THESIS FOR THE DEGREE OF DOCTOR OF PHILOSOPHY

Computational Modelling for Cavitation and Tip Vortex Flows

ABOLFAZL ASNAGHI

Department of Mechanics and Maritime Sciences
CHALMERS UNIVERSITY OF TECHNOLOGY
Göteborg, Sweden 2018

Computational Modelling for Cavitation and Tip Vortex Flows

ABOLFAZL ASNAGHI
ISBN: 978-91-7597-744-7

Series number: 4425
ISSN 0346-718X

Department of Mechanics and Maritime Sciences
Chalmers University of Technology
SE-412 96 Göteborg
Sweden
Telephone + 46 (0)31-772 1000

Printed by Chalmers Reproservice
Göteborg, Sweden 2018

Computational Modelling for Cavitation and Tip Vortex Flows

ABOLFAZL ASNAGHI, 2018
Department of Mechanics and Maritime Sciences, Chalmers University of Technology

Abstract

Cavitation often brings negative effects, such as performance degradation, noise, vibration, and material damage, to marine propulsion systems, but for optimum performance, cavitation is almost inevitable. Therefore, it is necessary to better understand cavitation in order to maximize the performance without encountering severe problems. Experimental tests can only provide limited information about this complex phenomenon. This thesis deals with improving computational methodologies that can offer a more complete picture of the cavitation process, making it possible to investigate the flow in more details with a higher level of confidence, which eventually enables an improved design.

The study describes cavitation behaviour in the early stage of the formation, i.e. cavitation inception and its interaction with tip vortex structures, as well as in the developed form, i.e. sheet and cloud cavitation. The analysis of the tip vortex flows is associated with the spatial mesh resolution, the sub-grid scale and the turbulence modelling, as well as the cavitation-vortex interaction.

For inception prediction, different inception methods are investigated to characterize tip vortex flows around an elliptical foil and high skewed low noise propellers. The adopted inception models cover different levels of complexity including wetted flow analysis, Eulerian cavitation simulations, and simplified Lagrangian Rayleigh-Plesset bubble dynamics models.

For simulations of developed sheet/cloud cavitating flows, a homogeneous two-phase mixture method is adopted along with the Schnerr-Sauer mass transfer model. A manual calibration of the mass transfer model coefficients may significantly affect both accuracy and stability of the numerical predictions. In order to avoid this issue, an approach is suggested and tested to compute the mass transfer rate based on the flow local time scale during the solution procedure.

Comparison between high speed videos and numerical results clearly shows the capability of the developed method in predicting the cavitating structures. It is shown that in addition to the well-captured difference in e.g. the amount of cavitation, the simulation is capable of correctly predicting the small though crucial differences in flow features and cavitation inception characteristics of different propellers designs. The strong dependency of the inception on the initial nuclei sizes are demonstrated, and it is shown that for weaker propeller tip vortices this dependency becomes even more significant.

Keywords: Cavitation, Inception, Numerical simulation, LES, SST $k-\omega$, Curvature correction, OpenFOAM, Elliptical foil, Twisted Delft foil, Propeller.

To my family

ACKNOWLEDGEMENT

This work would have not been possible without the help, support and encouragement of many people along the last few years. First and foremost, I would like to express my sincere gratitude to my supervisor Prof. Rickard E. Bensow for the continuous support of my PhD study, for his patience, motivation, and immense knowledge. I am truly grateful for all the freedom to try new things. I could not have imagined having a better supervisor and mentor for my PhD study.
I would like to thank my co-supervisors Dr. Urban Svennberg, and Dr. Andreas Feymark for all the valuable discussions, enthusiasm and support. I enjoyed every minute of discussions I had with you.
Thanks towards all of my colleagues in the Department of Mechanics and Maritime Sciences for providing a wonderful atmosphere.
Financial support for this work has been provided by Rolls-Royce Marine through the University Technology Centre in Computational Hydrodynamics hosted at the Department of Mechanics and Maritime Sciences at Chalmers. My sincere thanks goes to Johan Lundberg and Göran Grunditz, who provided me an opportunity to join the Rolls-Royce Technology Centre at Chalmers, and who gave access to the laboratory and research facilities at Kristinehamn. Without their support, it would not be possible to conduct this research.
Chalmers Centre for Computational Science and Engineering (C3SE) is also acknowledged for providing computational resources through the project.
Last but not the least, I would like to thank my family: my parents, my wonderful sisters and Sara for supporting me spiritually throughout my PhD life in Sweden. Words cannot express how grateful I am.

LIST OF PAPERS

The thesis consists of the following publications:

Paper A A. Asnaghi, A. Feymark, and R.E. Bensow. Improvement of Cavitation Mass Transfer Modeling Based on Local Flow Properties. International Journal of Multiphase Flow, 93:142 157, 2017.

Paper B A. Asnaghi, A. Feymark, and R.E. Bensow. Numerical Investigation of the Impact of Computational Resolution on Shedding Cavity Structures (Revision submitted to the International Journal of Multiphase Flow).

Paper C A. Asnaghi, R.E. Bensow, and U. Svennberg. Large Eddy Simulations of Cavitating Tip Vortex Flows (Under Review, Ocean Engineering).

Paper D A. Asnaghi, U. Svennberg, and R.E. Bensow. Analysis of Tip Vortex Inception Prediction Methods (Under Review, Ocean Engineering).

Paper E A. Asnaghi, U. Svennberg, and R.E. Bensow. Evaluation of Curvature Correction Methods for Tip Vortex Prediction in The SST $k-\omega$ Turbulence Model Framework (Under Review, International Journal of Heat and Fluid Flow).

Paper F A. Asnaghi, U. Svennberg, and R.E. Bensow. Numerical and Experimental Analysis of Cavitation Inception Behaviours for High-Skewed Low-Noise Propellers (Under Review, Applied Ocean Research).

OTHER RELEVANT PUBLICATIONS

In addition to the appended papers, I have authored or co-authored the following publications during my PhD:

Paper I A. Asnaghi, , R.E. Bensow, and U. Svennberg. Implicit large eddy simulation of tip vortex on an elliptical foil. In Proceedings of Fifth International Symposium on Marine Propulsion, Espoo, Finland, 2017.

Paper II A. Asnaghi, , R.E. Bensow, and U. Svennberg. Comparative analysis of tip vortex flow using RANS and LES. In Proceedings of VII International Conference on Computational Methods in Marine Engineering, Nantes, French, 2017.

Paper III A. Asnaghi, A. Feymark, and R.E. Bensow. Computational analysis of cavitating marine propeller performance using OpenFOAM. In Fourth International Symposium on Marine Propulsors, At Austin, Texas, USA, 2015.

Paper IV A. Asnaghi, A. Feymark, and R.E. Bensow. Numerical analysis of tip vortex flow. In Proceedings of the 16th Numerical Towing Tank Symposium, Olron, French, 2016.

Paper V A. Asnaghi. Developing Computational Methods for Detailed Assessment of Cavitation on Marine Propellers. Technical report, Department of Shipping and Marine Technology, Chalmers University of Technology, 2015. Lic.Eng. Thesis, Report No. 15:156.

Paper VI A. Asnaghi, A. Feymark, and R.E. Bensow. Workshop on cavitation and propeller performance. In 18th Numerical Towing Tank Symposium, 2015.

Paper VII A. Asnaghi, A. Feymark, and R.E. Bensow. Shear stress effects in cavitating flows. In 17th Numerical Towing Tank Symposium, Marstrand, Sweden, 2014.

CONTENTS

1

Introduction

Cavitation is the formation of vapour in a liquid when the local static pressure of the liquid falls below a critical pressure threshold. As the pressure of a larger region gets below the threshold pressure, more liquid will change phase into vapour. Without considering the effects of shear forces in flowing fluids, the pressure threshold is equal to the saturation pressure.

The region or pocket of the generated vapour in the cavitating flow is called cavity. The cavity can be either steady and attached to the surface or it can be separated from the surface and transported downstream. The size of the cavity might vary from an aggregation of a few bubbles to a size that covers the whole object [1].

There are five main cavitation patterns observable in cavitating flows depending on the operating conditions and fluid properties. *Bubble cavitation* consists of the formation of separated bubbles, their transportation to the downstream, and their collapse in the higher pressure region of the flow downstream. In *sheet cavitation*, the cavity stays attached to the surface. The interface between liquid and vapour at this condition is sharp and easily distinguishable. *Cloud cavitation* consists of a large collection of small bubbles separated from the initial sheet cavity. If there is a re-entrant flow at the end of the cavity that is strong enough to separate the cavity from the surface, two-phase vortex shedding occurs. This phenomenon is characterized by strong vibration, and noise. In the case that the transported cavity collapses near the surface, the risk of erosion is also considerable. In *supercavitation*, the cavity is large enough to cover either the whole object or most of it. The main application of supercavitation is to decrease the drag force. In propeller, unfavourable supercavitation can lead to thrust break-down. However, it should be noted that some propellers are designed to operate in the supercavitating regime. The last form of cavitation is *vortex cavitation*. This type of cavitation can be defined as the formation of cavitation in the core of vortices. Due to the high velocity gradients and the flow feature of vortices, the pressure at a vortice

core is lower than the surroundings. If the pressure of the core falls below the saturation pressure, cavitation will start at the core, and can travel to the downstream of the flow with the vortices. This type of cavitation mainly occurs on the tips of rotating blades and in the separation zone of bluff bodies.

On a ship propeller, which is of main concern in the framework of this thesis, formation of cavitation can cause performance degradation, and can produce vibration and noise. In the old days, the general philosophy for propeller design was to avoid cavitation for the widest possible range of operating conditions. One obvious way is to use propellers with larger blade area able to provide adequate propulsion while operating at low revolutions, but in many cases it is practically impossible, and the propulsive efficiency is relatively low due to great frictional losses associated with large blade surface. In order to reduce the cost of fuel as well as lowering the pollution, efforts have been devoted into enhancing the efficiency of ship propulsion. It is therefore necessary to decrease the margin of cavitation-free operation or to allow for some controlled amounts of cavitation on the propeller blades. Of course, this can be done only if the negative impacts such as noise, vibration and erosion are controlled [2].

Correctly predicting the cavitation behaviour of the propeller, as a function of loading conditions, is crucial in balancing difficult constraints in demanding design tasks. A propeller should preferably be ensured to meet the requirements relating to comfort (noise and vibration), and economic operation (efficiency) prior to construction, otherwise the cost of manufacture and repair can easily increase drastically. Propeller design then becomes a game of balancing different pros and cons in which it is crucial to be able to determine the characteristics of cavitation and not only its existence or extent. However, the co-existence of phase change and vortical structures creates a complex flow structure on propellers which involves very small scale dynamics both in time and spatial coordinates. Understanding the physics of these flows is important in order to prevent or control the occurrence of cavitation on propellers. The motivation of this PhD study is to provide a numerical tool to simulate different propeller cavitation patterns, e.g. leading edge sheet cavity and cavitating tip vortex, in order to provide an advanced CFD tool for propeller design comparison.

1.1 Erosion, noise and vibration

Cavitation can occur in a machine for several reasons [1, 3, 4]:

1. Change of streamline curvature (e.g. blades tip, and restricted section passage like nozzles) leads to local increase of flow velocity and reduction of pressure which in some circumstances can cause cavitation;
2. Flow instabilities can cause pressure fluctuations (e.g. in diesel injectors);
3. Solid surface imperfections (e.g. in hydraulic constructions);

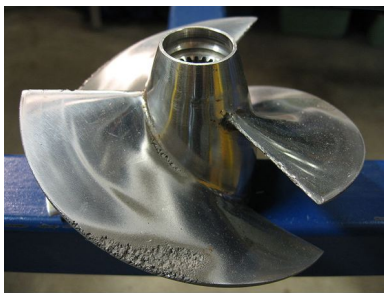

Figure 1.1: Erosion caused by cavitation on an arbitrary propeller [5]

4. High shear and high vortex flows (e.g. in cavitating jet, and turbine vortex rope).

For a system or machine designed to operate in liquid (or with very limited amount of cavitation), presence of cavitation is unfavourable and may cause several negative consequences, mainly on the performance and life time of the machine. For propellers, cavitation can increase the losses, and therefore decrease the efficiency or limit the thrust. Another negative aspect of cavitation is related to the collapse of the cavity.

The collapse can cause severe pressure pulses. In the case that these collapses occur near a surface, they can cause damage by removing material from the surface, which is called erosion, Figure 1.1. This process is noisy, and also due to posing high pressure pulses at different time occasions to the solid surface, can lead to significant vibration on the body. This phenomenon is complex since it involves both the flow characteristics and surface material properties. Therefore, in order to control it one has to investigate hydrodynamics behaviours of the flow and also the structural responses of the solid body to these hydrodynamics behaviour at the same time.

1.2 Effective parameters

Along with the pressure threshold, there are other parameters that contribute to the cavitation formation including water nuclei content, surface roughness, viscous effects, and turbulence properties.

Experimental tests have revealed that when the amount of dissolved gas bubbles inside the liquid is very low, the cohesion force between liquid molecules becomes very strong. At this condition, the liquid can withstand tension (i.e. negative pressure) without undergoing any phase change. The dissolved or non-condensable gas bubbles act as weak points inside the liquid where the cohesion force is weaker than other parts of the liquid and therefore the liquid breaking down, i.e. cavitation inception, starts from these points. These dissolved gas bubbles are known as nuclei [1, 3].

A laminar boundary layer can suppress cavitation inception, and affects its pattern due to the change in the location of cavitation inception. While the bound-

ary layer of full scale propellers are considered to be fully turbulent, except for a small region close to the propeller leading edge, the boundary layer on a model scale propeller can be laminar on a considerable part of the blade area. Therefore, it is possible that due to differences in the boundary layer between model and full scale, different cavitation patterns are observed. One solution to this discrepancy is to deliberately trip the boundary layer of model scale into turbulence at the leading edge by applying roughness. In this condition, the model scale boundary layer transition will occur close to the leading edge representing the full scale flow pattern much better [6, 7].

1.3 EULERIAN CAVITATION SIMULATION

In the Eulerian description of a field, the field (e.g. velocity, pressure, density, etc.) is represented as a function of position x and time t while a Lagrangian specification of the field is a way of looking at fluid motion where the observer follows an individual fluid particle as it moves through space and time. Considering two-phase flow, different approaches can be used which are briefly described below [8, 9, 10].

1. Single fluid mixture approach: In this methodology, the multiphase flow is treated as a single mixture fluid. The mass and momentum conservation equations are solved only for the mixture fluid. An extra equation, a transport equation of void fraction or a barotropic model, is needed to calculate the distribution of phases, and recompute the mixture fluid properties.

2. Euler-Euler approach: In this approach, the liquid and vapour phases are both described as interpenetrating fluids. For each phase, a set of mass and momentum equations is solved and coupled with other phases properties to close the governing equations.

3. Euler-Lagrange approach: If there is a continuous phase and a dilute/disperse phase where the dispersed phase occupies a low volume fraction, then the fluid phase is treated as a continuum while the dispersed phase is considered as particles modelled individually. In that case, the mass and momentum equations are solved for the continuous phase while the dispersed phase is solved by Lagrangian Particle Tracking method. It tracks the particles or bubbles through the calculated flow field. The dispersed phase exchanges momentum, mass and energy with the fluid phase. The trajectory of the particles are calculated individually by either one way or two way coupling with the main flow [8].

In the transport equation model (TEM) of the single fluid mixture modelling, the mass transfer between liquid and vapour is modelled using source terms. In most of the applications of this model, the transport of volume or mass of either

liquid or vapour is modelled. Then the transport equation is considered with mass, and momentum equations of the mixture fluid to close the governing equations. Different models have been proposed to model the mass transfer rate in TEM. Derived from the Rayleigh-Plesset equation, Sauer and Schnerr proposed a model based on the dynamics of a single bubble [11, 12]. In order to improve the phase change modelling, some author have proposed models derived from the Rayleigh-Plesset equation which includes empirical coefficients [13, 14]. Some of the proposed models are based on the practical methodology of using effective parameters and then using empirical factors in order to adjust the mass transfer between liquid and vapour phases [15, 16]. In order to get rid of the empirical constants, a model was proposed by Senocak and Shyy to explicitly calculate the coefficients of the mass transfer model from the interfacial velocity terms [17, 18, 19].

The main advantages of TEM are the convective characteristics of the model which allows appropriate modelling of the cavity detachment and also cavity closure. In contrast to the barotropic models, in TEM approach, the density is a function of the transport process. Consequently, gradients of density and pressure are not necessarily parallel, suggesting that the model can accommodate the vorticity production term as highlighted by recent experimental studies [20].

The main drawback of TEM comes from the source terms and phase change rate modelling. If the source term parameters (e.g. empirical coefficients, bubble density, bubble size, etc.) are not properly set, the accuracy of the numerical predictions can be significantly affected. In this thesis, these conditions are investigated and the effects of the phase change rate on the final results are highlighted.

1.4 Cavitating tip vortex

As the flow passes over a lifting wing with finite span, a pressure differential exists between the upper and lower surfaces of the wing. Close to the wing tip, this pressure differential drives the fluid from the high pressure side on the lower surface to the low pressure side on the upper surface. This makes the flow highly three dimensional at the tip region and creates a vortex pattern. As this vortex is transported downstream, it rolls up more and more of the wing wake until its circulation becomes nominally equal to that of the wing. This typically extends to a few chord lengths downstream of the trailing edge, called the near field region. After this region and when the roll-up is finished, the vortex will start to decay due to the flow viscosity, instability and also bursting [21, 22, 23].

Tip vortex flows are known to be challenging flows to study because of the presence of anisotropic turbulence and large gradients of pressure and velocity in all three directions, especially across the vortex core. The evolution of the strength and size of a tip vortex along its path is a complex phenomenon, governed by both viscous diffusion and the capture of vortex lines. Modelling and prediction of the minimum pressure coefficient is difficult, especially in the vicinity of the wing where the tip vortex is far from being axisymmetric [24, 25].

Due to the swirling nature of the vortex, the pressure in the vortex core is lower than in the surrounding. Therefore, in the cavitating case, cavitation inception would occur in the vortex core. The tip vortex cavitation inception complicates the flow physics even further as it depends on additional flow parameters, such as nuclei distribution, residence time, and turbulence fluctuation, which are very difficult to control during experimental tests, as well as in numerical simulations [26, 27, 28, 29].

Experimental tests on propellers can provide very useful information about the vortex properties and the tip vortex cavitation inception. However, despite the huge cost which has to be spent for each test, as the tip vortex involves small scales of flow dynamics, it is very difficult to measure all relevant flow features, e.g. velocity distribution. Another drawback is the disability of the current tools to measure the pressure at the vortex core where cavitation inception occurs. Numerical simulations can be used to give further insights on the tip vortex properties that experimental tests may not be able to provide [30, 31, 32].

The experimental assessment of cavitation is not straightforward and suffers from large uncertainties. This comes from the complex dependency of the tip vortex inception on the Reynolds number through the boundary layer development on the blades, shear layer vorticity interaction in the blade wake, and primarily nuclei distribution and its interactions with the low pressure region of the vortex. Further, there are technical difficulties in distinguishing the actual inception point. As a result, this makes numerical validation of inception points almost out of reach even though wetted tip vortex flows can be predicted reasonably well.

By consideration of some simplifications, however, some methods are proposed to numerically predict inception points including minimum pressure criterion, semi-empirical relation, energy of low pressure region, Eulerian cavitation simulation, and bubble dynamics method.

The simplest numerical approach to determine the cavitation inception number, σ_i, is the minimum pressure criteria. In this method, the operating condition when the lowest pressure value of a wetted flow falls below the saturation pressure is called the inception point. Considering the fact that cavitation inception is essentially a wetted flow problem, the advantage of the method is its simplicity, as it only requires the pressure field of the wetted flow simulation to determine the inception point. As the method does not include the nuclei contribution on the inception prediction, the method usually leads to over prediction of σ_i.

The methods that include the nuclei effects, and model bubble dynamics behaviours in order to determine the inception point, can be classified into three different groups including the two-way coupling, one-way coupling, and simplified one-way coupling [33]. The most advanced approach considers the two-way coupling between bubbles and the flow field. The bubbles are injected upstream and tracked downstream. As two-way coupling is considered, the bubbles size and distribution affect the velocity and pressure field. The second category, so called uncoupled approach, only includes the effects of the fluid on the bubbles, and it is assumed that the effects of the bubbles on the flow field is negligible.

The uncoupled assumption reduces the computational requirements. In the third model, a single spherical particle is assumed to travel through a specific path, e.g. tip vortex trajectory.

1.5 OBJECTIVES

Previous studies on the numerical simulation of cavitating flows using LES performed by Huuva [34] and Lu [2] were encouraging and promising. In these results the global mechanisms of cavitation were well captured in the simulation. The first part of the current work, therefore, is focused on using and also developing the previous computational methodology for cavitating flows simulation. The main original contribution presented here is the modification of the Schnerr-Sauer mass transfer model. The investigated cavitation mechanisms are related to cavitation formation and development which have direct effects on the flow structure and characteristics such as force distributions, pressure pulse, noise, vibration and erosion risk.

The second part of the work focuses on the formation and development of cavitating tip vortex flows. Tip vortex characteristics of a propeller has a direct impact on the propeller tip vortex cavitation inception which is important in defining the boundaries of the cavitation bucket chart of a propeller [35]. Correctly predicting the cavitation behaviour of the propeller, as a function of loading conditions, is crucial in balancing difficult constraints in demanding design tasks. The co-existence of phase change and tip vortex creates a complex flow structure in the tip region of propellers which involves very small scale dynamics both in time and spatial coordinates. Understanding the physics of these flows is important in finding the tip vortex inception speed in order to prevent or control the occurrence of cavitation on propellers [36, 37, 38]. Therefore, the impact of grid resolutions, turbulence modelling, and cavitation inception models are evaluated in predicting the cavitation inception point.

The main objectives of the current work can be listed as follows:

1. To investigate the capability of the methodology in predicting the cavitation pattern and the large scale two-phase mechanisms that interact with collapse, erosion risk, noise, and performance degradation of propulsor systems;

2. Investigation of mesh resolution effects on cavitation prediction (formation, development, transfer and collapse);

3. Providing a guideline for tip vortex simulations in the OpenFOAM numerics by describing the spatial grid resolution requirements, and turbulence modelling impacts;

4. Evaluating performance of different cavitation inception models in a benchmark case, e.g. the elliptical foil, and also in engineering applications, e.g.

high skewed propeller;

5. Apply the numerical methodology in engineering configurations in order to provide further knowledge for guiding the development of design principles.

1.6 THESIS OUTLINE

Following the present chapter, the thesis is structured as follows:

In Chapter 2, the governing equations employed in the current study for numerical simulations in OpenFOAM are presented. Conservation equations of mass and momentum, turbulence closure approaches, and cavitation modelling are described. To compute the LES sub-grid scale tensor, Implicit LES and Localized Dynamic Kinematic model (LDKM) are adopted. As a two-equation RANS model, the transport equations of the SST $k-\omega$ model along with different curvature corrections models are explained. By taking advantage of the homogeneous assumption, the two-phase mixture is modelled via the effective fluid for cavitation simulations. The phases are considered incompressible, isothermal and immiscible. The transport equation is used to calculate the distribution of each phase.

In Chapter 3, the studied cases, which include the Delft Twisted hydrofoil, Elliptical foil, E779A propeller, PPTC propeller, and four different designs of the Rolls-Royce high skewed propellers, are presented. For each case, descriptions of the geometry, experimental measurements, operating flow conditions, computational domain, and spatial mesh specifications are described.

In Chapter 4, the results of the tip vortex simulations are presented. The first part of the chapter contains the analysis of the spatial mesh resolution requirements for tip vortex simulations. The tip vortex flow around the elliptical foil is selected as the benchmark, and the grid resolution and turbulence modelling impacts on the numerical prediction of the tip vortex are evaluated.

Chapter 5 contains the sheet/cloud cavitation simulations around the Delft Twisted foil, Elliptical foil, E779A propeller, PPTC propeller, and Rolls-Royce high skewed propellers A and B. Effects of mesh resolution, computational setup and design changes on the flow structure and cavitation pattern are analyzed in this chapter.

In chapter 6, cavitation inception methods are evaluated and validated on the elliptical foil. Different inception models including the minimum pressure criterion, semi-empirical relation, energy balance, Eulerian cavitation simulation, and a simplified uncoupled bubble dynamics model are adopted, and the results are compared with the experimental data. In the second part, the analysis is extended to the Rolls-Royce high skewed propellers simulations, and for each propeller the cavitation inception chart is derived. For propeller D, the effects of the spatial resolution on the cavitation inception prediction is included.

In Chapter 7, the numerical simulations of tip vortex flows around the Rolls-Royce high skewed propellers C and D are presented and compared with high speed videos. The analysis contains the wetted flow, and cavitating conditions a three different operating conditions including J=0.82, 0.933, and 1.26. Vortical structures around the propellers are addressed by employing very fine spatial resolutions at the tip region of the blades to highlight the propeller design impacts on the tip vortex structure, and cavitation formation.

In Chapter 8, a summary and suggestions for future work are presented.

The appendix includes the prepared/published journal papers, where further details about the literature review, methodologies, and cases tested are presented.

2

Governing Equations

This chapter elaborates the methods and equations used to simulate wetted and cavitating flows. The models include conservation equations of mass and momentum, turbulent closure models for LES and RANS, cavitation inception models, Eulerian cavitation simulation models, and uncoupled single bubble dynamics modelling by the Rayleigh-Plesset equation.

2.1 Conservation equations

The conservation equations of mass and momentum (in Cauchy description) for the mean fluid can be written as follow,

$$\frac{\partial \rho_{\mathrm{m}}}{\partial t} + \frac{\partial (\rho_{\mathrm{m}} u_i)}{\partial x_i} = 0, \tag{2.1}$$

$$\frac{\partial (\rho_{\mathrm{m}} u_i)}{\partial t} + \frac{\partial (\rho_{\mathrm{m}} u_i u_j)}{\partial x_j} = \frac{\partial \tau_{ij}}{\partial x_j} + \rho_{\mathrm{m}} g_i. \tag{2.2}$$

The stress tensor of Newtonian fluids is conventionally written in the form of summation of the pressure stress and shear stresses,

$$\tau_{ij} = -p\delta_{ij} + S_{ij} - \frac{2}{3}\mu_m \frac{\partial u_{\mathrm{k}}}{\partial x_{\mathrm{k}}}\delta_{ij}, \tag{2.3}$$

$$S_{ij} = 2\mu D_{ij}. \tag{2.4}$$

Here, p is the static pressure, ρ_m and μ_m are the effective (mixture) density and viscosity, S is the viscous stress tensor and $D_{ij} = \frac{1}{2}(\frac{\partial u_i}{\partial x_j} + \frac{\partial u_j}{\partial x_i})$ is the deformation rate tensor (symmetric part of the velocity gradient), respectively.

2.2 TURBULENCE MODELLING

Most turbulent flows consist of vortex filaments and sheets with characteristic scales on the order of the Taylor and Kolmogorov scales, l_T and l_K , typically being orders of magnitude smaller than the integral scale which is the reference length of the flow, l_{ref}. The Taylor micro scale is an intermediate length scale at which fluid viscosity significantly affects the dynamics of turbulent eddies in the flow.

In DNS, all flow scales (down to l_K) are resolved, making such simulations too expensive for engineering applications. Instead LES, in which all the flow scales smaller than l_T are modelled, thus having weaker resolution requirements, have emerged as a viable alternative for engineering predictions. In RANS, on the other hand, all flow scales are modelled, which in general implies lower resolution requirements compared with LES.

Most of the simulations presented in this thesis are conducted by employing Implicit LES. This model has been used for cavitation simulations, and has been validate in different applications. For tip vortex simulations, two more turbulence models are investigated, the Localized Dynamic Kinematic sub-grid stress Model (LDKM) as an explicit LES, and the RANS SST $k-\omega$ model. LDKM is chosen to provide further insights on the effects of LES sub-grid scale modelling in predictions of tip vortex flows. As in some engineering applications, limitation of computational resources forces the adoption of RANS turbulence modelling, the SST $k-\omega$ model is evaluated, and its applications with and without curvature corrections are addressed.

2.2.1 LES turbulence modelling

Using the low pass filtering approach, the conservation equations of mass and momentum in LES models can be written as,

$$\frac{\partial \rho_{\mathrm{m}}}{\partial t}+\frac{\partial(\rho_{\mathrm{m}}\bar{u}_i)}{\partial x_i}=0, \tag{2.5}$$

$$\frac{\partial(\rho_{\mathrm{m}}\bar{u}_i)}{\partial t}+\frac{\partial(\rho_{\mathrm{m}}\bar{u}_i\bar{u}_j)}{\partial x_j}=-\frac{\partial \bar{p}}{\partial x_i}+\frac{\partial}{\partial x_j}(\bar{S}_{ij}-B_{ij})+\rho_{\mathrm{m}}g_i, \tag{2.6}$$

where the over bar denotes low pass filtered quantities, and $B_{ij}=\rho(\overline{u_iu_j}-\bar{u}_i\bar{u}_j)$ is the subgrid stress tensor. In the current research, two different strategies are considered to model the LES subgrid stress tensor, Implicit LES (ILES) and Localized Dynamic Kinematic subgrid stress Model (LDKM) as an explicit model.

In ILES, no explicit model is applied for B_{ij}, instead the numerical dissipation is considered enough to mimic the action of B_{ij} [39, 40, 36, 41]. Therefore, for the momentum convection term, a relatively dissipative scheme should be used to provide appropriate numerical diffusion in the solution procedure [42]. Here, a fixed blending of the first order upwind scheme, 20%, and the second order

central difference scheme, 80%, is used for ILES [43]. For LDKM, the second order limitedLinear scheme is employed.

In LDKM, a transport equation is solved to calculate the subgrid-scale kinetic energy,

$$\frac{\partial(\rho k_{sgs})}{\partial t}+\frac{\partial(\rho k_{sgs}\bar{u}_j)}{\partial x_j}=-B_{ij}\frac{\partial \bar{u}_i}{\partial x_j}-C_\varepsilon\rho\frac{k_{sgs}^{\frac{3}{2}}}{\Delta}+\frac{\partial}{\partial x_j}(\frac{\mu_t}{\sigma_k}\frac{\partial k_{sgs}}{\partial x_j}), \tag{2.7}$$

where the subgrid-scale kinetic energy is,

$$k_{sgs}=\frac{1}{2}(\overline{u_i u_i}-\bar{u}_i\bar{u}_i). \tag{2.8}$$

The subgrid-scale stress is then computed as,

$$B_{ij}-\frac{2}{3}\rho k_{sgs}\delta_{ij}=-2C_k\rho {k_{sgs}}^{\frac{1}{2}}\Delta\bar{S}_{ij}. \tag{2.9}$$

In Eq. 2.9 and 2.7, C_k and C_ε are model constants which are determined dynamically; see [44] for further details.

2.2.2 *SST $k-\omega$ model*

The SST $k-\omega$ model proposed by Menter [45, 46] adopts a blending function that switches from the $k-\omega$ model close to the wall to the $k-\varepsilon$ model outside the boundary layer. To provide further simplicity, the ε transport equation is transformed into an ω transport equation by variable substitution. The transformed equation is similar to the one in the standard $k-\omega$ model, but adds an additional non-conservative cross-diffusion term, $\frac{1}{\omega}\frac{\partial k}{\partial x_i}\frac{\partial \omega}{\partial x_i}$. Over the last two decades, the model has been used widely in different flow applications, e.g. marine and aerodynamics, and is proved to provide reasonably accurate results.

The transport equations for the turbulent kinetic energy and the specific dissipation rate of the SST $k-\omega$ model are,

$$\frac{\partial(\rho k)}{\partial t}+\frac{\partial(\rho\bar{u}_i k)}{\partial x_i}=P_k+D_k+\frac{\partial}{\partial x_i}[(\mu+\sigma_k\mu_t)\frac{\partial k}{\partial x_i}], \tag{2.10}$$

$$\frac{\partial(\rho\omega)}{\partial t}+\frac{\partial(\rho\bar{u}_i\omega)}{\partial x_i}=P_\omega+D_\omega+\frac{\partial}{\partial x_i}[(\mu+\sigma_\omega\mu_t)\frac{\partial \omega}{\partial x_i}], \tag{2.11}$$

where P_k and P_ω are the production terms, and D_k and D_ω are the destruction terms, σ_k and σ_ω are the model coefficients, and μ is the dynamic viscosity of the fluid. The production terms of the model without considering buoyancy effects are,

$$P_k=\mu_t\bar{S}^2-\frac{2}{3}\rho k\frac{\partial(\bar{u}_i)}{\partial x_i}-\frac{2}{3}\mu_t(\frac{\partial(\bar{u}_i)}{\partial x_i})^2, \tag{2.12}$$

$$P_\omega=G_\omega+G_{CD}, \tag{2.13}$$

$$G_\omega = \rho\gamma\bar{S}^2 - \frac{2}{3}\rho\gamma\omega\frac{\partial(\bar{u}_i)}{\partial x_i} - \frac{2}{3}\rho\gamma(\frac{\partial(\bar{u}_i)}{\partial x_i})^2, \tag{2.14}$$

$$G_{CD} = 2\rho(1-F_1)\sigma_{w2}\frac{1}{\omega}\frac{\partial k}{\partial x_i}\frac{\partial \omega}{\partial x_i}, \tag{2.15}$$

where γ and σ_{w2} are the model coefficients.

The production term of the ω transport equation is decomposed into two terms, G_ω and G_{CD}. The second term is the cross-diffusion term which is the consequence of the transformation of the ε transport equation into ω transport equation. Therefore, close to the wall, where the F_1 function tends to one, it will be negligible and the model will then switch to the $k-\omega$ model, and far from the boundary layer, where the F_1 function tends to zero, it will be non-zero and consequently the model will switch to the $k-\varepsilon$ model.
The destruction terms are,

$$D_k = -\rho\beta^* k\omega, \tag{2.16}$$

$$D_\omega = -\rho\beta\omega^2, \tag{2.17}$$

where β^* and β are the model coefficients. The turbulent viscosity is calculated as [46],

$$\mu_t = \frac{a_1\rho k}{\max(a_1\omega, \bar{S}F_2)}. \tag{2.18}$$

The two-equation models predict an unexpectedly large growth of turbulent kinetic energy in the stagnation point regions leading to over prediction of turbulent viscosity. Therefore, it is proposed to include a lower limit on the turbulence viscosity to impose the realizability constraint on the turbulent viscosity formula,

$$\mu_t = \min(\frac{a_1\rho k}{\max(a_1\omega, \bar{S}F_2)}, \frac{\rho k C_T}{\sqrt{3}\bar{S}}), \tag{2.19}$$

where C_T is the model coefficient. More details about the model can be found in [46, 47].

2.2.3 Curvature correction models

The assumption that the Reynolds stress tensor is linearly proportional to the mean strain rate does not consider anisotropy of turbulence. This drawback, especially in fully three dimensional turbulent structures where the anisotropy turbulent quantities are of importance, limits the accuracy of the modelling. Reynolds Stress Models, RSMs, however, can account for streamline curvature effects in a systematic manner because of the presence of exact production terms containing mean flow gradients and system rotation. They also contain the convective transport of the second moments and hence provide an accurate means for predicting the curved flows. RSMs are still not tractable in complex industrial applications

due to excessive computational cost and numerical stiffness. This is the motivation to incorporate rotation and curvature effects into the scalar eddy viscosity framework of RANS approaches, such as the SST $k-\omega$ model [48, 49, 50, 51]. More details about the curvature correction, CC, concept and history of the development are presented in Paper E.

In CC models that employ the vorticity rate tensor and without considering the frame rotation, the streamline curvature is incorporated as,

$$\Omega_{ij}^{mod} = \Omega_{ij} + (C_r - 1)W_{ij}^{A}, \tag{2.20}$$

where C_r is the constant of the equation and depends on the curvature correction model. This coefficient takes a value of 2 for bifurcation approaches. The W_{ij}^{A} tensor which contains the effects of curvature corrections in the vorticity tensor is defined by [52, 47, 53],

$$W_{ij}^{A} = -\varepsilon_{ijk}B_{km}S_{pr}\frac{DS_{rq}}{Dt}\varepsilon_{pqm}, \tag{2.21}$$

$$B_{km} = \frac{II_S^2\delta_{km} + 12III_S S_{km} + 6II_S S_{kl}S_{lm}}{2II_S^3 - 12III_S^2}, \tag{2.22}$$

$$II_S^2 = S_{kl}S_{lk}, \quad III_S^2 = S_{kl}S_{lm}S_{mk}, \tag{2.23}$$

where $\frac{DS_{rq}}{Dt}$ is the material derivative of the strain rate tensor. The non-dimensional strain rate and vorticity tensors then are defined by,

$$S_{ij}^{*} = \tau S_{ij}, \quad \Omega_{ij}^{*} = \tau\Omega_{ij}^{mod}. \tag{2.24}$$

Three other parameters used in curvature correction models are defined as,

$$\eta_1 = S_{ij}^{*}S_{ij}^{*}, \quad \eta_2 = \Omega_{ij}^{*}\Omega_{ij}^{*}, \quad \eta_3 = \eta_1 - \eta_2. \tag{2.25}$$

As it can be seen, η_1 represents the non-dimensional strain rate magnitude, η_2 represents the non-dimensional vorticity magnitude. It can be also noted that η_3 represents the minus of the non-dimensional Q criterion.

Pettersson (CC1) [53]
The model was originally introduced for the v^2-f turbulence model, and later extended to the SST $k-\omega$ model as $\nu_t = C_\mu^{*}k/\omega$,

$$C_\mu^{*} = C_\mu\frac{1+\alpha_2 \mid \eta_3 \mid +\alpha_3\eta_3}{1+\alpha_4 \mid \eta_3 \mid}\left(\sqrt{\frac{1+\alpha_5\eta_1}{1+\alpha_5\eta_2}} + \alpha_1\sqrt{\eta}_2\sqrt{\mid \eta_3 \mid -\eta_3}\right)^{-1}, \tag{2.26}$$

where $(\alpha_1,\alpha_2,\alpha_3,\alpha_4,\alpha_5) = (0.055, 0.5, 0.25, 0.2, 0.025)$, and $C_r = 2.0$.

Arolla (CC2) [52]
The model uses the bifurcation diagram of the Second Moment Closure (SMC). The following function is proposed to enforce the model to follow the bifurcation and restabilization points to be closed to SMCs,

$$C_\mu^* = \min(C_\mu[\alpha_1(\mid \eta_3 \mid -\eta_3) + \sqrt{1-\min(\alpha_2\eta_3, 0.99)}]^{-1}, 2.5), \tag{2.27}$$

where $(\alpha_1, \alpha_2) = (0.04645, 0.25)$, and $C_r = 2.0$.

StarCCM+ (CC3) [54]
The curvature correction model used in StarCCM+ is the same as the Arolla curvature correction model, with the only difference that C_μ^* is limited to a maximum value of 1.25 rather than 2.5. It should be noted that in the StarCCM+ software, the curvature correction function is used as a multiplier of the k production term. In this study, we will consider both applications, as the C_μ sensitizer (CC3a) and as the k production term multiplier (CC3b).

η_3 **based (CC4)** [55]
In this model, the production term of the ω-equation is multiplied by F_{rc},

$$F_{rc} = 1 + \alpha_1 \mid \eta_3 \mid + 3\alpha_1\eta_3, \tag{2.28}$$

where $\alpha_1 = -0.2$, and $C_r = 2.0$. Since F_{rc} is not usually bounded, it is limited to a maximum value of 10 to enforce the stabilization of turbulence and minimum value of zero to avoid negative dissipation.

Br **based (CC5)** [47]
This model is motivated by the Bradshaw number,

$$Br = \sqrt{\frac{\eta_2}{\eta_1}}(\sqrt{\frac{\eta_2}{\eta_1}} - 1). \tag{2.29}$$

The destruction term of the ω-equation is multiplied by F_4,

$$F_4 = \frac{1}{1 + C_{RC}Br}. \tag{2.30}$$

The model constants are $C_{RC} = 3.6$ and $C_r = 1.0$.

Menter (CC6) [56]
In this curvature correction form, the production term in both k and ω-equations are multiplied by the f_{r1} function,

$$f_{r1} = \max(\min(f_{rotation}, 1.25), 0, 0), \tag{2.31}$$

where

$$f_{rotation} = (1 + C_{r1})\frac{2r^*}{1+r^*}[1 - C_{r3}\tan^{-1}(C_{r2}\hat{r})] - C_{r1}. \tag{2.32}$$

In this equation, the functions are defined as,

$$r^* = \frac{\mid S \mid}{\mid \Omega \mid}, \tag{2.33}$$

$$\hat{r} = \frac{2\Omega_{ih}S_{jh}}{\mid \Omega \mid D^3}\frac{DS_{ij}}{Dt}, \tag{2.34}$$

where

$$D^2 = \max(S^2, 0.09\Omega^2), \quad S^2 = 2S_{ij}S_{ij}, \quad \Omega^2 = 2\Omega_{ij}\Omega_{ij}. \tag{2.35}$$

The constants of this model are $(C_{r1}, C_{r2}, C_{r3}) = (1.0, 2.0, 1.0)$. The model is also called SST-CC in the literature.

Stabnikov (CC7) [57]
The modification is similar to Menter CC, and is derived based on the matching evolution of the turbulent kinetic energy in rotating homogenous shear flows, and is of the form,

$$f_{r1-mod} = \max(f_{rotation-mod}, 0), \tag{2.36}$$

where

$$f_{rotation-mod} = (1+C_{r1})\frac{1+C_{r4}}{1+C_{r4}\mid r^*-2\mid}[1-C_{r3}\tan^{-1}(C_{r2}\hat{r})] - C_{r1}, \tag{2.37}$$

and $(C_{r1}, C_{r2}, C_{r3}, C_{r4}) = (0.4, 1.0, 0.6, 0.1)$. In contrast to the Menter CC model, where the correcting function is used as a multiplier of the production term in both k and ω transport equations, the current modification multiplies only the production term of the k equation.

C_μ sensitization based on η parameters (CC8)
It is suggested and employed by Kato and Launder [58] to include the strain rate parameter into the calculation of C_μ,

$$C_{\mu-Mod-\eta_1} = C_\mu \max[\min(1, \frac{3.333}{1+0.35(\eta_1)^{1.5}}), 0.1], \tag{2.38}$$

where η_1 is the magnitude of the non-dimensional strain rate tensor. The modification was originally proposed for the $k-\varepsilon$ model. However, in the tip region, F_1 is very close to zero implying that the SST $k-\omega$ model is switched to the $k-\varepsilon$ model. Therefore, the application of the modification can be extended into SST $k-\omega$ model for tip vortex flow simulations as in the current study. As the vorticity is more significant in the tip vortex region, the application of η_2 instead of η_1 to compute C_μ is also investigated,

$$C_{\mu-Mod-\eta_2} = C_\mu \max[\min(1, \frac{3.333}{1+0.35(\eta_2)^{1.5}}), 0.1]. \tag{2.39}$$

In order to retain the original form in the absence of curvature or rotation, $C_\mu^* = C_\mu$, we also propose the application of η_3 in Eq. 2.38 and 2.39,

$$C_{\mu-Mod-\eta_3} = C_\mu \max[\min(1, \frac{3.333}{1+0.35(\eta_3)^{1.5}}), 0.1]. \tag{2.40}$$

We keep the clipping value, 0.1, equal to the previous equations.

The summary of the curvature correction models, and their contributions are presented in Table 2.1.

Table 2.1: Summary of curvature correction models

Name	Reference	Modification
CC1	Pettersson [53]	Modify the turbulent viscosity coefficient
CC2	Arolla [52]	
CC3a	StarCCM+ [54]	
CC3b	StarCCM+ [54]	Modify the production term in k equation
CC4	η_3 based [55]	Modify the production term of ω-equation
CC5	Br based [47]	Modify the destruction term of ω-equation
CC6	Menter [56]	Modify the production terms in k and ω-equations
CC7	Stabnikov [57]	Modify the production term in k equation
CC8	Kato and Launder [58]	Modify the turbulent viscosity coefficient

2.3 CAVITATION INCEPTION

Descriptions and details of cavitation inception models are included in Paper D, and Paper F. Here, the models are briefly summarized.

The simplest cavitation inception model is the minimum pressure criterion,

$$\sigma_i = -C_{p,min}. \tag{2.41}$$

This equation implies that cavitation occurs when the minimum pressure in the flow reaches the saturation pressure.

The second approach is from a curve fitting to cavitation inception data, so called semi-empirical relation. As an instance and for the elliptical foil in weak water, Arndt et al. [59] suggested the following formula,

$$\sigma_i = 0.068 C_l^2 Re^{0.4}. \tag{2.42}$$

The third approach employs energy balance between phases [60]. By considering a region with pressure lower than the saturation pressure, the volume of vapour generated by the energy stored in this region is,

$$\forall_v = \frac{(p_{sat} - p)\forall}{\rho_v L}, \tag{2.43}$$

where $\forall$ is the volume of the region with pressure lower than the saturation pressure, and L is the mass transfer latent heat.

The cavitation inception point can also be determined by the Eulerian cavitation simulations. This approach assumes that in the visual detection of tip vortex cavitation inception, a certain volume of vapour is required in order to be noticed by observers. Then, the cavitation inception point would be a condition which leads to this amount of vapour volume in the simulations. In this study, the vapour corresponding to a cylindrical shape with diameter of 1 mm, and length of 3 mm, is considered as the inception point. By assuming that the vapour volume fraction of this cylinder is 10%, the corresponding inception vapour volume would be 0.2365 mm^3.

Another approach in predicting the cavitation inception is to include the bubble dynamics into the flow simulations via either uncoupled approach or coupled approach. In the simplified uncoupled approach, the Lagrangian equations of motion are neglected, and it is assumed that bubbles are travelling through specific paths, e.g. streamlines of the wetted flow, or the core of the tip vortex. The Rayleigh-Plesset equation is then solved by considering the surroundings conditions of these paths. This simplified approach can be used for cases where the possible cavitation inception paths are known, such as the tip vortex trajectory where cavitation incepts primarily in the tip vortex core. In this case, the inception condition is when a bubble reaches to a certain radius.

2.4 EULERIAN MASS TRANSFER MODELLING

As described before, one approach to model the phase distribution is using a transport equation for volume or mass fractions, and then solving it along with the mass and momentum equations, Eq. 2.1 and Eq. 2.2, to calculate the velocity and pressure fields. In this work, the transport equation of liquid volume fraction is solved along with a source term to mimic the mass transfer between liquid and vapour. Using the volume fraction function, it is possible to calculate the mixture density and mixture viscosity based on the homogenous flow assumption,

$$\rho_{\mathrm{m}} = \alpha_{\mathrm{l}}\rho_{\mathrm{l}} + (1-\alpha_{\mathrm{l}})\rho_{\mathrm{v}},\ \mu_{\mathrm{m}} = \alpha_{\mathrm{l}}\mu_{\mathrm{l}} + (1-\alpha_{\mathrm{l}})\mu_{\mathrm{v}}, \tag{2.44}$$

$$\frac{\partial \alpha_{\mathrm{l}}}{\partial t} + \frac{\partial(\alpha_{\mathrm{l}} u_i)}{\partial x_i} = \frac{\dot{m}}{\rho}, \tag{2.45}$$

$$\frac{\partial u_i}{\partial x_i} = (\frac{1}{\rho_{\mathrm{l}}} - \frac{1}{\rho_{\mathrm{v}}})\dot{m}. \tag{2.46}$$

In Equation 2.45, which represents the transport equation of liquid volume fraction, the source term is the rate of mass transfer between vapour and liquid phases. Since the OpenFOAM package is utilized for solving the equations, similar notation is employed here for TEM. As it can be seen from Equation 2.46, in cavitating flows, due to the phase change, the flow is not divergence free, and therefore special considerations should be taken in solving the pressure correction equations.

2.4.1 Schnerr and Sauer cavitation model

The Schnerr-Sauer model assumes that there are several vapour bubbles, also called nuclei, inside the liquid which act as the initial sources of the phase change, and cavitation inception occurs due to their presence [11]. The number, size and distribution of these bubbles can be determined in water quality experiment tests. To simplify the numerical modelling, it is assumed that the initial nuclei have been distributed evenly throughout the liquid, and they have an equal size which is the smallest size that vapour bubbles can have.

The volume of nuclei, its volume fraction, and the radius of bubble can be described through Equations 2.47, 2.48 and 2.49. In these equations, n_0 is the number of nuclei in one cubic meter of liquid, and d_{Nuc} is the diameter of the nuclei. The radius of the bubble, R_B, is modified based on the notation used in OpenFOAM to consider the effects of initial nuclei volume fraction, α_Nuc,

$$\mathrm{Vol}_\mathrm{Nuc} = \frac{\pi n_0 d_\mathrm{Nuc}^3}{6}, \tag{2.47}$$

$$\alpha_\mathrm{Nuc} = \frac{\mathrm{Vol}_\mathrm{Nuc}}{1+\mathrm{Vol}_\mathrm{Nuc}} = \frac{\frac{\pi n_0 d_\mathrm{Nuc}^3}{6}}{1+\frac{\pi n_0 d_\mathrm{Nuc}^3}{6}}, \tag{2.48}$$

$$R_\mathrm{B} = \sqrt[3]{\frac{3}{4\pi n_0}\frac{1+\alpha_\mathrm{Nuc}-\alpha_\mathrm{l}}{\alpha_\mathrm{l}}}. \tag{2.49}$$

Depending on the local properties of the flow, in the matrix of the discretized volume fraction transport equation, the source term can become very large compared to the diagonal part due to the very high phase change rate. This may make solving the discretized equations matrix problematic [11]. In order to improve the solution stability, the source term needs to be rewritten, Equation 2.50, so the diagonal part can take into account some parts of the source term as an implicit term,

$$\frac{\partial \alpha_\mathrm{l}}{\partial t} + \frac{\partial(\alpha_\mathrm{l}\bar{u}_i)}{\partial x_i} = \frac{\dot{m}}{\rho_\mathrm{l}} = \frac{\dot{m}}{\rho_\mathrm{l}} - \alpha_l(\frac{1}{\rho_l}-\frac{1}{\rho_v})\dot{m} + \alpha_l(\frac{1}{\rho_l}-\frac{1}{\rho_v})\dot{m}. \tag{2.50}$$

Considering the non-conservative form of the mass continuty equation, the last term in Equation 2.50 can be replaced with the divergence of velocity,

$$\frac{\partial \alpha_\mathrm{l}}{\partial t} + \frac{\partial(\alpha_\mathrm{l}\bar{u}_i)}{\partial x_i} = (\frac{1}{\rho_\mathrm{l}} - \alpha_l(\frac{1}{\rho_l}-\frac{1}{\rho_v}))\dot{m} + \alpha_l\frac{\partial \bar{u}_i}{\partial x_i}. \tag{2.51}$$

The phase change model can be also decomposed into two terms, one for condensation and the other for vapourization modelling,

$$\dot{m}_{\alpha c} = C_c\alpha_\mathrm{l}\frac{3\rho_\mathrm{l}\rho_\mathrm{v}}{\rho_\mathrm{m}R_\mathrm{B}}\sqrt{\frac{2}{3\rho_\mathrm{l}}}\sqrt{\frac{1}{|p-p_\mathrm{threshold}|}}\max(p-p_\mathrm{threshold},0), \tag{2.52}$$

$$\dot{m}_{\alpha v} = C_v(1+\alpha_{\text{Nuc}}-\alpha_{\text{l}})\frac{3\rho_{\text{l}}\rho_{\text{v}}}{\rho_{\text{m}}R_{\text{B}}}\sqrt{\frac{2}{3\rho_{\text{l}}}}\sqrt{\frac{1}{|p-p_{\text{threshold}}|}}\min(p-p_{\text{threshold}},0), \tag{2.53}$$

$$\dot{m} = \alpha_{\text{l}}\dot{m}_{\alpha v}+(1-\alpha_{\text{l}})\dot{m}_{\alpha c} = \alpha_{\text{l}}(\dot{m}_{\alpha v}-\dot{m}_{\alpha c})+\dot{m}_{\alpha c}. \tag{2.54}$$

By introducing $\dot{V} = (\frac{1}{\rho_l}-\alpha_l(\frac{1}{\rho_l}-\frac{1}{\rho_v}))\dot{m}$ and putting Equation 2.54 inside Equation 2.51, the transport equation can be rewritten as,

$$\frac{\partial \alpha_{\text{l}}}{\partial t}+\frac{\partial(\alpha_{\text{l}}\bar{u}_i)}{\partial x_i} = (\frac{\partial \bar{u}_i}{\partial x_i}+\dot{V}_{\text{v}}-\dot{V}_{\text{c}})\alpha_l+\dot{V}_{\text{c}}. \tag{2.55}$$

Accordingly, the source term is decomposed into two terms where the first one can be considered implicitly to improve the robustness of the solution [41].

2.4.2 Mass transfer modifications

In this study, the symmetric part of the velocity strain rate is proposed to be considered for correction of the local phase change relaxation time scale [61]. It has been observed that in cavitating flows, the vapour production coefficient should be large, as high as possible according to [62], to satisfy near instantaneous vapourization. The destruction term, however, allows for some retardation in the condensation [62]. Therefore, the coefficient modification is limited to the vapourization coefficient, C_{v} where the main flow time scale, $t_\infty = \frac{L_\infty}{U_\infty}$, is employed to normalize the velocity strain rate,

$$C_{\text{v-mod}} = C_{\text{v}}\left(1+t_\infty\left|\frac{1}{2}(\frac{\partial u_i}{\partial x_j}+\frac{\partial u_j}{\partial x_i})\right|\right). \tag{2.56}$$

In order to consider the viscous stresses in liquid rupturing, the maximum eigenvalues of the stress tensor should be considered as the criteria that the flow withstands rupturing or phase change, $\max(\tau_{\text{ij}}) < p_{\text{Sat}}$, where

$$\tau_{\text{ij}} = \begin{bmatrix} -p+S_{11}-\frac{2}{3}\mu\frac{\partial u_i}{\partial x_i} & S_{12} & S_{13} \\ S_{21} & -p+S_{22}-\frac{2}{3}\mu\frac{\partial u_i}{\partial x_i} & S_{23} \\ S_{31} & S_{32} & -p+S_{33}-\frac{2}{3}\mu\frac{\partial u_i}{\partial x_i} \end{bmatrix}. \tag{2.57}$$

As it can be seen from Equation 2.57, calculation of the eigenvalues of the stress tensor for all of the computational cells will demand a significant computational cost. To simplify the calculation, one can use the same methodology used in the turbulence models where the maximum viscous stress tensor is assumed to be of the same order as the shear strain rate, $\dot{\gamma} = \sqrt{2D_{ij}D_{ij}}$. Therefore, the magnitude of stress tensor in its principal coordinates can be estimated by,

$$\left|\tau_{ij}\right| = \left|-p\delta_{ij}+S_{ij}\right| \approx \left|-p\delta_{ij}+\mu\dot{\gamma}\delta_{ij}\right|. \tag{2.58}$$

Using this simplification, the pressure threshold, which determines the onset of cavitation in the flowing fluid, can be written as,

$$p - \mu\dot{\gamma} < p_{\mathrm{Sat}}, \tag{2.59}$$

$$p_{\mathrm{threshold}} = \mu\dot{\gamma} + p_{\mathrm{Sat}} = p_{\mathrm{a}} + p_{\mathrm{Sat}}. \tag{2.60}$$

This added pressure, $p_{\mathrm{a}} = \mu\dot{\gamma}$, is important if either shear strain rate or effective viscosity is large, and comparable with the saturation pressure.

2.5 OpenFOAM package

OpenFOAM (Open Source Field Operation and Manipulation) is an open source code written in C++ to model and simulate fluid dynamics and continuum mechanics. It is possible to adopt the code and build new functionalities, libraries, solvers, and utilities. The software is community driven where various communities are working on different fields of applications.

In OpenFOAM, the spatial discretization is performed using a cell centered co-located finite volume (FV) method for unstructured meshes with arbitrary cell-shapes, and a multi-step scheme is used for the time derivatives. To complete the FV-discretization, the face fluxes need to be reconstructed from grid variables at adjacent cells, requiring interpolation of the convective fluxes and difference approximations for the inner derivatives of the diffusive fluxes; see Weller et al. [63], Jasak [64] and Rusche [65] for more details on the discretization and the numerics used in OpenFOAM. In this work, the OpenFOAM version 2.3.x is used.

InterPhaseChangeFoam is a solver for two incompressible, isothermal, immiscible fluids with phase-change (i.e. cavitation) which uses a phase-fraction based interface capturing approach as described above. The set of phase-change models provided are designed to simulate cavitation but other mechanisms of phase-change are supported within this solver framework. Turbulence modelling is generic, i.e. laminar, RANS, or LES may be selected. More details about this solver can be found in the open access literature [66].

3

Studied Cases

This chapter provides an overview of the geometry and computational conditions of the benchmarks and cases studied. For each case, details of the geometry, flow condition, computational domain, and the spatial meshes are presented. A brief description of the experimental tests and measurements are also included.

3.1 DELFT TWISTED HYDROFOIL

Twisted foils are considered and tested to improve the knowledge regarding the three dimensional effects on the cavitation and its characteristics such as interactions of the cavity with re-entrant jets, cavitation collapse, noise, vibration, and erosion risk. These foils generate cavitation which more or less resembles propeller cavitation but in a more well defined and easily studied set up, which makes it an attractive test case for evaluation of computational approaches for predicting cavitation. Due to the spanwise variation of the angle of attack in these foils, the sheet cavity is three-dimensional and the closure line of the cavity is convex-shaped.

For this study, the Delft Twisted hydrofoil is selected as the benchmark for 3D sheet and cloud cavitation simulation in order to provide further insights about the dynamics of cloud cavitation and the spatial mesh requirements for its numerical simulations. The experimental tests of this hydrofoil were carried out in steady and unsteady inflow conditions in the cavitation tunnels at Delft Technical University, see [67, 68, 69]. The numerical results of this benchmark are compared with the experimental measurements, and are presented in the Paper A and Paper B.

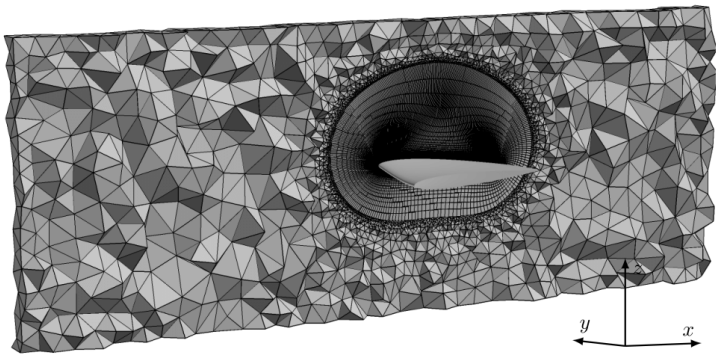

Figure 3.1: Computational domain of the twisted hydrofoil simulation

3.1.1 Geometry

The hydrofoil tested at the Delft Technical University consists of a NACA0009 profile, with chord length, C, equal to 150mm, that has a spanwise varying angle of attack, ranging from zero degree at the cavitation tunnel wall to 11 degrees at the center line and then back to zero degree symmetrically with respect to the center plane, with a total span of two chord length [69]. For the current study, simulation of the foil having -2 degree angle of attack is conducted. Taking advantage of the symmetry, only half of the domain is considered for numerical simulation. The computational domain extends $6.5C$ in the streamwise direction, starting $3C$ upstream of the leading edge and ending $2.5C$ behind the trailing edge. The sizes of the computational domain are selected according to instructions provided in the second international symposium on marine propulsors.

3.1.2 Flow conditions

A standard fixed inflow boundary condition is used at the inlet where the flow velocity is set equal to $6.97\,\mathrm{m\,s^{-1}}$, giving $Re = 1.05 \times 10^6$. At the outflow boundary a fixed pressure of 2970 Pa is used, setting the outlet cavitation number equal to 1.07. At the upper, lower, and side walls of the tunnel, slip boundary condition is employed. Symmetry plane is used at the center of the tunnel, and a no-slip boundary condition is specified on the hydrofoil surface.

3.1.3 Computational mesh description

Structured surface mesh is used on the foil surface, along with the extrusion method to create appropriate computational grids around the foil. The number of layers is selected large enough to be able to use tetrahedral cells far from the foil. This will decrease the mesh concentration in regions that are not disturbed by the foil and therefore less interesting physics are happening there to be captured, Figure 3.1.

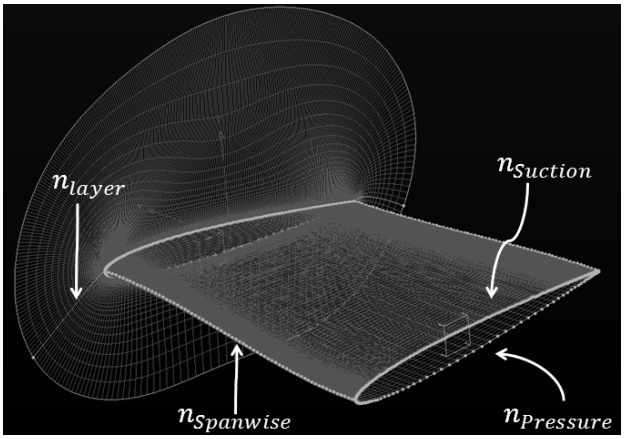

Figure 3.2: Cell number notation definition for Twisted foil

The mesh resolution study is categorized into two parts. The first part focuses on the mesh dependency study based on the wetted flow analysis and the second part focuses on the mesh resolution effects on the cavitation simulation. All of the meshes are generated by using the Pointwise software.

In the wetted flow mesh dependency study, at first the effects of the streamwise and spanwise resolutions (called surface mesh resolution in this work) on the flow prediction are investigated while keeping the wall normal resolution constant ($y^+ = 50$). In Table 3.1, name, size and specifications of the mesh resolutions used for surface mesh dependency study of the first part are presented. Four different surface mesh resolutions are considered with constant $y^+ = 50$. In this table, n_{suction} is the number of cells on the suction side of the foil in the streamwise direction, n_{spanwise} is the number of cells in the span direction, n_{layer} is the number of layers of extruded cells, Figure 3.2. It should be noted that since the gradient of the pressure and velocity at the leading edge are much higher than in other regions of the foil, the mesh points are clustered towards the leading edge. Moreover, the number of cells on the pressure side in the streamwise direction is kept constant, 70, in all of the meshes. The numbers $n_{\text{structured}}$ and n_{total} represent the number of structured and total volumetric cells.

Table 3.1: Surface mesh specification for mesh dependency study, $y^+ = 50$

Mesh	n_{suction}	n_{spanwise}	n_{layer}	$n_{\text{structured}}$	n_{total}
T11-I	70	70	34	367k	658k
T11-II	140	70	34	478k	818k
T11-III	280	70	80	1932k	2461k
T11-IV	560	140	80	7005k	8733k

In order to investigate the effects of the first mesh height and its interactions with the selected wall model, five different y^+ have been selected and tested in the

wetted flow mesh dependency study, presented in Table 3.2. For these resolutions, the surface mesh resolution is the same as mesh T11-III in Table 3.1.

Table 3.2: Mesh specification for mesh dependency study with different y^+

Mesh	T11-V	T11-III	T11-VI	T11-VII	T11-VIII
y^+	100	50	30	5	1

In the second part, the mesh resolution obtained from the wetted flow mesh dependency analysis is considered as the base mesh and effects of the mesh resolution refinements on the cavitation prediction is investigated. Ten different mesh resolutions are considered. The resolution in streamwise, spanwise and normal to the wall is varied while keeping $y^+ = 1$. The specifications of these mesh resolutions are presented in Table 3.3. Numerical results of four of these resolutions, called (T11-A, T11-B, T11-C, T11-D), are presented in detail, and the others are employed to support the analysis and for the uncertainty analysis of the results. It should be noted that the Mesh T11-A has the same resolution as mesh T11-VIII. It can be seen from the table that mesh T11-B has four times finer surface mesh resolution comparing to mesh T11-A while the normal mesh distribution has been kept the same. Mesh T11-C and T11-D have the same surface mesh as Mesh T11-A and Mesh T11-B respectively, but with finer mesh resolution in the normal to the wall direction. Here, normal to the wall resolution does not imply just on the first cell height. For all of the cases in this section, the y^+ value is kept lower than one. Then, by varying the extrusion coefficient, different resolutions in the normal direction are created. It should be noted that the number of cells on the pressure side in the streamwise direction is kept constant, 70, for all of the meshes. Detailed information about the numerical setting and procedure used is provided in Paper A and B.

3.2 Elliptical hydrofoil

The tip vortex flow around the Arndt elliptical foil is selected as a benchmark in order to gain insight about the tip vortex formation and development, as well as the requirements for numerical simulation of this type of flow. This elliptical foil is often used for experiments and analysis of vortex cavitation. The foil has been tested at different institutes in various operating conditions both in wetted and cavitating conditions [21, 70, 71, 30].

The numerical study conducted on this foil consists of LES simulations of the cavitating tip vortex presented in Paper C, tip vortex inception analysis presented in Paper D, and evaluation of curvature correction models in the SST $k-\omega$ framework presented in Paper E. In these studies, the experimental data measured in the cavitation tunnel in the Laboratory for Ship Hydrodynamics at Delft Technical University [71, 30] is selected for comparison with the numerical results.

Table 3.3: Mesh specification for cavitation simulation, $y^+ = 1$

Mesh	n_x	n_z	x^+	z^+	n_{layer}	$n_{struct}(M)$	$h_{v,i}$	$n_{total}(M)$
T11-A	280	70	82	324	80	1.57	2.15	2.46
T11-A1B	330	85	69	267	80	2.25	1.91	3.41
T11-A2B	420	105	54	216	80	3.53	1.64	5.12
T11-B	560	140	41	162	80	6.27	1.36	7.64
T11-C	280	70	82	324	200	3.92	1.59	5.37
T11-C1D	330	85	69	267	200	5.61	1.41	7.44
T11-C2D	420	105	54	216	200	8.82	1.21	11.23
T11-D	560	140	41	162	200	15.68	1.00	19.28
T11-A	280	70	82	324	80	1.57	2.15	2.46
T11-A1D	330	85	69	267	105	2.95	1.75	4.21
T11-A2D	420	105	54	216	140	6.17	1.36	8.18
T11-D	560	140	41	162	200	15.68	1.00	19.28

3.2.1 Geometry

The geometry of the foil is an elliptical planform having a NACA $66_2 - 415$ cross section. Having NACA 6 series section introduces a low adverse pressure gradient over the foil and therefore longer laminar boundary layer.

The trailing edge of the foil was truncated at a thickness of $0.3mm$ due to manufacturing limitations where the root chord length after truncation is $C_0 = 0.1256m$. The total area of the foil obtained from the 3D CAD model is $0.01465m^2$ which is used as the reference area to compute non-dimensional parameters, e.g. lift coefficient. The foil has a half span of $150mm$, so that the tip is positioned in the centre of the test section. The foil is also placed in the middle of the channel width where distance to each side is equal to $150mm$ [71].

3.2.2 Flow conditions

For the selected conditions, the inlet velocity is $6.8\,\mathrm{m\,s^{-1}}$ which corresponds to a Reynolds number of 8.95×10^5. The foil has been analyzed at three different angles of attack, 9°, 7° and 5°, where in this study the results of AOA equal to 9° are included.

3.2.3 Computational mesh description

The computational domain mimics the cavitation tunnel dimensions where the inlet is placed approximately four chord lengths in front of the foil, and the outlet is placed ten chord lengths behind the foil, Figure 3.3. In order to systematically

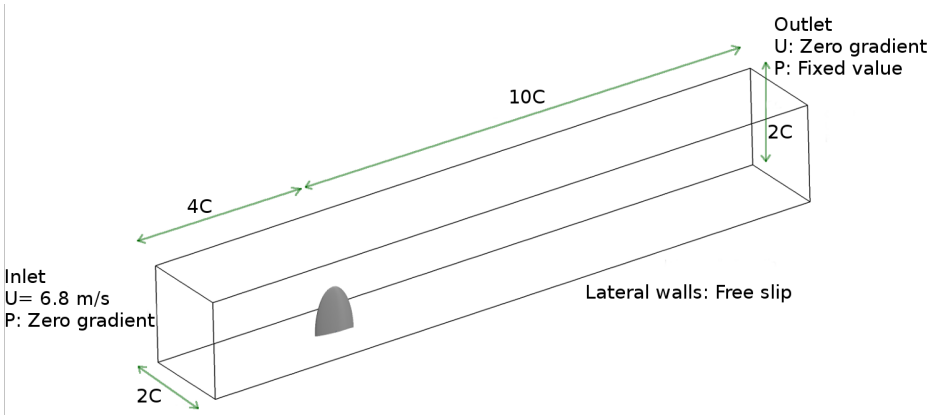

Figure 3.3: Boundary positions

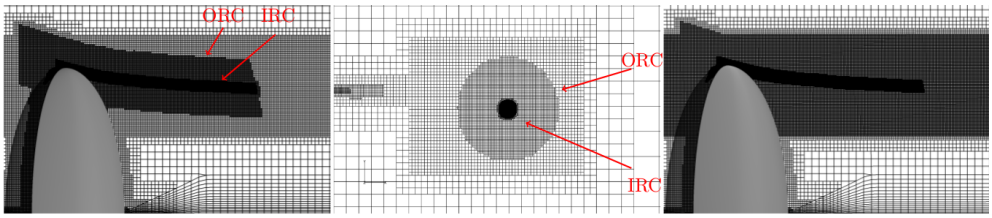

Figure 3.4: Mesh distribution in streamwise and inplane directions, ORC: Outer Refinement Cylinder, IRC:Inner Refinement Cylinder

investigate the spatial resolution requirement for numerical analysis of the tip vortex, employing hexahedral cells at the tip vortex region is considered. To address this, StarCCM+ of Siemens PLC is used to generate the mesh.

In the first step, a coarse mesh without refinement of the tip vortex region is generated. The flow is simulated to find an approximate tip vortex trajectory. The trajectory path is then exported into StarCCM+ to define a priori refinement zones. Two cylindrical regions are considered around the trajectory path to specify the mesh resolution, having 10 mm for inner refinement cylinder (IRC) and 60 mm for outer refinement cylinder (ORC) diameters, respectively. As the objective is to investigate the mesh requirement for vortex prediction in the near field region, these cylindrical refinement regions are extended 1.5 chord lengths downstream of the foil. In Figure 3.4, cell distribution in the streamwise and inplane sections are presented.

The boundary layer in all of the resolutions are fully resolved in the wall normal direction, $y^+ \leqslant 1$. Prismatic cells having 20 layers with an extrusion factor of 1.15 are used to provide appropriate boundary layer resolution around the foil. The base mesh resolution on the foil follows $x^+, z^+ < 250$. However, in the relevant tip region, the refinement regions also affect the surface resolution and higher mesh density is achieved.

To investigate the inplane and streamwise mesh requirements, five different resolutions are created. The surface resolution and prismatic layers ($y^+ = 1$) of

these meshes are the same, and the only difference between them is the resolution of the inner refinement cylinder, Figure 3.4. The specifications of these meshes are presented in Table 3.4. For the coarsest resolution, P1S1, Taylor length scale is selected as the streamwise resolution. The inplane resolution is selected as half of the Taylor length scale in order to provide at least 8 cells in the vortex core. Then, two more meshes are created with the same streamwise resolution but finer inplane resolution, P2S1 and P3S1. For the streamwise mesh resolution study, P2S1 is selected as the base resolution, and is refined in the streamwise direction to obtain P2S2 and P2S3 meshes. In order to investigate effects of foil wake on the vortex roll-up, the mesh resolution of P2S2 is also refined in the the wing wake region, so called P2S2-Wake.

It should be noted that the inner refinement cylinder also covers the tip surface of the foil. Therefore, the surface resolution in that region follows the inner refinement cylinder resolution.

Table 3.4: Mesh specifications for mesh dependency study of the elliptical foil

Resolution	Name	Total number of Cells (M)	In-plane cell size (mm)	Streamwise cell size (mm)	Cells in vortex radius
In-Plane	P1S1	8.3	0.125	0.25	8
	P2S1	24.4	0.062	0.25	16
	P3S1	88.3	0.031	0.25	32
Streamwise	P2S1	24.4	0.062	0.25	16
	P2S2	44.3	0.062	0.125	16
	P2S3	84.9	0.062	0.062	16
Wake	P2S2-Wake	48.5	0.062	0.125	16

3.3 E779A PROPELLER

The INSEAN E779A model propeller is a modified Wageningen B-series propeller characterized by a constant pitch distribution and very low skew. The propeller has been extensively tested experimentally at the Italian Ship Model Basin, INSEAN, and there are some numerical results published for this propeller at different operating conditions [72, 73]. The experimental data and operating conditions of the tested propeller are reported in [74, 75, 76]. The propeller is selected as a benchmark to validate the numerical simulation of propellers in wetted and cavitating flow conditions.

3.3.1 Geometry

E779A propeller has four blades with a uniform pitch (pitch/diameter = 1.1), a forward rake angle of 4 degrees with the diameter of 227.2 mm, Figure 3.5.

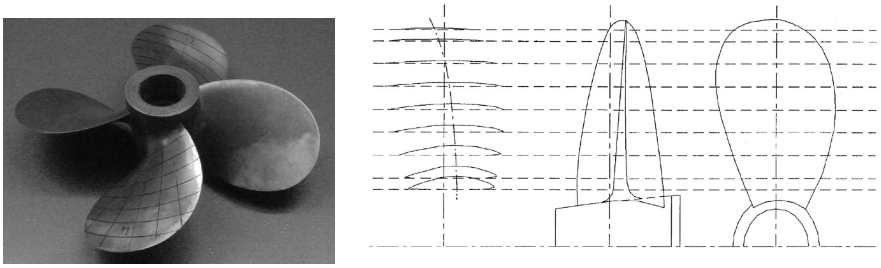

Figure 3.5: E779A propeller

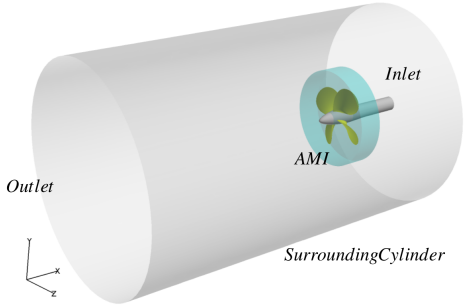

Figure 3.6: Boundaries setting for E779A propeller simulation

The numerical domain is simplified to a cylinder extending one D_p upstream the propeller and 3.75 D_p downstream of the propeller. The surrounding cylinder has the radius of 0.334 m, yielding the same cross-sectional area as the cavitation tunnel, Figure 3.6.

3.3.2 Flow conditions

The flow around the E779A is simulated in three different conditions presented in Table 3.5. In order to validate the employed settings, moving mesh strategy, and to check the quality of the mesh, the wetted flows are simulated at two different J values, and then for $J = 0.71$ the cavitating flow is simulated. For the cavitating flow, the outlet pressure is adjusted to meet the cavitation number equal to $\sigma_n = 1.76$.

Table 3.5: Simulation conditions of E779A propeller

J	n (rps)	Inlet velocity (m/s)	Cavitation number
0.88	25	5	Wetted Flow
0.71	36	5.808	Wetted Flow
0.71	36	5.808	1.76

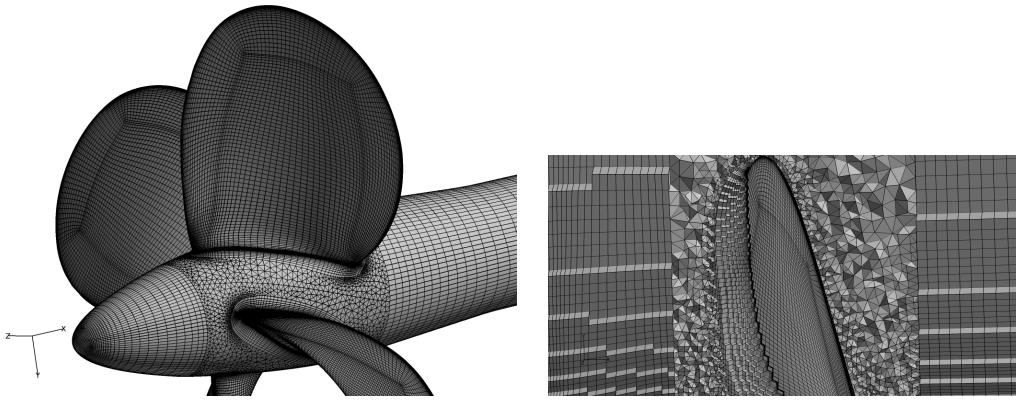

(a) Blade surface mesh (b) Blade prism mesh

Figure 3.7: Mesh specification of E779A propeller

3.3.3 Computational mesh description

The computational grids have approximately 3.65 million cells composed of tetrahedral cells with prisms in the boundary layer region of the blades, see Figure 3.7. In order to appropriately capture the boundary layer over the blades, the surface mesh is extruded normal to the surface to create the prisms cells. The non-dimensionalized height of the first cell (y^+) is set equal to 10 except near the leading edge, where higher velocities lead to slightly higher values.

3.4 PPTC PROPELLER

The Potsdam Propeller Test Case (PPTC) is used as the reference geometry of the 2nd International Workshop on Cavitating Propeller Perfomance (2015). The focus of the current simulation is on the second case of the workshop, Cavitation Observation in Oblique Flows.

3.4.1 Geometry

The propeller is a model scale, five bladed propeller with a diameter equal to $D =$ 250 mm. The geometry of the propeller including general information, propeller data sheet and also propeller description by radius is open-access and can be found on the webpage of the workshop [77, 78]. The open water experimental tests have been carried out for wetted and cavitating flows by SVA Potsdam GmbH in the cavitation tunnel K 15 A where the propeller was positioned with 12 degrees inclination towards the inflow direction.

Table 3.6: Case2 of SMP 2015 operating conditions

Case	J	σ_n	$V_{inlet}(m/s)$	n (rev/s)
2.1	1.019	2.024	5.095	20
2.2	1.269	1.424	6.345	20
2.3	1.408	2.0	7.04	20

3.4.2 Flow conditions

The operating conditions are presented in Table 3.6, where the open water performance of the propeller in wetted and cavitating flows is predicted for three operating conditions ($J = 1.019, 1.269$ and 1.408). The same settings and approaches used in the modelling of E779A propeller are employed here to simulate the PPTC propeller.

3.4.3 Computational mesh description

The blade surface mesh consists of quad surfaces which have been extruded in the wall normal direction, $y^+ = 5$, to create prism cells. The rest of the domain is filled with unstructured tetrahedral cells. Since the flow has higher gradients near the leading and trailing edges and also near the tip region of the blades, the mesh has finer resolution at these parts. In order to keep the mesh size in a reasonable range, the mesh gets coarser with increasing distance from the blades. The total size of the mesh is around 4.7 M cells, called SMP-Mesh-I. For this mesh, the domain size of the tunnel has been kept the same as the geometry provided by the workshop committee, where the inlet is located only 2D upstream of the propeller where D is the diameter of the propeller. Since the inlet is relatively close to the propeller, it is possible that using uniform inflow as the inlet velocity boundary condition affects the flow around the propeller (e.g. pressure distribution and cavitation pattern). Therefore, another mesh is also created where the inlet is moved 4D further upstream, SMP-Mesh-II. In order to investigate the effects of the mesh resolution on the results, SMP-Mesh-III is created from SMP-Mesh-II where each prism cell around one blade is split into 8 equal cells.

3.5 ROLLS-ROYCE (RR) HIGH SKEWED PROPELLERS

Four different designs of RR propellers are considered, and their performance is investigated in wetted and cavitating flows. The first two designs, propeller A and propeller B, are compared in inclined conditions, while the cavitation inception properties of the other two designs, propellers C and D, are analyzed in open water conditions. The results of propellers A and B are presented in [41], and the analysis of propeller C and D is provided in the paper E and paper F.

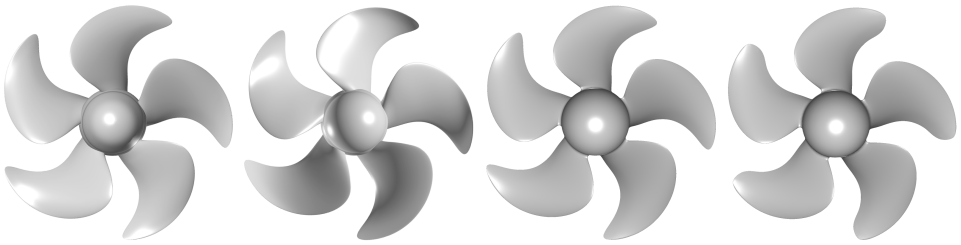

(a) Propeller A (b) Propeller B (c) Propeller C (d) Propeller D

Figure 3.8: Geometries of Rolls-Royce high skewed propellers

3.5.1 Geometry

The basic design of the propellers is from a highly skewed propeller research series which has low effective tip load and are typical for yachts and cruise ships, where it is very important to suppress and limit propeller-induced vibration and noise. In this type of propeller, the main source of noise and vibration is the vortex cavitation in the tip region. The tip vortex cavitation, and therefore noise and vibration, is sensitive to modification of the blade's geometry in the tip region. In order to investigate the influence of tip shape and loading on the cavitation behaviour, different designs have been suggested and tested at the RRHRC cavitation tunnel, the Hydrodynamics Research Centre of Rolls-Royce AB, Kristinehamn, Sweden. The current analysis is the continuation of the previous research on these propellers [79].

In Figure 3.8, general sketches of the propellers are presented. Propellers A and C are Rolls-Royce standard high skew propellers, with a low tip load and similar skew. Propeller B is a standard high skew design, with the same skew as for propellers A and C, modified by forward rake at the outer radius. Propeller D has the same geometry as propeller C for most of the blade except that the geometry differs at the tip. The sections close to the tip of propeller D are shorter and are loaded differently. The pitch is also changed slightly. This results in a lower tip loading in propeller D compared to propeller C. Propeller A is designed in a way to have the same effective tip load as propeller D, but with the same section definition at all radii.

3.5.2 Flow conditions

After mounting the propeller, the operating condition is set by adjusting the water velocity, revolution rate of the propeller and the pressure of the tunnel. A pitot tube mounted on the lower part of the side wall of the tunnel measures the inflow velocity. In the inclined setup of the cavitation tunnel, the water flows from the left side to the right side with a constant velocity. The propeller shaft is inclined towards the water flow direction by 10 degrees, Figure 3.9.

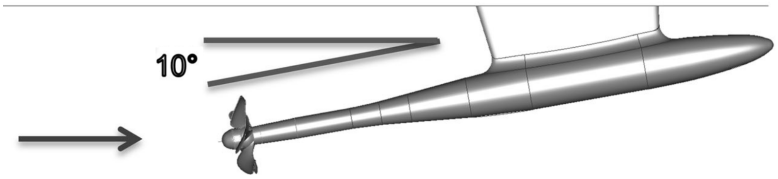

Figure 3.9: Inclined propeller towards the incoming flow in the experiment setup of propeller A and B

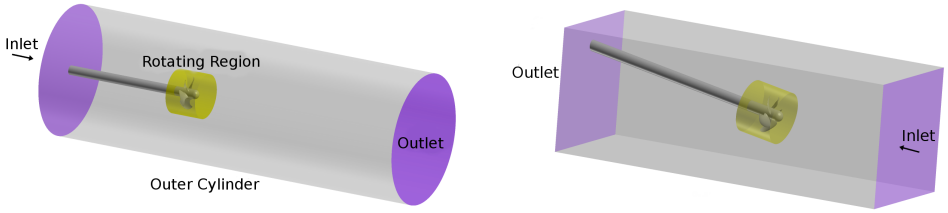

(a) OW condition (b) Inclined condition

Figure 3.10: Computational domain of the RR propellers

3.5.3 Computational mesh description

The computational domains of the propellers are presented in Figure 3.10. Similar to previous propellers simulations settings, the computational domains have been decomposed into two regions connected to each other through AMI (Arbitrary Mesh Interpolation) boundaries. While the outer region is stationary, the rotation of the region close to the propeller has been handled either by solid body motion with sliding mesh for unsteady computations or by MRF for steady computations. In the OW simulations, the domain is simplified to a cylinder extending 4D upstream the propeller and 8D downstream of the propeller where D=0.2543 m is the diameter of the propeller. In the inclined setup, the inflow is located 2.5D upstream of the propeller, and the outflow is located 5D downstream of the propeller. The constant inflow velocity (4.2 m/s) is set as inlet velocity boundary condition, and constant pressure is employed as outlet pressure boundary condition to set the flow Reynolds and cavitation numbers.

As for the propellers A and B, analysis of the cavitation pattern is the main objective of the numerical modelling, similar spatial mesh resolutions to the previous study, e.g. PPTC propeller, are generated. The grid type of the propeller A is named CoarseII in [79]. The near wall resolution of the blade is around $y^+ = 30$ and therefore a wall model is used. The computational domain of the propeller A consists of 8.7 million cells which are composed of tetrahedral cells with prism layers of hexahedral cells around the blades, hub and shaft, Figure 3.11. The mesh is named Mesh-RR-A-1 in this study.

For the propeller B, two different mesh structures are considered. The first

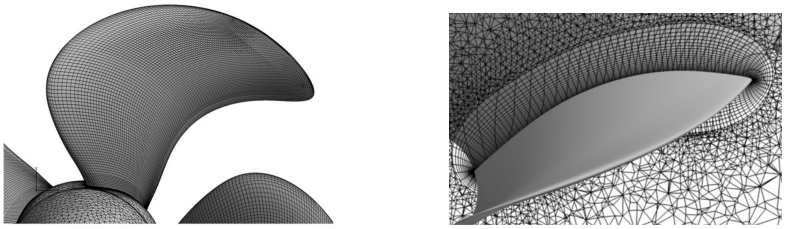

Figure 3.11: Surface mesh and closed-up views of volume mesh around the blades of the the propeller A

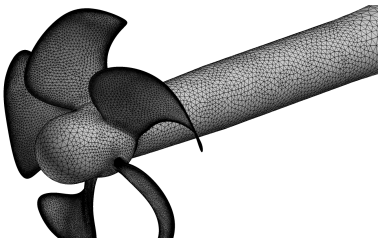

Figure 3.12: Triangular surface mesh of the propeller B, Mesh-RR-B-2

mesh, Mesh-RR-B-1, is created by using the same mesh topology as used for propeller A, employing the quad surfaces on the blades surfaces, and then extrusion of this surface mesh to create prismatic layers around the blades and at the last step, using tetrahedral cells to fill the rest of the domain where the total mesh size is around 7.5 M cells. For this mesh, the near wall resolution of the mesh (y^+) is around 20. The second mesh topology, Mesh-RR-B-2, is composed of triangular prisms near the blades and tetrahedral cells in the rest of the computational domain, totally 13.7 M cells. The surface mesh distribution of this mesh is presented in Figure 3.12. For both of the meshes, the mesh is finer near the leading edge, trailing edge and also tip of the blades in order to capture more physics of the flow in these regions.

In Figure 3.13, the mesh topology of propellers C and D, generated in StarCCM+, is presented. Different refinement boxes are applied in StarCCM+ to provide finer resolution around the propeller rotating region, Figure 3.13a. Generated mesh resolutions provide fully resolved boundary layers on the propeller blades in the wall normal direction, $y^+ \leqslant 5$, with prismatic layers consisting of 20 layers and having an extrusion factor of 1.15. The baseline mesh resolution on the blades surfaces follows, $x^+, z^+ < 250$, where finer resolutions are provided at the leading edge and trailing edge of the blades.

The tip vortex refinement is applied on one blade only, where three helical shape refinement zones are defined based on the primary vortex trajectory, Figure 3.14. The refinement regions cover the tip of the blade, and therefore provide finer surface resolutions at the tip of the refined blade, Figure 3.13b. These helical refinement regions provide spatial resolutions as fine as 0.2 mm, 0.1 mm, and 0.05 mm in H1, H2, and H3 regions, Table 3.7.

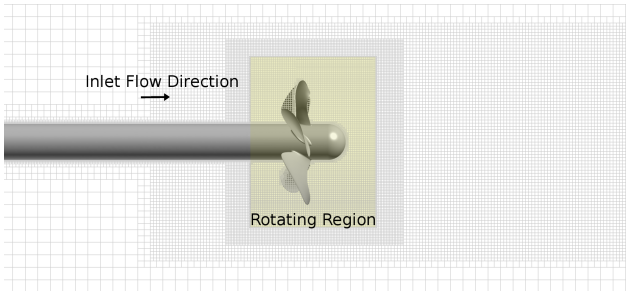

(a) Streamwise resolution

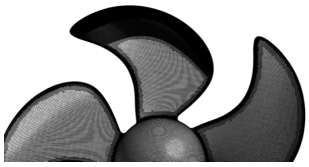

(b) Blade surface resolution

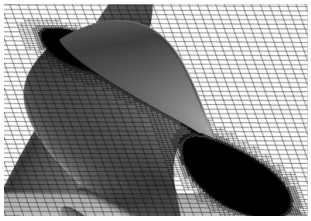

(c) Prismatic layers

Figure 3.13: Mesh distribution in streamwise directions, RR propellers, OW condition

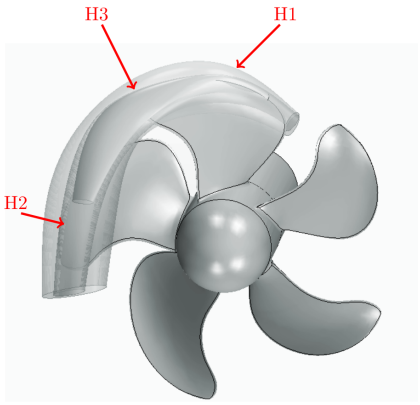

Figure 3.14: Three layers of refinement in the tip vortex region, RR propellers, OW condition

Table 3.7: Rolls-Royce propellers C and D mesh specifications

Name	Total number of Cells (M)	Total number of Faces (M)	Tip vortex grid resolution (mm)
Propeller C - OW	122	365	0.05
Propeller D - OW (H2)	37	112	0.1
Propeller D - OW (H3)	119	359	0.05

4

Tip Vortex

The chapter includes the analysis of tip vortex flow around the elliptical foil in order to determine the possibility of using CFD to support advanced propeller design work. The vortex structures around this type of foil resembles the propeller tip vortex behaviour while making it possible to be tested in more details both experimentally and numerically. The tip vortex at the selected operating conditions is relatively stationary which reduces the computational requirements [80, 81].

The first part of the study contains the analysis of the spatial mesh resolution requirements for simulation of tip vortex flows in the near field region. The streamwise, inplane, and wake resolution effects on the prediction of the tip vortex and its development are investigated. The second part of the chapter focuses on the effects of the turbulence modelling. Two sub-grid scale closure models of LES, ILES and LDKM, are considered, and dependency of the tip vortex prediction on the sub-grid model is analyzed. In the last part of the chapter, effects of the curvature correction models on the tip vortex prediction by the RANS SST $k-\omega$ model is discussed. The results of this chapter are presented in the paper C and paper E.

4.1 SPATIAL MESH RESOLUTION DEPENDENCY

In Figure 4.1, the tip vortex properties at the vortex core for different inplane resolutions are presented. The cavitation index curves, Figure 4.1a, show that all of the selected inplane resolutions predict negative pressure in the region close to the tip ($z/C < 0.2$). However, the negative pressure predicted by P2S1 and P3S1 is almost twice the value predicted by P1S1. While the vortex core pressure of P1S1 becomes positive after $z/C > 0.35$, the other two resolutions predict negative pressure at the core until the end of the refined zones, $z/C = 1.6$. The minimum pressure predicted by P2S1 and P3S1 are almost the same, but the region of this minimum pressure is larger in P3S1. Close to the end of the refinement region,

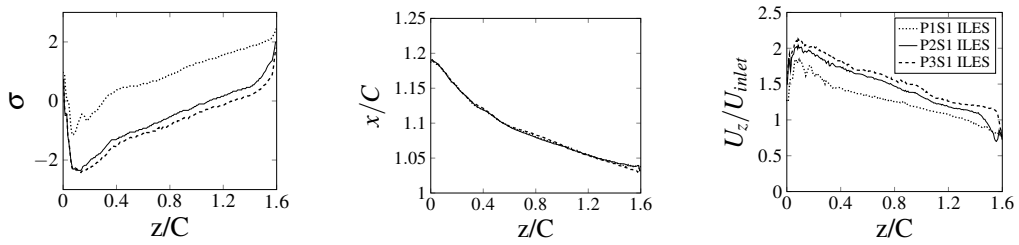

(a) Cavitation index (b) Vortex trajectory (c) Axial velocity

Figure 4.1: Variation of vortex core properties, different inplane resolutions, AOA = 9 deg, ILES results

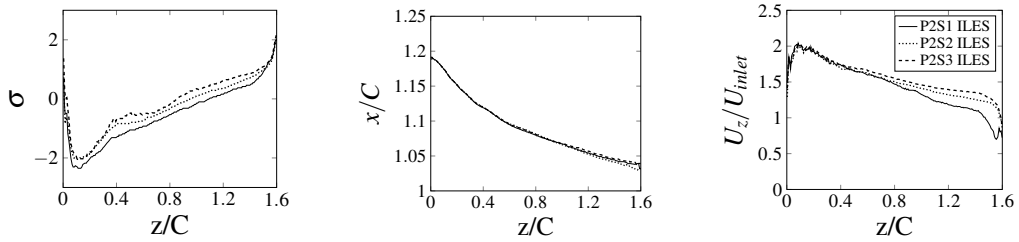

(a) Cavitation index (b) Vortex trajectory (c) Axial velocity

Figure 4.2: Variation of vortex core properties, different streamwise resolutions, AOA = 9 deg, ILES results

$z/C > 1.5$, all of the resolutions show a sudden increase in the pressure. The main reason of this sudden change is an impact of the coarse resolution outside the refined zone into the upstream region. Comparison of the vortex trajectories, Figure 4.1b, shows similar prediction by different inplane resolutions. Slight difference at the centre region, $0.6 < z/C < 1.0$, is considered to be due to the foil wake flow roll-up contributions into the tip vortex development.

All of the considered inplane resolutions are able to capture the accelerated axial velocity at the centre of the vortex, Figure 4.1c, where the location of the maximum velocity corresponds to the location of the minimum pressure.

Figure 4.2 presents the results of streamwise mesh variations while inplane resolution is kept constant and equal to the P2 resolution. Results show that the effects of the streamwise resolution on the tip vortex prediction is less than the inplane resolution. This is related to the fact that the flow variations in the inplane section of the tip vortex due to the rotational nature of the vortex is larger than the variations in the streamwise direction.

The pressure distributions predicted by P2S1, P2S2, and P2S3 resolutions show similar trend, even though the pressure predicted by P2S1 is slightly lower than the two other resolutions, Figure 4.2a. Contradictory to the inplane resolution variation where increasing the inplane resolution leads to lower pressure at the vortex centre, increasing the streamwise resolution leads to slightly higher pressure in the vortex core. Having higher streamwise resolution also leads to

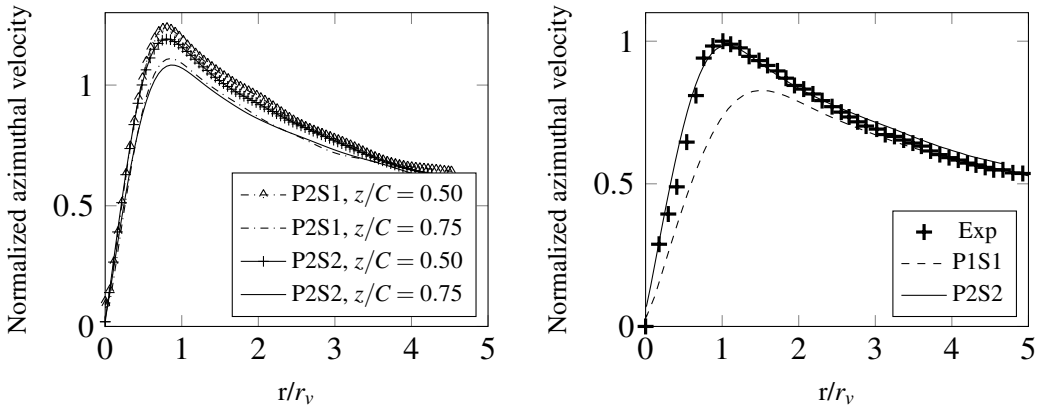

(a) z/C=0.5, 0.75 (b) z/C=1.14

Figure 4.3: Variation of the normalized azimuthal velocity at the vortex core region, ILES, wetted flow results. The vortex core radius is normalized by $r_v = 1.1mm$, and the velocity is normalized by $u_\theta = 6.7m/s$.

prediction of higher axial velocity, Figure 4.2c. This means that increasing the streamwise resolution leads to prediction of lower rotational velocity, Figure 4.3.

P2S1 resolution, which has the coarsest streamwise resolution, shows more rapid decrease of the axial velocity, especially after $z/C > 0.8$. The maximum axial velocity predicted at the centre of the vortex by different streamwise resolutions are similar, almost twice the inlet velocity. According to the mesh resolution investigation, P2S2 resolution is considered to be suitable to capture the physics of the vortex at reasonable computational cost.

In Figure 4.4 and Figure 4.5, the velocity distributions at three different sections downstream of the foil are presented and compared with the experimental PIV data. The sections are $z/C = 0.5$, 075, and 1.14. PIV images are derived by employing sum of correlation (SOC) conditional weighted averaging of experimental measurements, see [71], while the numerical results are time averaged. Therefore, a small portion of the discrepancy between numerical results and experimental measurements are related to the difference in the averaging methods. It is however anticipated that the agreement would improve if the same averaging would have been used.

Axial velocity distribution shows that the numerical approach can accurately predict the accelerated velocity at the centre of the vortex. The vortex roll-up which can be seen in the increase of the axial velocity between z/C $= 0.5$ and z/C $= 0.75$, is slightly under predicted in the numerical simulations. One possible reason for this can be the coarse resolution in the wake region of the foil. The results clearly show that employed numerical tool, i.e. grid, turbulence closure model, and numerical schemes, are well suited together to predict the tip vortex flow.

The distributions of vortex properties, Figure 4.6, show that the pressure and axial velocity predicted by P2S2-Wake resolution is lower than predictions of the

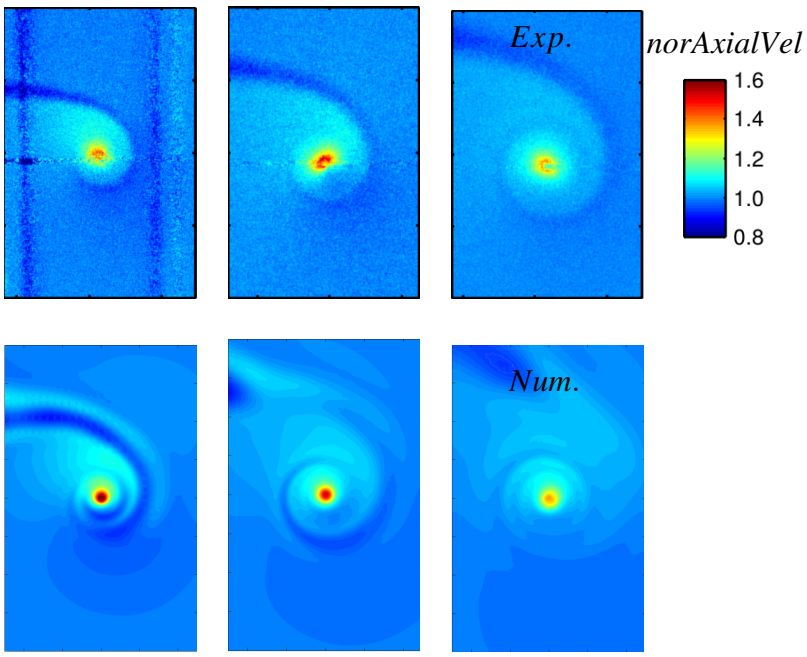

(a) $z/C = 0.5$ (b) $z/C = 0.75$ (c) $z/C = 1.14$

Figure 4.4: Comparison of normalized axial velocity between experimental PIV data and numerical results of P2S2 ILES

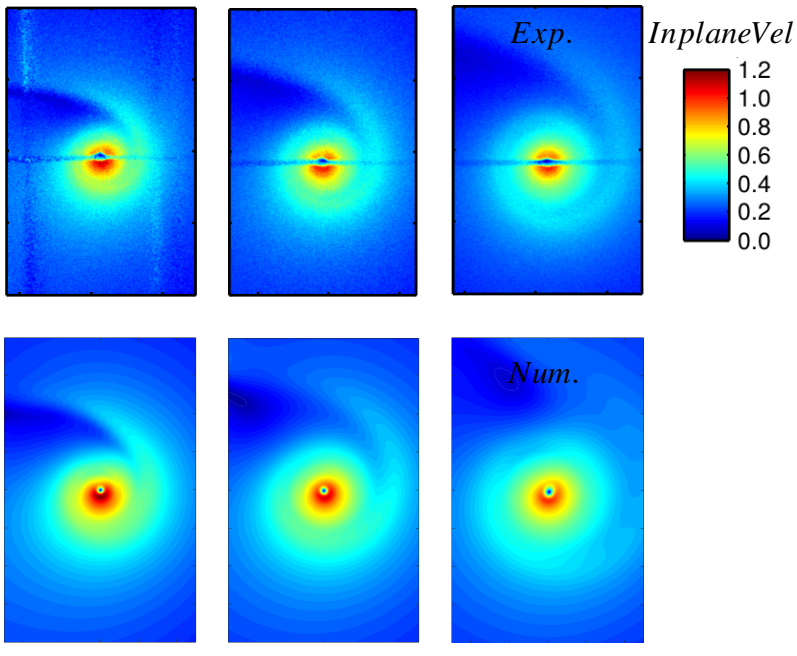

(a) $z/C = 0.5$ (b) $z/C = 0.75$ (c) $z/C = 1.14$

Figure 4.5: Comparison of normalized inplane velocity between experimental PIV data and numerical results of P2S2 ILES

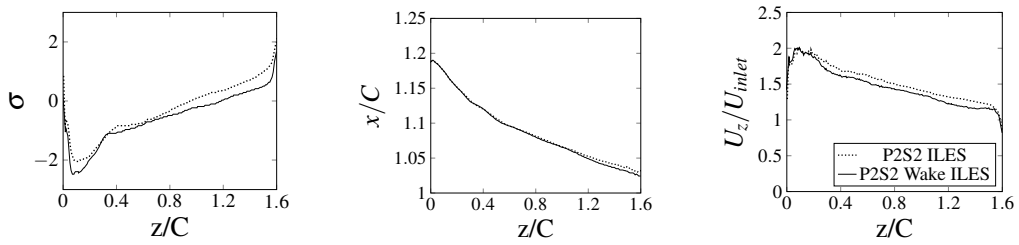

(a) Cavitation index (b) Vortex trajectory (c) Axial velocity

Figure 4.6: Variation of vortex core properties, P2S2 and P2S2-Wake resolutions, ILES, AOA=9°

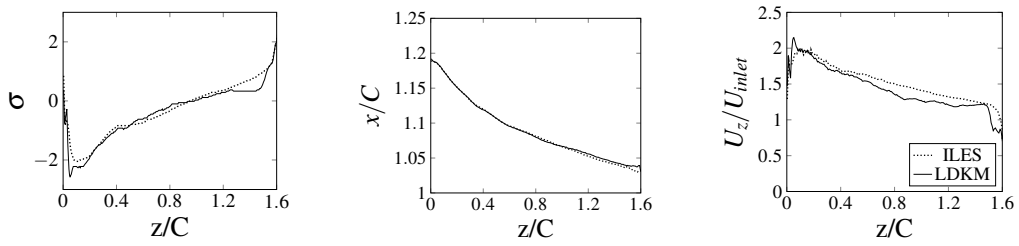

(a) Cavitation index (b) Vortex trajectory (c) Axial velocity

Figure 4.7: Variation of vortex core properties, ILES and LDKM, P2S2

P2S2 resolution. The main reason for presence of lower pressure in P2S2-Wake can be correlated to the azimuthal velocity.

4.2 LES SUB-GRID SCALE MODELLING

The comparison of vortex properties between the ILES and LDKM results are presented in Figure 4.7. The pressure prediction at the vortex core is similar for these two models except close to the foil, $z/C < 0.2$, where LDKM shows lower pressure prediction. Close to the end of the refinement region, $z/C < 1.4$, LDKM is more sensitivity to the mesh size variation. The contribution of the mesh size variation can also be observed at the vortex trajectory prediction. In $0.4 < z/C < 1.4$ region, it can be observed that the decay rate of the accelerated velocity is higher in LDKM, leading to lower axial velocity predictions by LDKM comparing to ILES predictions.

No obvious difference is found between the Q distributions of the LDKM and ILES, Figure 4.8. Both of the models show that the boundary layer separates in the region around $z/C = 0.6$. Similar structures are also found in the instantaneous and averaged Q fields. The tip-zoomed view of Q clearly indicates that close to the tip, the flow is dominated by very small structures and is fully three dimensional, similar to the findings of Stinebring et al. [82].

In Figure 4.9, the distribution of azimuthal velocity at $z/C = 1.14$ is presented. The comparison shows that both models have predicted the velocity distribution

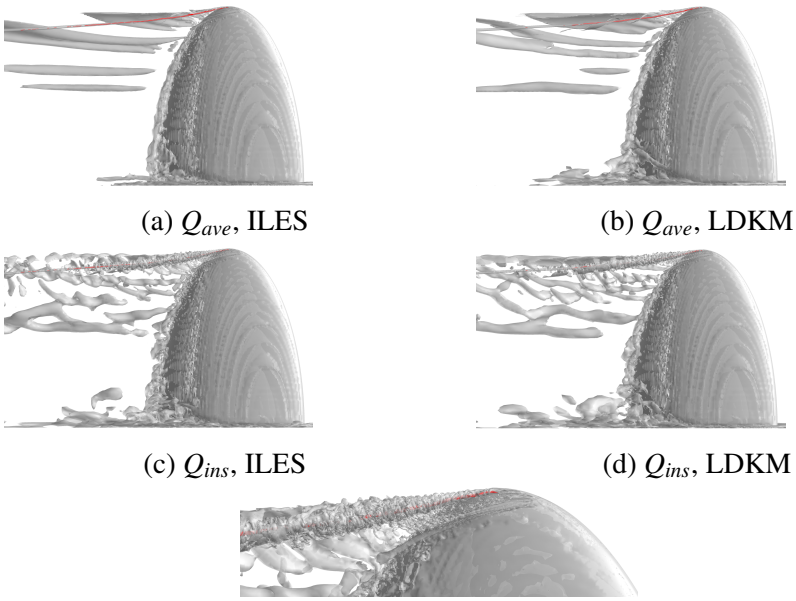

(a) Q_{ave}, ILES (b) Q_{ave}, LDKM

(c) Q_{ins}, ILES (d) Q_{ins}, LDKM

(e) Q_{ins}, Tip zoomed, ILES

Figure 4.8: Instantaneous and averaged distributions of Q=5000 around the foil, ILES and LDKM, P2S2 resolution, AOA=9 deg

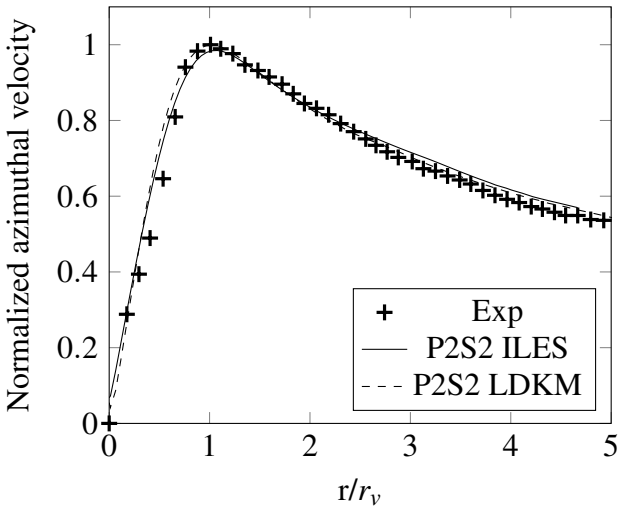

Figure 4.9: Variation of the normalized azimuthal velocity at the vortex core region, the velocity is normalized by $u_\theta = 6.7m/s$, $z/C = 1.14$

quite well. The lift force, however, is predicted slightly better by LDKM, Table 4.1.

The distribution of the turbulent kinetic energy in the vortex core region is presented in Figure 4.10. The results show that the vortex core contains the highest turbulent kinetic energy, similar to results reported by Wells [83] using RSM. As the vortex core can be assumed laminar due to small fluctuations, this high

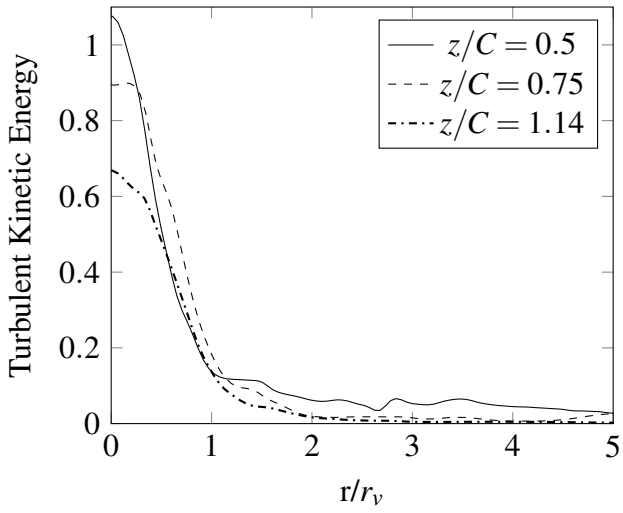

Figure 4.10: Variation of the sub grid turbulent kinetic energy at the vortex core region. P2S2, LDKM.

Table 4.1: Lift coefficient, AOA=9°, $Exp.C_l = 0.67$, wetted flow, ILES vs. LDKM

Turbulence Model	Mesh Resolution	Numerical C_l	Comparative Error (%)
ILES	P2S2	0.688	2.7
LDKM	P2S2	0.676	0.8

turbulent kinetic energy is believed to be related to the vortex wandering and the variation of vortex core location.

4.3 THE SST $k-\omega$ MODEL WITH CURVATURE CORRECTION

This section evaluates the adoption of curvature correction models in the SST $k-\omega$ model, and its effects on the tip vortex flow simulations.

4.3.1 C_μ sensitization (CC1, CC2, and CC3)

In Figure 4.11, distribution of f_C, ν_t and production term of the k transport equation in the streamwise direction are presented. The figure also includes the isosurface of the pressure, $p = p_{sat}$. As it can be observed, CC3a can predict a more accurate tip vortex compared to the other ones. The relation between the predicted tip vortex, ν_t, and k production term should be also noted. Higher production term, which corresponds to higher ν_t, prevents the tip vortex from development. In CC1, the production term of k is much higher than the other models leading to much higher ν_t in CC1. Consequently, the predicted tip vortex by this model is weaker than the others.

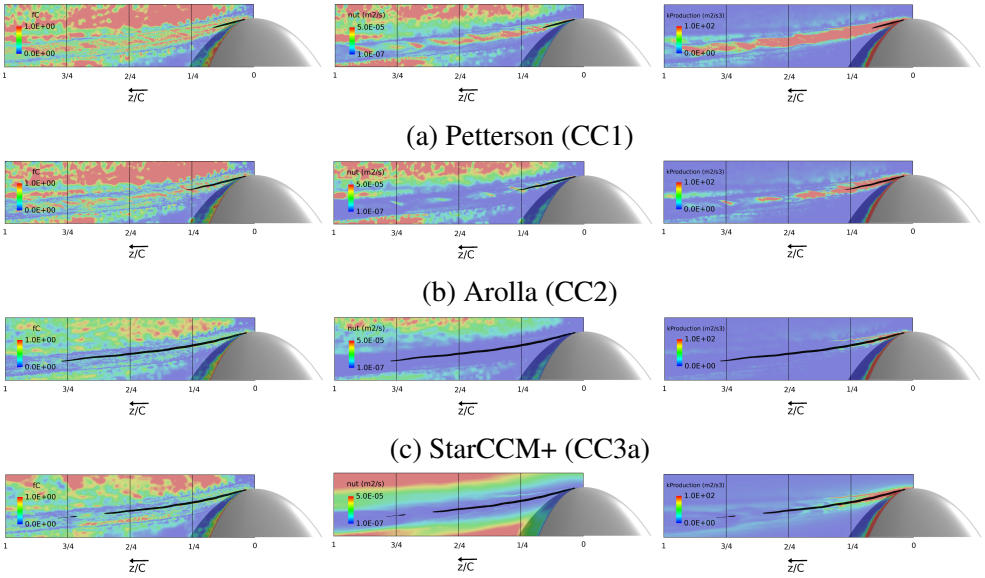

(a) Petterson (CC1)

(b) Arolla (CC2)

(c) StarCCM+ (CC3a)

(d) StarCCM+ (CC3b)

Figure 4.11: Distribution of correction function, f_C, turbulent viscosity, k eqaution production term, and pressure iso-surface ($p = p_{sat}$) for CC1, CC2, CC3a, and CC3b

The only difference between CC2 and CC3a is the upper clipping of f_C. It is noticeable that this difference leads to such a considerable difference on the tip vortex prediction. This, however, poses an uncertainty and question about the calibration of these curvature corrections, and the possibility of their adoptions in different applications.

Comparison of CC3a and CC3b shows that both of the models provide accurate predictions of the tip vortex, where the tip vortex predicted by CC3a is a slightly stronger. The CC3b predicts higher values for f_C especially in the region $z/C \sim 0.5$ outside the vortex core, possibly the reason for weaker vortex prediction by CC3b. The CC3b also predicts higher k production close to the tip of the foil ($z/C < 0.25$).

4.3.2 Modification of ω transport equation (CC4, and CC5)

It is observed that both the CC4 and CC5 models distinguish the rotating region and the vortex cortex core quite well. However, one feature of the η_3 based (CC4) model is its behaviour at $z/C > 0.25$, Figure 4.12. The distribution of F_{rc} shows that the model predicts a very high value (close to the clipping value of 10) for F_{rc} outside the vortex core. This leads to a very high dissipation in the region and therefore compensates the over prediction of k at the outside of the vortex core. It should be noted that the distribution of F_{rc} seems to have a stronger dependency on the flow structures, resulting in a more non-uniform distribution of F_{rc} around the vortex core. Another consequence is the stronger dependency on the mesh

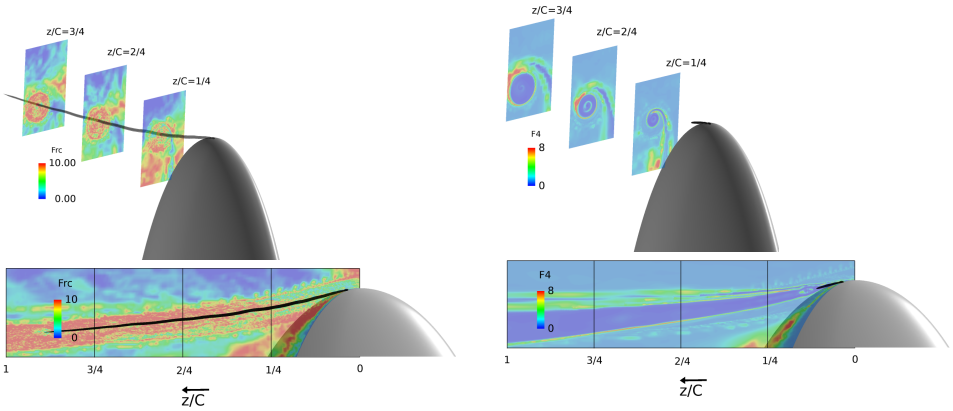

(a) η_3 based (CC4) (b) Bradshaw (CC5)

Figure 4.12: Distribution of curvature correction functions for CC4, and CC5 at different sections downstream of the foil

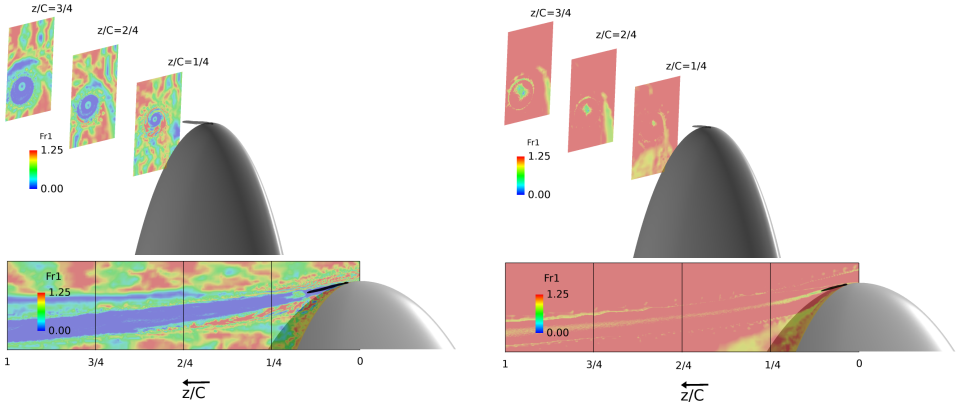

(a) Menter (CC6) (b) Stabnikov (CC7)

Figure 4.13: Distribution of curvature correction functions for CC6, and CC7 at different sections downstream of the foil

resolution, as the flow structure prediction depends on the mesh resolution.

4.3.3 Modification of production terms (CC6, and CC7)

In Figure 4.13, the curvature correction function distributions for CC6 and CC7 are presented where it is found that both of the models fail in predicting the tip vortex accurately. The CC7 is clearly incapable of predicting the rotating region. It predicts $f_{r1} > 1$ in the rotating region and especially outside the tip core. As the function is a multiplier of the k production term, it leads to higher turbulent kinetic energy and consequently leads to higher turbulent viscosity. It is observed that not having an upper clip in CC7 contributes to this incapability.

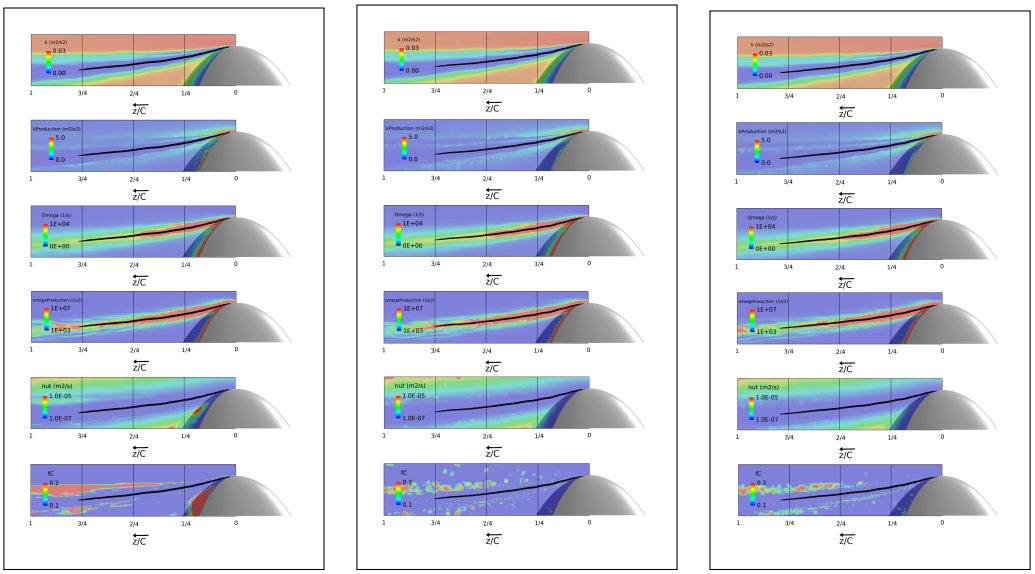

(a) η_1 (b) η_2 (c) η_3

Figure 4.14: Comparison of different sensitization models

4.3.4 C_μ sensitization based on η parameters (CC8)

Figure 4.14 represents the turbulent properties and also the iso-surface of pressure ($p = p_{sat}$). The extent of the tip vortex iso-surface is very similar in these three approaches. While the distribution of ω in the vortex region is very high, the predicted k values are much lower than the predicted values by the original SST model. Having very low value of k and at the same time very high value of ω in the vortex region leads to very low values of ν_t. The low prediction of ν_t in the tip region resembles laminar conditions, and explains the similarity of predicted tip vortex extension with laminar simulations.

It should be noted that adoption of C_μ sensitization has two main contributions. The sensitization leads to lower prediction of the turbulent viscosity in the region with high values of η_1, η_2, or η_3. The other contribution is in the k transport equation. As the production term of this equation is proportional to the ν_t magnitude, lowering ν_t would lead to lower production of k. As a results, k becomes smaller, which thus leads to extra reduction of ν_t.

4.3.5 Tip vortex velocity field

The axial and inplane velocity distributions at $z/C = 0.5$ section downstream of the foil are presented and compared with the experimental measurements in Figure 4.15. The axial velocity is normalized by inlet velocity value ($6.8m/s$), and the inplane or cross flow velocity field is normalized by $6.7m/s$ value according to the reported experimental data. The measurements indicate that the tip vortex

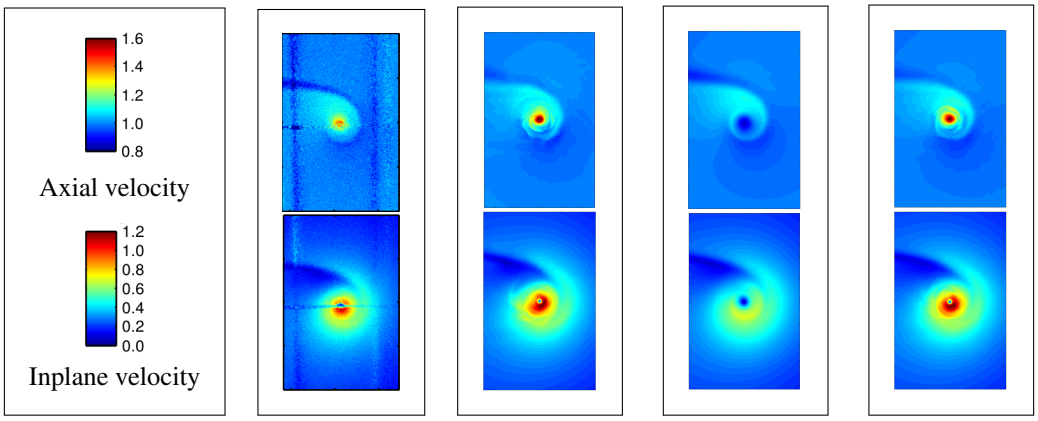

(a) Color map (b) Exp (c) ILES (d) SST (e) CC8(η_3)

Figure 4.15: Comparison between experimental measurements [81] and numerical predictions of tip vortex velocity field at section $z/C = 0.5$, P1S1 resolution

core has accelerated axial velocity, up to 1.6 times larger than the inlet velocity. As the SST $k-\omega$ model fails in prediction of the tip vortex, it cannot predict this accelerated velocity field, and instead predicts very low values for the vortex core axial velocity. Both ILES and CC8(η_3) are able to accurately predict the accelerated axial velocity, even though the predicted value seems to be slightly higher than the measurements. Similar trend is also observed for the inplane velocity distribution where ILES and CC8(η_3) provide more accurate results.

4.3.6 Analysis of the accelerated axial velocity

In Figure 4.16, the flow streamlines are presented for the SST $k-\omega$ and CC8(η_3) models. The streamlines on the foil are plotted for the pressure and suction sides of the foil, using white lines. The figure also includes the normalized axial velocity at section $z/C = 0.5$. As the vortex core is accelerated, the seeding points of the streamlines are placed at the vortex core of this section in order to track the streamlines that are fed into the accelerated flow region, with black lines.

The SST model does not predict any separation of the boundary layer (BL) on the pressure side until the trailing edge, and the predicted suction side separation line is located at $z/C > 0.9$. Adoption of the curvature correction CC8(η_3) not only affects the tip vortex region, but also alters the BL behaviour on the foil where the suction side BL separation is predicted to happen at $z/C \sim 0.6$, similar to experimental observations [21], and the pressure side BL separation is located at $z/C \sim 0.8$.

The black streamlines represents the flow passing through the accelerated tip vortex core at the section $z/C = 0.5$. As it can be observed, the adoption of curvature correction predicts stronger vortex, and therefore lower pressure at the vortex

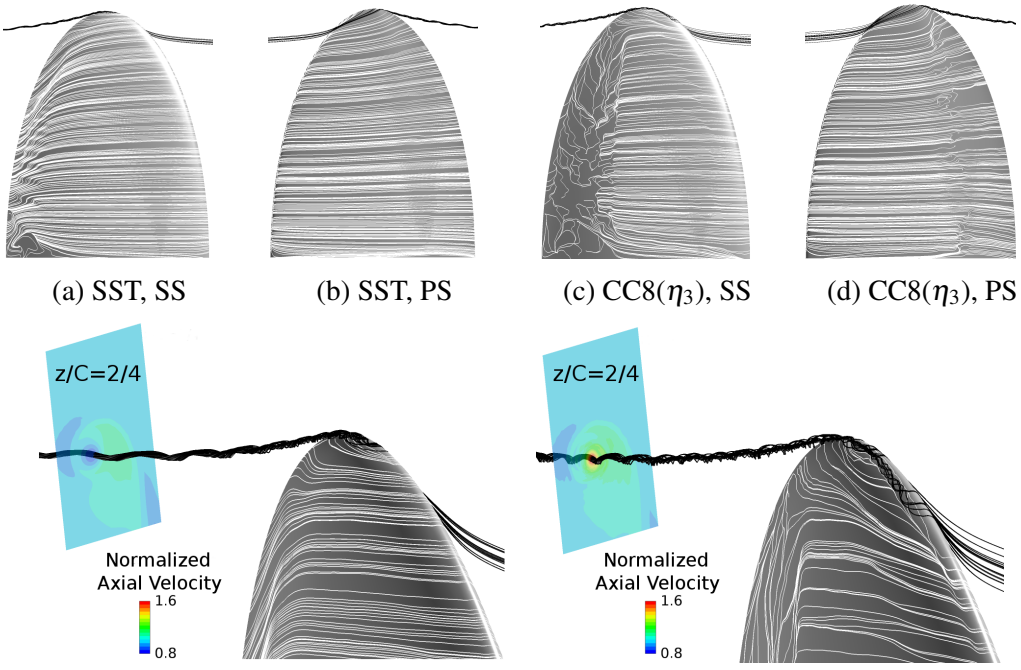

(a) SST, SS (b) SST, PS (c) CC8(η_3), SS (d) CC8(η_3), PS

(e) SST, tip zoomed view (f) CC8(η_3), tip zoomed view

Figure 4.16: Comparison between flow streamlines passing through the vortex core predicted by the SST $k-\omega$ model and CC8(η_3) model, SS: Suction Side, PS: Pressure Side

core leading to more flow suction into the vortex core.

4.4 Summary of the elliptical foil analysis

The mesh dependency study clarifies that at least 16 grid points across the vortex core radius are required to accurately predict the tip vortex with the current numerics. The streamwise grid point demand is found to be lower, with cell size equal to 8 grid points across the vortex core radius, as the streamwise gradients of the flow are lower compared to the inplane flow gradients. As the OpenFOAM package can be reasonably considered as a second order numerical tool, these findings are found to match with previous reports on LES analysis of tip vortex flows.

Comparisons of the velocity distributions between numerical results and experimental PIV images show very good agreement. It highlights the capability of the LES approach in predicting the accelerated axial velocity at the vortex core, and therefore good prediction of the pressure distribution which is very important in cavitation inception studies.

The comparison of ILES and LDKM results clarifies that both of these LES models can provide very accurate tip vortex flow predictions. The predicted velocity distributions at different sections downstream of the foil, and pressure dis-

tribution and axial velocity along the tip vortex trajectory are compared and found to be very similar.

The LDKM results also predict very high turbulent kinetic energy at the vortex core. Even though the high value of turbulent kinetic energy in the vortex core has been reported also by experimental measurements, it is believed that this high turbulent kinetic energy is related to the vortex wandering combined with small-scale flow structures surrounding the vortex core, rather than turbulent fluctuations in the actual core.

RANS studies of tip vortex flows are presented by evaluating different curvature correction (CC) methods incorporated into the SST $k-\omega$ turbulence model. The investigation includes two types of curvature correction approaches, i.e. sensitization of the C_μ and modification of the transport equation production or destruction terms.

The results of the curvature correction study indicate the possible improvement of the SST $k-\omega$ model in predicting the tip vortex flows by employing CC models. Some of the evaluated CC models, however, were either incapable of preventing excessive turbulent viscosity prediction in the viscous core region or were sensitive to the clipping parameters, and their initial calibration parameters. Best results where obtained using the CC8 models, which sensitize C_μ. These models predict accurate tip vortex flow fields and formation of a leading edge vortex partly due to that they alter the boundary layer behaviour on the foil, . This is consistent with the flow behaviour predicted by ILES, and is believed to be crucial for the correct behaviour with an accelerated axial flow in the vortex core.

The numerical results presented in this chapter clearly show the capability of the numerical approach in predicting tip vortex flows. Excellent agreement is found between the numerical predictions and the experimental measurements of the velocity field at different sections downstream of the foil, also implying an accurate prediction of the pressure field.

5

Sheet Cavitation

5.1 TWISTED DELFT HYDROFOIL

In this section numerical results of cavitating flow around the Twisted foil are presented in order to evaluate the proposed mass transfer modelling modifications, and also investigate the mesh resolution requirements for sheet/cloud cavitation simulations. The foil, studied experimentally by Foeth et al. [68, 69] and later by Peng et al. [84], generates cavitation which resembles propeller cavitation but in a well defined and easily studied set up; this makes it an attractive test case for evaluation of computational approaches for predicting cavitation in the hydro machinery. Moreover, this case was presented as a benchmark case in several workshops on cavitation, thus several numerical studies have been performed on the foil [85, 86, 67, 87, 88, 89, 90].

Based on the wet flow mesh dependency study, the mesh T11-VIII having $y^+ = 1$ is selected as the base resolution. For this mesh resolution, cavitation is simulated in three different states. These three states are presented in Table 5.1 as model A, B, and C. Model A is based on the original settings of the Schnerr-Sauer model. In the model B, the phase change model coefficients are modified according to the proposed modification from the turbulent time scale while the pressure threshold is keep constant equal to the saturation pressure. In model C, the threshold pressure is also modified to consider the shear stress in the liquid pocket rupturing and cavitation formation.

5.1.1 Verification of the proposed model for phase change rate

In Figure 5.1, the average vapour volume fraction and the average pressure distributions on the foil for the three different models (A, B, and C) are presented.

As it can be observed from the averaged pressure coefficient of model A, Figure 5.1b, the minimum pressure coefficient is lower than the minus cavitation

Table 5.1: Coefficients of the three different models investigated

Model	C_v	$p_{threshold}$
A	1.0	p_{Sat}
B	modified	p_{Sat}
C	modified	$p_{Sat} + p_a$

number (-1.07) which indicates that the pressure is negative at those regions. This indicates that the cavitation (i.e. vapour liquid phase change rate) has not been modelled correctly. Moreover, based on the vapour iso-surfaces, Figure 5.1a, the content and volume of vapour in Model A is under predicted significantly. Two parameters can cause such an under prediction. The first one is the number of excited nuclei and the other is the rate of the mass transfer. Since these two parameters have similar contributions according to the Sauer mass transfer model, here we have put the focus on the mass transfer rate. To adjust the value of the mass transfer rate, one approach is to manually increase the C_v coefficient in order to increase the cavitation production, until a point where the negative pressure disappears.

The proposed modification for the coefficients will create a better relation between phase change rate and local flow properties. It can be observed from the obtained results, Figure 5.1, that using the modification leads to having positive pressure throughout the computational domain, and therefore more precise prediction of cavitation (e.g. size and shedding behaviour).

In Figure 5.2, the added pressure to the pressure threshold based on the shear stress modification is presented, Model C. As expected, the results show that this modification is effective in the region where velocity strain is high, e.g. leading edge and cavity closure regions. For the studied case, the maximum added pressure to the saturation pressure is around 1000 Pa. It should be highlighted that this modification will lead to an increase in cavitation production at the leading edge as well as in condensation rate due to have higher threshold pressure at the downstream region and cavity closure region.

5.1.2 Spatial mesh resolution effects on cavitation simulation

When cavitation occurs in a flow, due to the different vapour and liquid density values, the mass fluxes at the interface of the cavity will become different. This can also be deduced from the non-zero divergence of the velocity in the cavitating flow since at the interface of the cavity, due to having phase change and varying density over time, the summation of mass fluxes on the faces of the computational cells are not zero. Therefore, capturing the cavity interface, and cavity behaviour, will be dependent on the spatial resolution, especially where the cavity interface exists. The presence of the cavity and its shedding also alters the flow dynamics, and can lead to more vortical structures which changes the mesh resolution

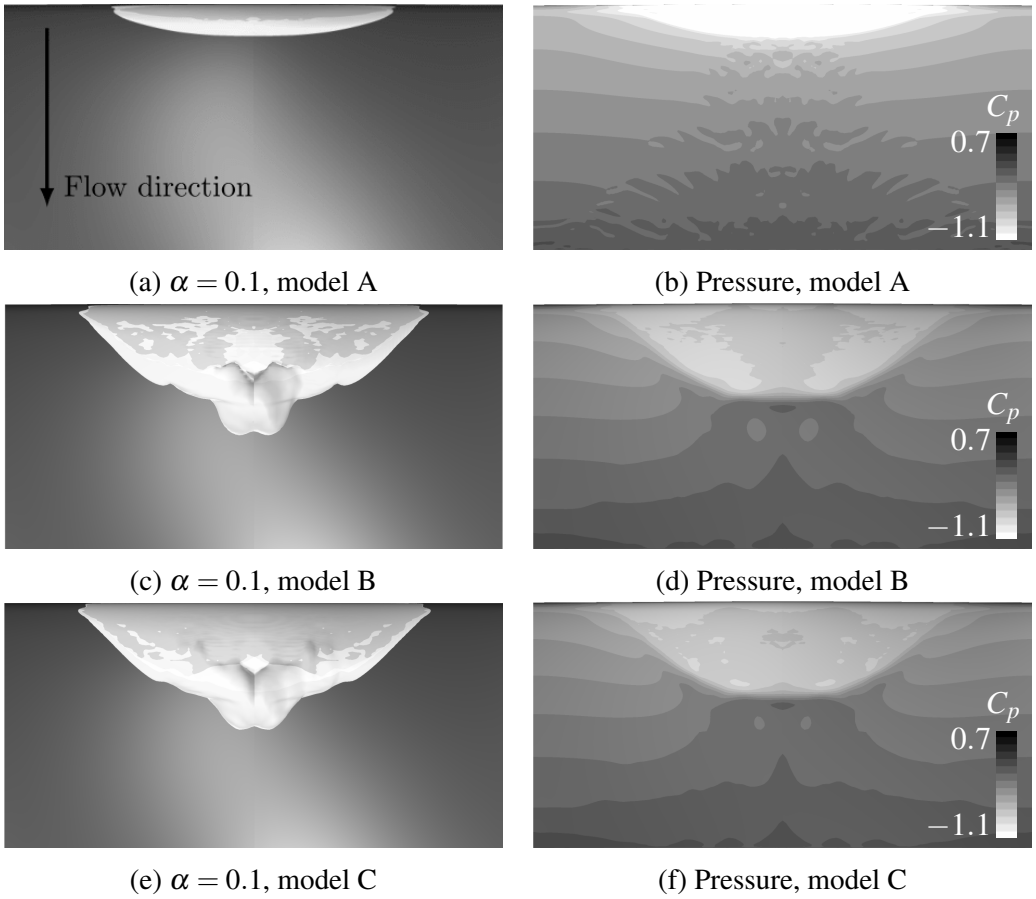

(a) $\alpha = 0.1$, model A (b) Pressure, model A

(c) $\alpha = 0.1$, model B (d) Pressure, model B

(e) $\alpha = 0.1$, model C (f) Pressure, model C

Figure 5.1: Averaged vapour iso-surfaces and pressure distribution around Twist11 with $y^+ = 1$.

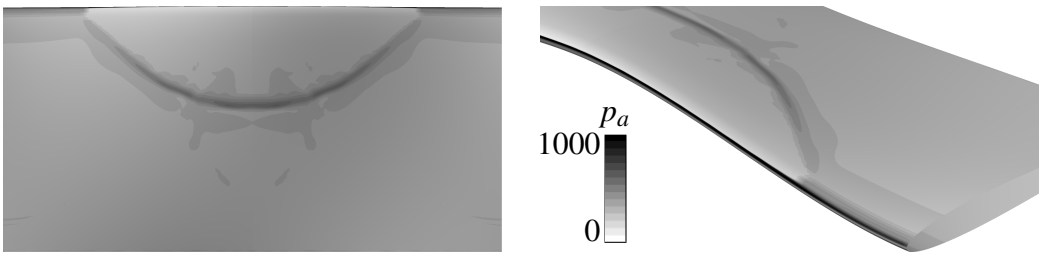

Figure 5.2: Added Pressure to the threshold pressure due to the viscous effects for cavitation around Twist11.

requirements.

In Figure 5.3, the predicted average pressure at two different sections of the foil is compared with the experimental data. Both the experimental data measured at EPFL and Delft laboratories are considered for the comparison.

The numerical results for all of the spatial resolutions have similar level of accuracy in the region near to the leading edge, $X < 0.4$. However, mesh T11-B

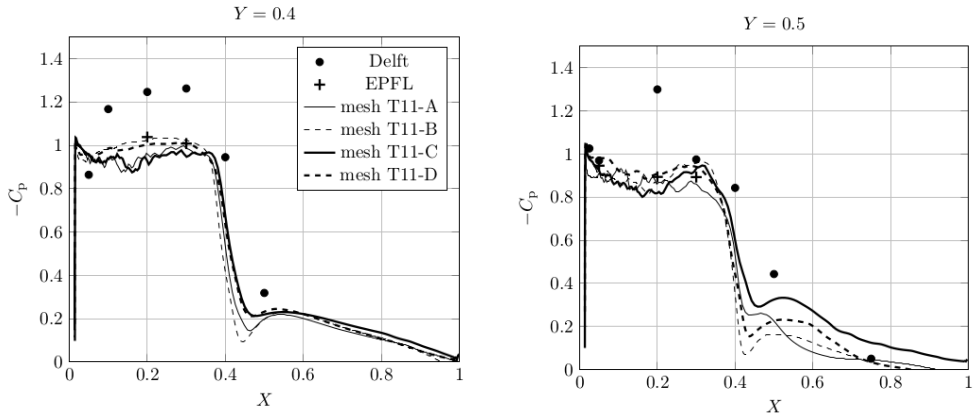

Figure 5.3: Pressure coefficient distributions over the Delft Twist11 for different mesh resolution, at different sections of the foil.

and mesh T11-D, which have the same surface resolution, show better prediction in the region close to X = 0.2. The results also show that increasing the spatial resolution in the wall normal direction will increase the accuracy in predicting the pressure distribution, especially at the region $0.4 < X < 0.6$. Although mesh T11-C shows better prediction of the pressure at $0.4 < X < 0.6$, it over predicts the pressure at the trailing edge region.

The comparison between the averaged numerical results and experimental data of the lift coefficient is presented in Table 5.2. As it can be seen from this table, although all of the selected resolutions were able to predict the lift coefficient very well in the wet flow simulations, the error level in the cavitating simulations is around 11%.

Table 5.2: Lift coefficient for various mesh resolutions in cavitating flow simulation.

Mesh	C_l	Error %
T11-A	0.441	-13.5
T11-B	0.444	-12.8
T11-C	0.454	-10.9
T11-D	0.449	-11.9
Exp. [68]	0.51	-

There are several factors affecting the lift force prediction in the cavitating flow around the foil. The lift force consists mainly of the pressure force. It is the pressure value that also defines the cavity content and size. Pressure, velocity and volume fraction are linked to each other through the non-linear governing equations. Considering the pressure distribution, it may be deduced that over prediction of the pressure at the down stream region of the cavity, $0.4 < X < 0.6$,

can be a reason for under prediction of lift force.

In Figure 5.4, variation of the lift coefficient in one typical shedding cycle is presented for each mesh resolution. There is one significant difference between the lift coefficients predicted by different meshes. Mesh T11-A and mesh T11-C, which have the same surface mesh resolution, predicts strong force acting on the foil during the cavity collapse at the down stream. This strong force, which is due to a strong pressure pulse, has caused the negative lift at the collapse time while the two other mesh resolutions show positive lift prediction throughout the shedding cycle.

The uncertainty analysis of the results is conducted according to [91, 92, 93], and is included in paper B.

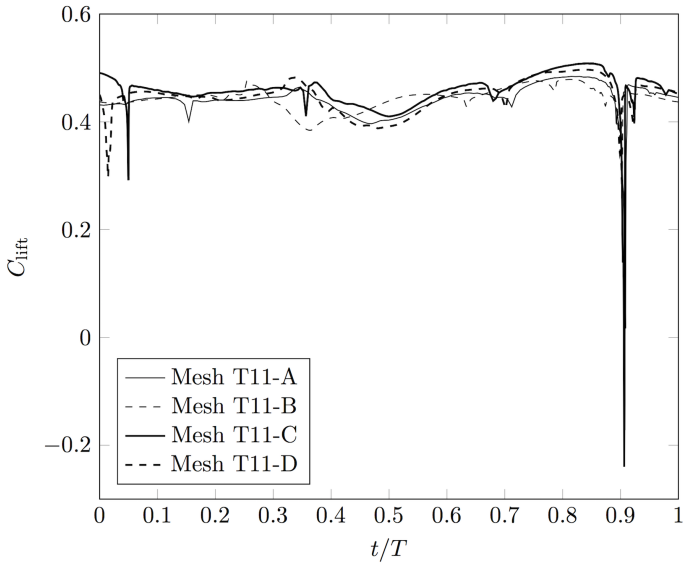

Figure 5.4: Variation of lift coefficient for various mesh resolutions in the cavitating flow conditions for one typical shedding cycle.

5.1.3 Cavitation shedding behaviour

Integrating the vapour volume fraction, Figure 5.5, shows that the cavity size is directly dependent on the mesh resolution where the finest mesh resolution, mesh T11-D, shows a bigger cavity size than the other resolutions. To some extent, this behaviour was predictable since the cavity amount is directly proportional to the pressure distribution, which for vortex based flow is dependent on the spatial resolution. Based on the vapour volume fraction variations over time, the frequency of the shedding is calculated and presented in Table 5.3. It is noticeable from this table that increasing the resolution, and therefore better prediction of the cavity amount, will increase the accuracy of the cavitation transportation, i.e. frequency of the flow.

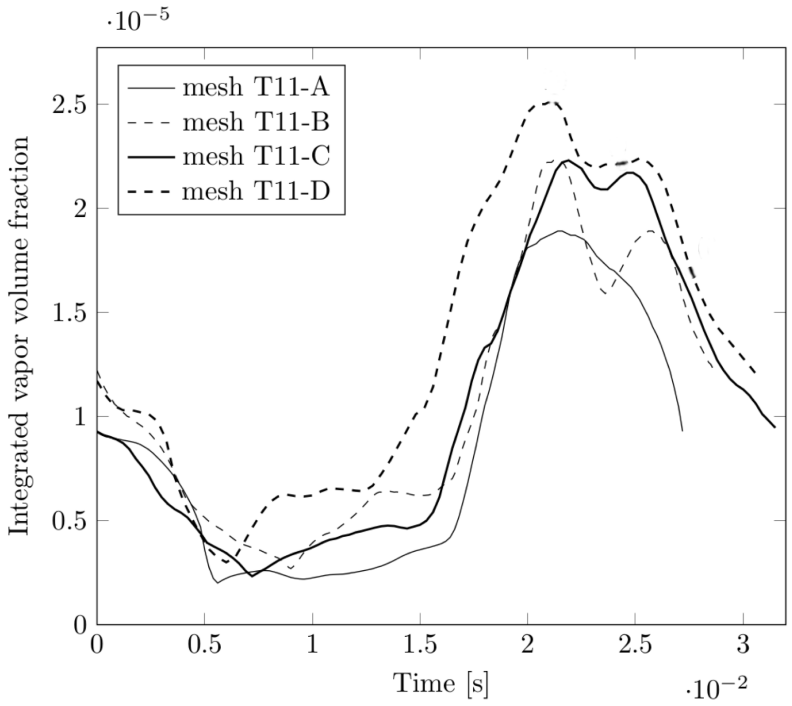

Figure 5.5: Integrated vapor volume for different mesh resolutions in one typical shedding cycle.

Table 5.3: Comparison of the shedding frequency of the cavitating flows.

Mesh	$f_{\mathrm{FO}}Hz$	Error %
I	36.7	12.7
II	34.8	7
III	31.7	-2.6
IV	32.5	-0.1
Exp. [68]	32.55	-

5.1.4 Cavitation pattern

In Figure 5.6, the time averaged vapour iso surface 10 % is presented for different resolutions. The main difference is near the middle of the foil where the cavitation and the separated vortex have stronger coupling and interaction. Since the finer mesh can predict the vortex strength better than the others, the cavitation content near the middle plan is bigger for the finer mesh.

In Figure 5.7, the numerical results of cavitation shedding behaviour are presented and compared with the experimental data in one typical shedding cycle. The pictures are related to the coarsest resolution, mesh T11-A, and the finest resolution, mesh T11-D. It should be noted that since the frequency of the flow predicted in the mesh T11-A is higher than the experimental data, the time differ-

ence between each step is adjusted to find the relative cavity pictures. As it can be seen from Figure 5.7, the coarse mesh fails in predicting and transporting the separated two-phase vortex, e.g. Figure 5.7a, while the finer mesh can preserve the vortex until the trailing edge of the foil.

For the finest resolution, the amount of the separated cavity is in reasonably good agreement with the experimental data. It indicates that the spatial resolution at the leading edge region ($X < 0.4$) is good enough to capture the 3D sheet cavity generation and separation, Figure 5.7d. Moreover, it shows that the pressure distribution and liquid to vapour phase change have been modelled appropriately. There is, however, a small difference between numerical results and experimental data regarding the cavity width.

During the transportation to the downstream, due to over prediction of pressure, which itself can be a result of lack of spatial resolution, the cavity shrinks in the simulation much faster than in the experiments. When the separated cavity reaches the trailing edge region of the foil, the discrepancy between the numerical results and experimental data becomes more obvious, Figure 5.7j. This indicates that the rate of phase change from vapour to liquid is over predicted in the down stream region. The accuracy of condensation prediction depends on several factors such as condensation phase change model (modelling perspective), and computational time and spatial resolution (numerical perspective). The condensation model used in this study is based on the dynamic of a single bubble during the bubble growth which does not include effects of compressibility and strong bubble collapse jet. As it is stated before, the mesh resolution affects the pressure distribution prediction accuracy. Lack of enough spatial mesh resolution will lead to over prediction of vortex core pressure which means higher condensation rate for the separated cavity.

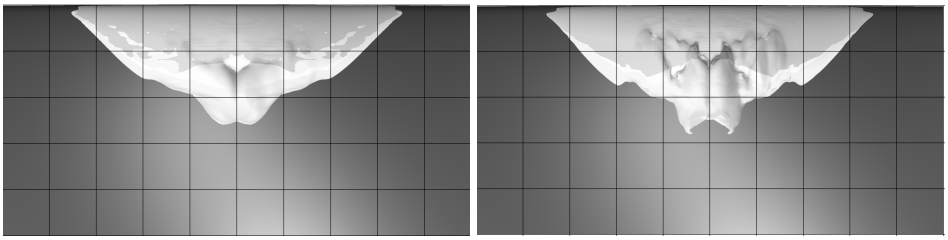

(a) $\alpha_v = 0.1$, mesh T11-A (b) $\alpha_v = 0.1$, mesh T11-B

(c) $\alpha_v = 0.1$, mesh T11-C (d) $\alpha_v = 0.1$, mesh T11-D

Figure 5.6: Averaged vapor iso-surfaces 10%.

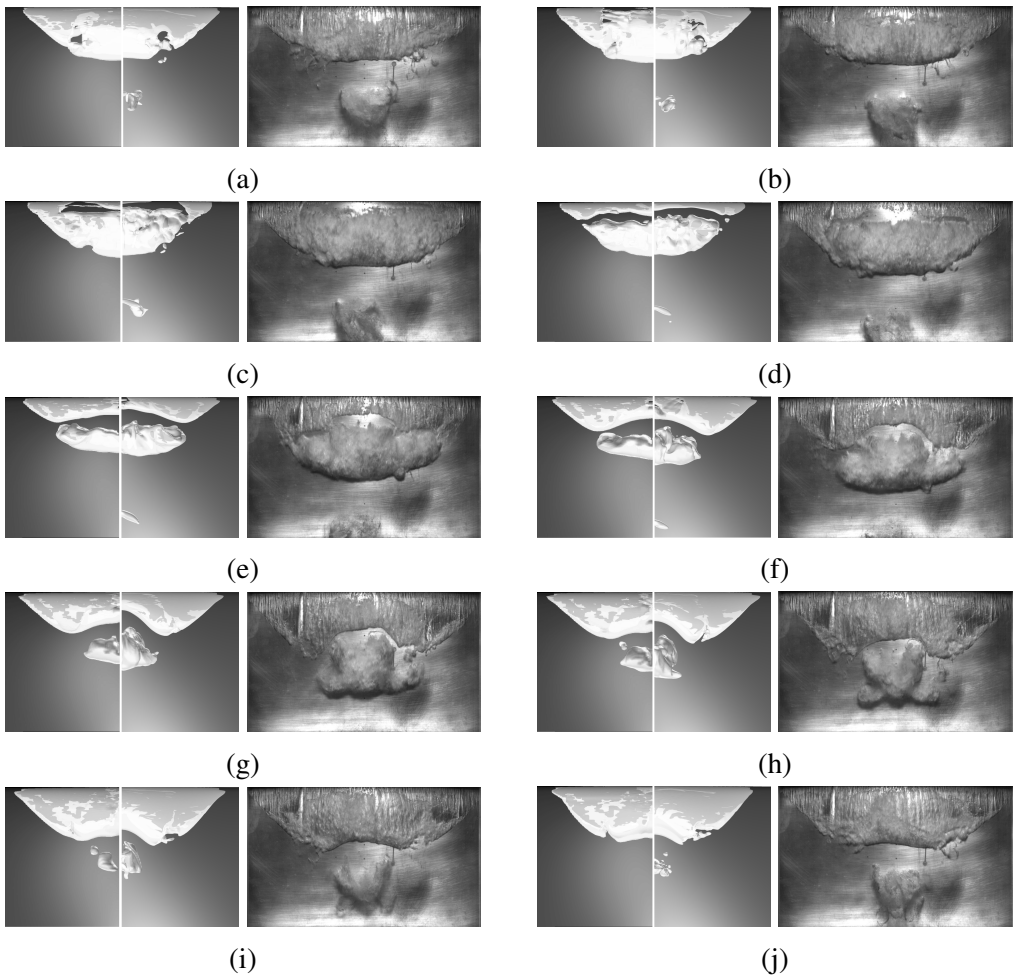

Figure 5.7: Comparison between numerical results (first column, left half of the foil: mesh T11-A, right half: mesh T11-D) and experimental snapshots regarding cavitation shedding development, time step $=1/10T$, vapor iso-surface 10%.

5.1.5 Cavitation-vortex interaction

In Figure 5.8, the average distribution of vapor volume fraction, Q-criterion, vorticity, vortex stretching term, vortex dilatation term, and baroclinic term are presented. As the vorticity is a three dimensional vector, here in order to simplify the comparison, the magnitude of the terms are plotted. The plots are related to the mid-section of the foil, Y=0.5.

Figure 5.8a and Figure 5.8b show that in T11-D, the extent of the predicted cavitation is larger. It is also clear that the cavity is transported to the trailing edge of the foil which matches better with the experimental observations. It also indicates more vortical cavitation prediction comparing to T11-A.

In Figure 5.8c and Figure 5.8d, the absolute value of Q is presented. In both of the meshes, the value of Q on the interface of the cavity, and at the cavity closure

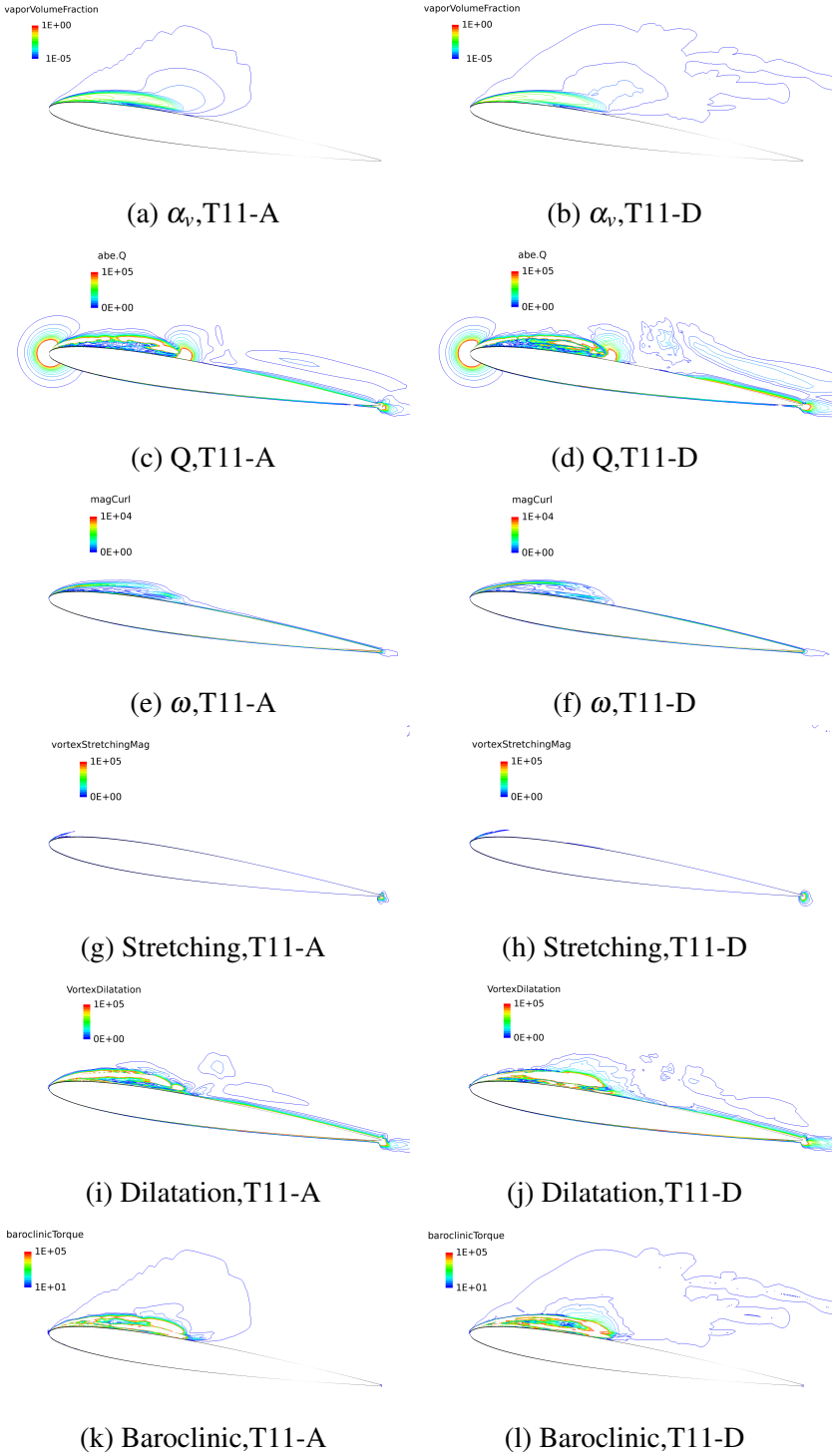

(a) α_v,T11-A (b) α_v,T11-D

(c) Q,T11-A (d) Q,T11-D

(e) ω,T11-A (f) ω,T11-D

(g) Stretching,T11-A (h) Stretching,T11-D

(i) Dilatation,T11-A (j) Dilatation,T11-D

(k) Baroclinic,T11-A (l) Baroclinic,T11-D

Figure 5.8: Average distribution of vapor volume fraction, absolute value of Q, magnitude of: vorticity, vortex dilatation, vortex stretching, baroclinic torque for mesh T11-A and T11-D at Y=0.5.

region is larger than in the other regions. The comparison of Q also shows that the cavity is filled with vortex structures. Moreover, it shows that T11-D predicts more unsteady structures after the cavity closure which corresponds to the vapor transportation to the trailing edge.

Comparison of the vorticity magnitude, Figure 5.8e and Figure 5.8f, clarifies that the region with the highest vorticity magnitude matches with the cavity interface location, and it is larger and also sharper in T11-D. It corresponds to the vorticity stretching characteristics presented in Figure 5.8g and Figure 5.8h.

In Figure 5.8i and Figure 5.8j, distributions of vorticity dilatation are presented. Vorticity dilatation is related to the vorticity and the divergence of the velocity, and therefore it is noticeable at regions where the vorticity magnitude is high and the mass transfer between phases occurs. From these figures, it can be observed that for T11-D, the phase change presence is continued till the trailing edge of the foil, again indicating the transport of the shed cavity cloud. This is also presented in the figures related to the baroclinic term, Figure 5.8k and Figure 5.8l. At the downstream of the foil ($X > 0.6$), and close to the surface the dilatation term is notable. At this region even though that the mass transfer rate (or divergence of the velocity) is very small, the vorticity is very high due to the presence of the boundary layer.

The maximum of vortex stretching, dilatation, and baroclinic terms appears on the interface of the cavity, Figure 5.8. It can be deduced that it is the interface of the cavity that is mostly involved in the vorticity transportation of the cavitating flows.

5.1.6 Summary of the Delft twisted flow simulations

Numerical simulations of unsteady cavitating flow around the Delft Twist11 foil are conducted on four different spatial resolutions to investigate effects of the spatial mesh resolution on the separated vortex development and its impact in the separated cavity. Moreover, two improvements to transport equation based mass transfer models are proposed, and evaluated.

The first modification employs the velocity strain rate time scale to improve the coupling between the local flow properties and mass transfer modelling, leading to better prediction of cavitation behaviour. This local strain rate based adjustment is the main factor behind the improvement in the presented results.

The concept of using saturation pressure as the pressure threshold for phase change in the flowing fluid is also investigated, and effects of considering the viscous stress tensor in the calculation of pressure threshold is studied. It is shown that this modification will increase vapor generation, but also affect condensation behaviour.

The results indicate the dependency of the cavity transportation and also cavity collapse location prediction to the spatial mesh resolution. Since the collapse is dependent on the resolution, the collapse induced pressure pulses are also dependent on the resolution. The collapse occurs in a very small fraction of time,

and therefore this pressure oscillation may not affect the average force prediction but the erosion and noise prediction will be affected. One suggestion is using very fine resolution in the closure regions and also in the region where shed cavity transportation occurs.

5.2 E779A PROPELLER

INSEAN E779A model propeller is a modified Wageningen propeller characterized by a constant pitch distribution and very low skew, tested at the Italian Ship Model Basin, INSEAN [74, 75, 76]. Numerical simulation of cavitating flows around E779A propeller is conducted, and presented in this section in order to evaluate the accuracy of propeller simulations in open water setup. In the selected operating condition, the rate of revolution and the inlet velocity are set equal to $n = 36$ rps and $U = 5.808\ m/s$. The outlet pressure was adjusted to $\sigma_n = 1.76$.

The comparison of cavitation extent between numerical results and experimental data is presented in Figure 5.9. Three types of cavitation patterns are observed in the experiment, sheet cavitation on the blade, tip vortex cavitation and hub vortex cavitation. The sheet cavitation is separated from the blade by a vortex and creates tip vortex cavitation which lasts for a few revolutions. The numerical results predicts these two cavitation patterns reasonably well. It should be noted that finer resolution is needed to capture the physics of a vortex and also to preserve them during transport to the downstream of the flow. Since the focus of this study is on the validation of the mass transfer modelling, and prediction of sheet cavitation on the E779A propeller, the analysis of cavitating tip vortex, and its numerical requirements are conducted, and are later presented for Rolls-Royce propellers C and D.

Effects of different mass transfer models (e.g. Kunz, Zwart, and Full Cavitation Model) and their coefficients adjustments on the cavitation extent of E779A have been investigated and reported in the literature, see [94]. In Figure 5.10, the results of modified Schnerr-Sauer model from the current work are compared with the results of other calibrated mass transfer models, [94]. As it is described, the advantage of using modified coefficients according to the strain rate is that there is no need to calibrate the model coefficients, and the model would be automatically calibrated based on the local flow conditions.

A glimpse conclusion from Figure 5.10 is that all of the models over-predict the cavity size. This behaviour, which also has been observed in most computations using a variety of simulation techniques and models, [94, 72, 95], could be due to laminar flow on the blade, geometrical modelling problems, or similar effects.

The open water performance of the propeller in the cavitating condition, thrust and torque coefficients, are presented in Table 5.4. Comparison with the experimental data shows that the performance is correctly captured although slightly under predicted but consistent with the over predicted cavity extent.

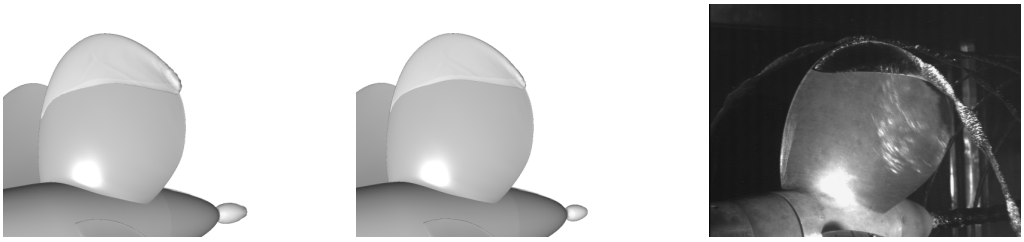

(a) $\alpha_v = 0.9$ (b) $\alpha_v = 0.5$ (c) Experiment

Figure 5.9: Numerical results comparison with experiment, E779A propeller.

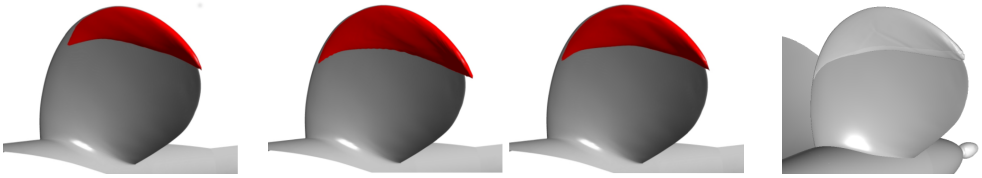

(a) (b) (c) (d)

Figure 5.10: Comparison of different calibrated cavitation mass transfer models results for E779A propeller [94], iso-surface $\alpha_v = 0.5$, a=Full cavitation model, b=Kunz model, c=Zwart model, d= current results.

5.3 PPTC PROPELLER, SMP 2015

In this section, numerical simulations of a model scale five bladed propeller known as Potsdam Propeller Test Case (PPTC), used as the reference geometry of the 2nd International Workshop on Cavitating Propeller Performance (2015), are presented. As the propeller experiences different cavitation regimes, it is used in the workshop as a benchmark to evaluate and compare different CFD tools. The numerical simulations of cavitation around this propeller is conducted in order to evaluate the capability of the current numerical methodology in predicting the cavitation patterns around high skewed propellers in inclined shaft setup.

5.3.1 Performance prediction

In Table 5.5, the numerical results for open water performance of PPTC propeller in non-cavitating conditions are presented and compared with available experimental data. The forces and moments here are computed for the blades only, in order to match with the experimental measurements setup.

The comparison indicates good agreement between the numerical results and experimental data. The influence of the inlet distance (SMP-Mesh-I and SMP-Mesh-II) on the wetted flow performance of the propeller is also investigated. Since the values presented here is the time-averaged value which do not represent the temporary small size oscillations, the effects of the inlet distance on the wetted

Table 5.4: Cavitating flow open water performance of E779A propeller

J		K_T	$10K_Q$
0.71	Exp	0.255	0.46
	LES	0.253	0.44
	Error (%)	-0.8	-4.3

Table 5.5: Open water coefficients of PPTC propeller in wetted flow conditions

Operating conditions	Mesh	Time scheme		K_T	$10K_Q$
Case 2.1			Exp	0.397	1.02
	SMP-Mesh-I	backward	ILES	0.405	1.01
	SMP-Mesh-II	backward	ILES	0.404	1.00
	SMP-Mesh-III	backward	ILES	0.406	1.01

flow performance is so small and below the simulation error level.

In Table 5.6, the thrust and torque coefficients for cavitating conditions are presented. Comparison between numerical results and experimental data reveals that the error level of prediction is 8% for K_Q and 4% for K_T.

5.3.2 Cavitation simulation

Cavitation results for Case 2.1 having operating conditions $J = 1.019$, $n = 20rps$, $\sigma_n = 2.024$ are presented and compared with the experimental data. It should be noted that the angular positions are counted in the direction of rotation (right-handed) where zero degree is equivalent to the 12 o'clock position.

In Figure 5.11, the cavitation pattern for two iso-surfaces of vapour volume fraction (40% and 60%) are presented for suction and pressure sides of the propeller. These results are related to the SMP-Mesh-I with backward time scheme. Note that we do not see any pressure side cavitation, but the image only reveals the extended sheet of the suction side.

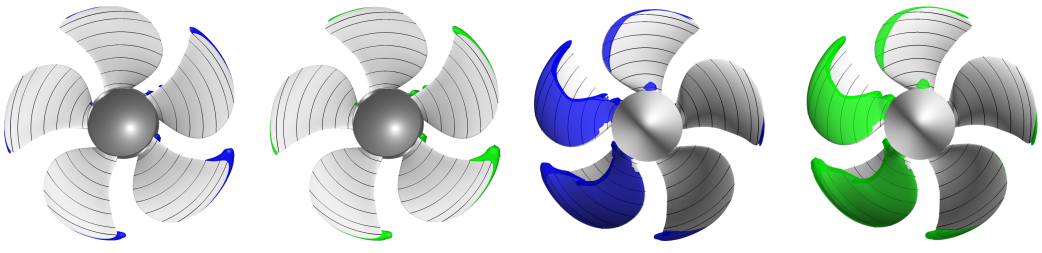

(a) PS, $\alpha_v = 0.6$ (b) PS, $\alpha_v = 0.4$ (c) SS, $\alpha_v = 0.6$ (d) SS, $\alpha_v = 0.4$

Figure 5.11: Vapor iso-surfaces for Case2.1, SMP-Mesh-I, view along x-axis, PS: pressure side, SS: suction side

Table 5.6: Open water coefficients of PPTC propeller in cavitating conditions

Operating conditions	Mesh	Time scheme		K_T	$10K_Q$
			Exp	0.36	1.02
	SMP-Mesh-I	backward	ILES	0.373	1.07
Case 2.1	SMP-Mesh-II	backward	ILES	0.374	1.05
	SMP-Mesh-III	backward	ILES	0.375	1.04

In Figure 5.12 and 5.13, the cavitation predictions are compared with the experimental sketches for Case2.1 for the suction side and pressure side at different blade positions. As it is shown in Figure 5.12, the general trend of the cavitation has been predicted reasonably well. The main difference between numerical results and the experimental data is related to the region with the bubble cavitation pattern in the experimental observation. In Figure 5.12a, the bubbly root cavitation is predicted as sheet/cloud cavitation, and in Figure 5.12b the bubbly cavitation near the leading edge is predicted as attached leading edge sheet cavitation. This sheet cavity then is attached to the near tip sheet cavity (radius 0.9) and covers almost all of the suction side of the blade. The type of bubble cavitation in the experiments indicates a blade pressure close to, or even below, the saturation pressure. The modelling used here can not accommodate the growth of individual nuclei to this type of bubble cavitation, instead leading to this formation of a sheet over the leading half of the blade. The pressure side of the blade experiences root cavitation at blade positions of zero and 270 degrees during the experiment. The numerical simulation under predicts root cavitation at zero degree position, and 270 degree blade position.

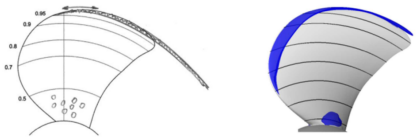

(a) Blade position zero degree

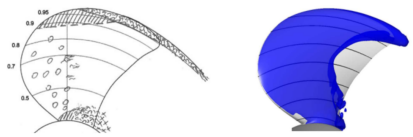

(b) Blade position 90 degree

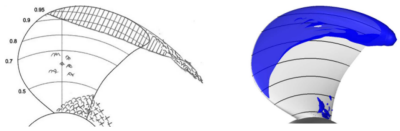

(c) Blade position 180 degree

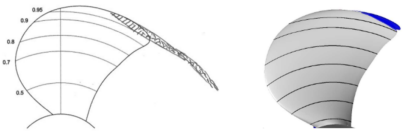

(d) Blade position 270 degree

Figure 5.12: Comparison between numerical results and experimental sketches for cavitation in Case2.1, view along x-axis, suction side, numerical results: SMP-Mesh-III, vapour iso-surface: 0.6

In Figure 5.14, the pressure coefficient of the wetted flow and the vapour iso-surface 60% are presented for Case2.1. The pressure coefficient values of the wetted flow results, Figure 5.14a, are adjusted to represent regions with pressure

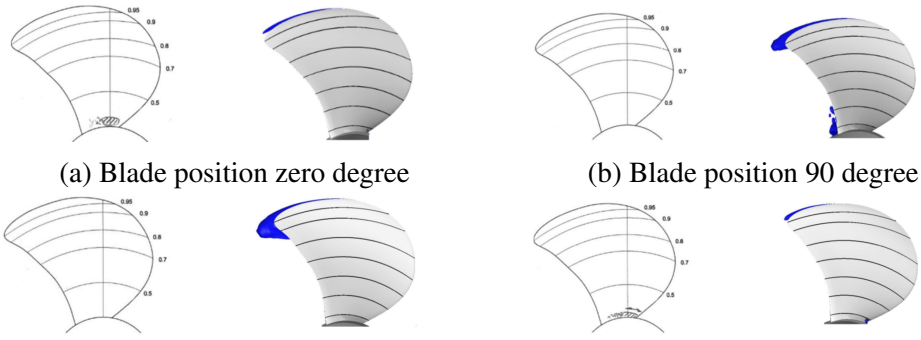

(a) Blade position zero degree

(b) Blade position 90 degree

(c) Blade position 180 degree

(d) Blade position 270 degree

Figure 5.13: Comparison between numerical results and experimental sketches for cavitation in Case2.1, view along x-axis, pressure side, numerical results: SMP-Mesh-III, vapour iso-surface: 0.6

lower than the saturation pressure. At these regions it is probable that cavitation incepts. As it is discussed before, the main discrepancy between cavitation numerical prediction and the experimental observations is related to the prediction of leading edge sheet cavity, e.g. at the blade position 72 and 144 degrees. In the leading edge regions, where the numerical prediction show pressure lower than the saturation pressure, the computational model will start to produce vapour. In the experiments, the formation of a sheet cavity depends as well on the nuclei content and nuclei residence time in the low pressure region. This is a modelling discrepancy between the numerical and experimental procedures. Bubble cavitation is observed in the experiment to incept from the leading edge at these positions which suggests a blade pressure close to, or possibly even below, vapour pressure while the numerically predicted pressure at the leading edge is far lower than the saturation pressure in a considerable region. Without further experimental data clarifying the actual blade pressure, its difficult to assess whether the difference in prediction is related to an error in the flow modelling, or if there are, e.g., geometrical differences between the tested and modelled propeller causing this deviation. However, it is also known that a laminar boundary layer can suppress the cavitation inception even though pressure is far below the saturation pressure.

In Figure 5.15, the cavitation prediction for different mesh resolutions are presented for Case2.1 where the vapour iso-surface is 60%. For SMP-Mesh-III, the picture is modified in a way that each blade position is replaced with the corresponding results of the blade having the refined mesh. Therefore, the picture somehow represents the results for an imaginary full refined propeller.

Comparison between Figure 5.15a and Figure 5.15b shows that the effects of the inlet distance from the propeller are negligible on the cavitation prediction for this investigated operating condition. The only difference can be seen on the leading edge sheet cavity at the radius ratio between 0.4 and 0.5 where SMP-Mesh-II results show lower amount of cavitation.

Comparison between results of Figure 5.15b and Figure 5.15c will reveal the

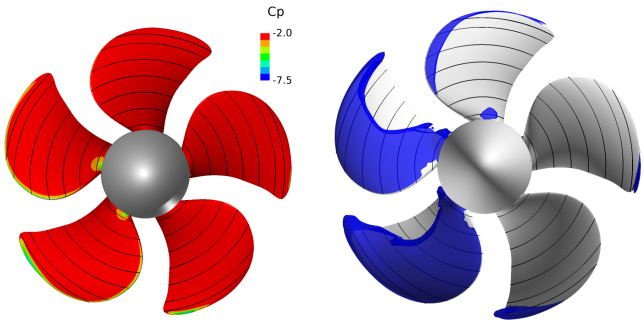

(a) Wetted flow, pressure coefficient (b) Cavitating flow, alpha vapour 0.6

Figure 5.14: Case2.1, view along x-axis, suction side, SMP-Mesh-I

effects of refining mesh resolution on the cavitation prediction. From the results, it can be deduced that the finer mesh is more capable of capturing and preserving the vortex rolled up into the blade tip region; note that only the region around the blade is refined and not when the vortex has left the blade. From the blade position zero degree, it can be seen that finer mesh resolution is able to preserve the tip vortex cavitation longer, till the end of blade tip while in the coarser mesh the tip vortex cavitation is ended before reaching the blade tip. From the blade position 72 degree, it can be seen that in the finer mesh the vortex is rolled up earlier into blade tip region, and also from the blade position 216 degree, it can be seen that the preserved cavity is bigger than the one in the coarser mesh. We remark that the mesh refinement does not affect the over predicted mid radii sheet cavity.

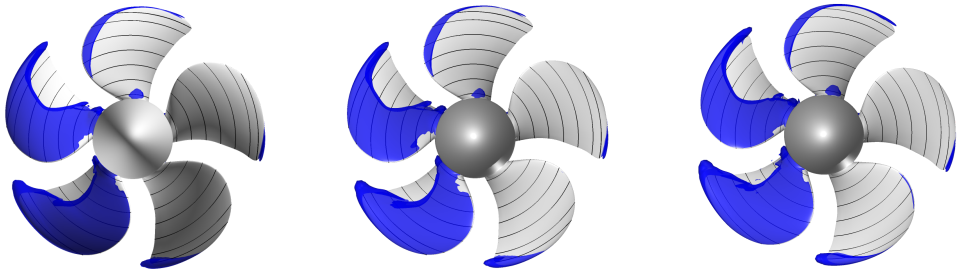

(a) SMP-Mesh-I (b) SMP-Mesh-II (c) SMP-Mesh-III

Figure 5.15: Case2.1, view along x-axis, Suction side, vapour iso-surface 0.6

5.3.3 Summary of PPTC simulations

Comparison between numerical results and experimental observations show that the current methodology is capable of predicting the propeller performance with a high accuracy in some conditions. General agreement between the numerical

Table 5.7: Wetted flow open water performance of RR propellers

Propeller		Mesh	K_T	$10K_Q$
A	Experiment		0.289	0.631
	ILES	Mesh-RR-A-1	0.282	0.636
B	Experiment		0.291	0.644
	ILES	Mesh-RR-B-1	0.272	0.593
	ILES	Mesh-RR-B-2	0.269	0.590

predictions and experiments of the cavitation extent in different operating conditions is acceptable. However, the comparison highlights some limitations of the Eulerian cavitation simulation, and current mass transfer modelling. It is noted that bubble cavitation pattern observed in the experiment is predicted as a sheet cavitation in the numerical simulations, which is a known consequence of the mixture assumption and the mass transfer models used. Moreover, as the current mass transfer modelling does not include effects of laminar boundary layer, the numerical results predict a leading sheet cavity which was not observed in the experiment.

5.4 ROLLS-ROYCE HIGH SKEW PROPELLERS A AND B

In the previous sections, numerical settings and solution algorithm have been verified by comparing the numerical results and experimental data for open access model scale propellers. Here, the simulation has been extended to the industrial propellers in order to provide more detailed information for possible design improvement. Results included here are the wetted flow and cavitating flow simulations of two high skew propellers.

In Table 5.7, thrust and torque coefficients of propellers A and B are presented in wetted flow conditions. These results have been obtained using the same settings which were used to simulate E779A and PPTC propellers. However, while the error level in prediction of the thrust coefficients of propellers E779A, PPTC and A is around 2%, the thrust coefficient prediction error level of propeller B is around 7%.

5.4.1 Cavitation modelling of propeller A

In Table 5.8, the numerical prediction of open water performance of propeller A (thrust and torque coefficients) in the cavitating conditions are presented and compared with the experimental data where the error level of prediction of the forces (i.e. thrust coefficient) is -3.5%.

Comparing the thrust coefficients of the wetted flow conditions, Table 5.7, and the results for cavitating flows reveals that the thrust coefficient has dropped

Table 5.8: Cavitating open water performance of propeller A.

Operating conditions	K_T	$10K_Q$
Experimental data	0.289	0.620
Numerical results	0.279	0.630
Error (%)	-3.5	1.6

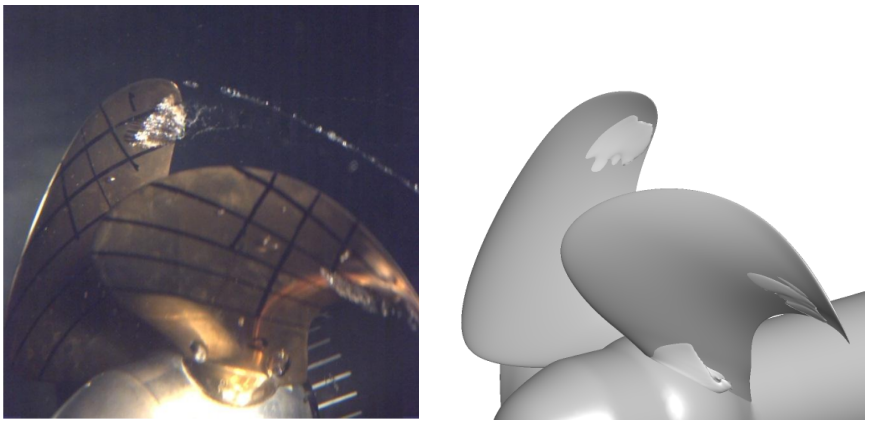

(a) Experiment (b) ILES

Figure 5.16: Side view of numerical predictions vapour Iso-surfaces (50 %) and experimental snapshot, propeller A.

around 1%. Noting that the amount of the thrust coefficient reduction measured in the experiment between the wetted flow and cavitating flow is also around 1% suggests that numerical simulation can predict the flow trend.

In Figure 5.16, the numerical prediction of cavitation (vapour iso-surface 50%) has been compared with the experiment. In the experimental tests, it is observed that the sheet cavity starts from the vortex core and grows toward the blade tip. The current numerical simulation is able to predict the sheet cavity near the tip region. Moreover, in the numerical results, the root cavitation is predicted as sheet cavitation. The vapour iso-surface and pressure coefficient distribution for cavitating flows of propeller A are presented in Figure 5.17.

5.4.2 Cavitation modelling of propeller B

Performance of propeller B in cavitating conditions is presented in Table 5.9. The error level of the thrust coefficient prediction with Mesh-RR-B-1 is 5.1% and with Mesh-RR-B-2 is 6.5%. One possible reason for having better prediction in Mesh-RR-B-1 is having finer mesh resolution near the tip and leading edge of the blades, which helps to capture the high gradient nature of the flow in these regions more accurately.

In Figure 5.18, the pressure coefficient distribution and vapour iso-surfaces (50

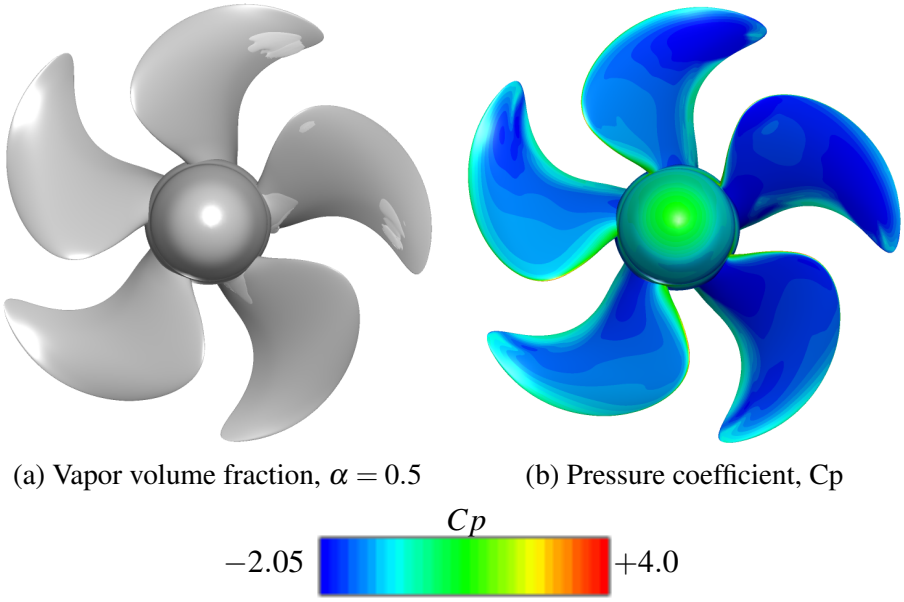

(a) Vapor volume fraction, $\alpha = 0.5$ (b) Pressure coefficient, Cp

Figure 5.17: Front view of numerical predictions vapour Iso-surfaces (50 %) and pressure coefficients of propeller A.

Table 5.9: Cavitating open water performance of propeller B.

Operating conditions	Mesh	K_T	$10K_Q$
Experimental data	—	0.292	0.641
Numerical results	Mesh-RR-B-1	0.277	0.616
	Mesh-RR-B-2	0.273	0.609

%) of cavitating flow simulations for propeller B are presented for two different meshes, and is compared with the experimental observation in Figure 5.19.

The first impression from the comparison is that the total extent of the predicted cavitation is larger than in the experimental observations. The numerical simulations predict cavitation near the leading edge (e.g. blade position 270 degrees) while leading edge sheet cavitation is not found in the experiments. During the experiment, it is observed that the leading edge area may show bubble cavitation, Figure 5.19c. Similar to the cavitation analysis of PPTC propeller, this indicates that the pressure at this region is close to, or even lower than, the saturation pressure.

Comparing the cavitation at the blade position 30 degrees for Mesh-RR-B-1, Figure 5.18a, and Mesh-RR-B-2, Figure 5.18b, shows that results related to Mesh-RR-B-2 better predict the vortex separation from the tip blade region, and the shape of the cavity closure at this region is more similar to the experimental observations. One reason can be the over prediction of cavitation in the blade position 320 degrees of Mesh-RR-B-1 which lead to over prediction of cavitation in the blade position 30 degrees.

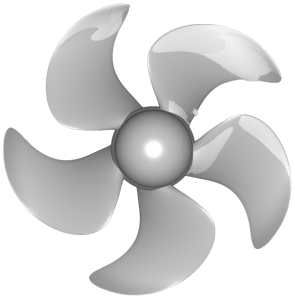

(a) Mesh-RR-B-1, vapour iso-surface

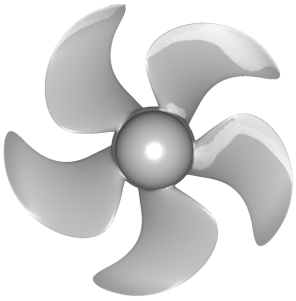

(b) Mesh-RR-B-2, vapour iso-surface

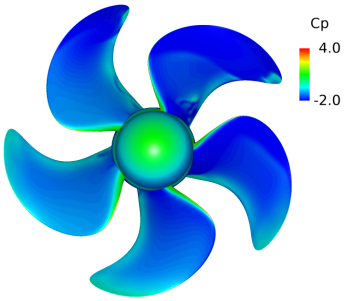

(c) Mesh-RR-B-1, Pressure coefficient

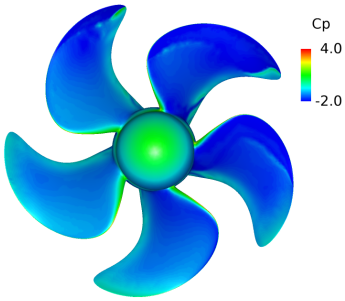

(d) Mesh-RR-B-2, Pressure coefficient

Figure 5.18: Pressure coefficient distribution and vapour iso-surfaces (50 %) of cavitating flow simulations for propeller B.

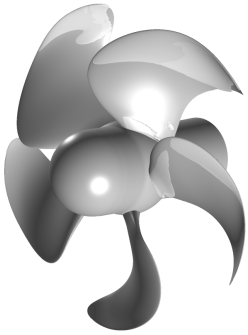

(a) Mesh-RR-B-1

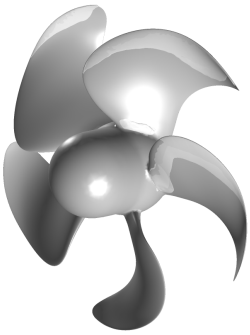

(b) Mesh-RR-B-2

(c) Experiment

Figure 5.19: Comparison between vapour iso-surfaces (50 %) of numerical results and experimental observations for propeller B.

In Figure 5.20, the vapour iso-surfaces of 10% are plotted. From this figure, it can be seen that the results related to Mesh-RR-B-2 are more dependent on the mesh distribution. Moreover, the difference between cavity shape which can be seen in Figure 5.18a and Figure 5.18b at the blade position 270 degrees, is less obvious in the 10% vapour iso-surfaces pictures. It can be seen from this figure that at the blade position 180 degrees, Mesh-RR-B-2 predicts cavitation at the leading edge which is not observed in the experiment.

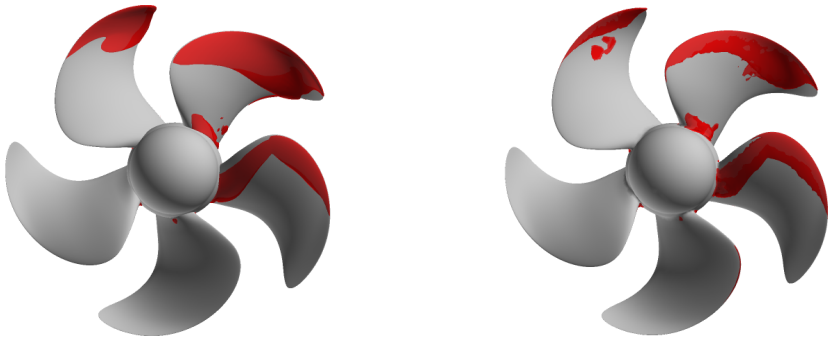

(a) Mesh-RR-B-1 (b) Mesh-RR-B-2

Figure 5.20: Vapor iso-surfaces (10 %) of numerical results for propeller B.

5.4.3 Summary of cavitation modelling of propellers A and B

Similar to the numerical results of the PPTC propeller, numerical simulations on RR-B propeller show sheet cavitation on the leading edge of the propeller while bubble cavitation is observed in the experiment to incept from the leading edge. It might be deduced that this is a modelling discrepancy between the numerical and experimental procedures. Appearance of bubble cavitation in the experiment on the leading edge suggests that pressure at the leading edge is close to, or possibly even below, the saturation pressure while the numerically predicted pressure at the leading edge is far lower than the saturation pressure in a considerable region. Without further experimental data clarifying the actual blade pressure, its difficult to assess whether the difference in prediction is related to an error in the flow modelling, or if there are, e.g., geometrical differences between the tested and modelled propellers causing this deviation. However, it is also known that a laminar boundary layer can suppress the cavitation inception even though pressure is far below the saturation pressure.

6

Cavitation Inception

This chapter includes the experimental and numerical analysis of the tip vortex cavitation inception. The objective is to investigate different inception prediction methods to characterize tip vortex flows around an elliptical foil, as well as on high skewed low-noise propellers. Different propeller operating conditions are studied to explore the capability of the current numerical methods in predicting the tip vortex cavitation inception chart, and therefore the possibility of applying CFD to support advanced propeller design work.

First, the numerical methodology is evaluated on the elliptical foil where different cavitation inception models are applied, and results are discussed. Later, the analysis is extended to the prediction of the cavitation inception charts of the RR propellers C and D. The results of this chapter is included in the paper D and paper F.

6.1 ELLIPTICAL FOIL

The summary of predicted inception points by different methods are presented in Table 6.1. The results are classified into three different categories including the wetted flow simulations, Eulerian cavitation simulations, and Lagrangian simulations. In order to include the spatial mesh resolution effects, each category contains the results of P1S1 and P2S2Wake resolutions.

In the literature, e.g. [70], the tip vortex cavitation inception dependency on the water quality has been investigated in the context of weak water (no tensile strength) and strong water (withstands pressure considerably below the saturation pressure). Weak water resembles the homogenous assumption, where there is no tensile strength. For strong water tested in [70], the estimated initial nuclei size responsible for the tensile strength was around $2\mu m$. From figure 12 of this reference, and for lift coefficient similar to the current study ($C_l = 0.67$), the interpolated values of cavitation inception for weak and strong water are 5.47 and

Table 6.1: Summary of predicted inception points of the elliptical foil

Method	P1S1 Resolution	P2S2Wake Resolution	Category
Minimum pressure	5.34	6.68	Wetted flow simulations
Semi-empirical relation	7.84	7.58	
Energy balance	4.53	5.85	
Minimum vapor volume	4.5	5.5	Eulerian cavitation simulations
Simplified uncoupled RP weak water ($R_0 = 200\mu m$)	5.17	6.59	Lagrangian simulations
Simplified uncoupled RP strong water ($R_0 = 1\mu m$)	2.37	3.61	

2.81, respectively.

Comparing the measured weak water inception value with the predicted value by $-C_p$ criterion and Eulerian simulations, where no tensile strength is assumed in the modelling, clearly show that the results of P2S2Wake are in very good agreement with the experimental measurements. It can be also noted that the $-C_p$ criterion and Eulerian simulations predict very similar values for inception points. One advantage of Lagrangian bubble dynamics simulations is the capability to include the tensile strength by considering small bubble radii, e.g. $1\mu m$. As it is presented in Table 6.1, the results also show very good agreement between the measured value for the strong water inception, 2.81, and the predicted value with the bubble radius of $1\mu m$.

6.2 ROLLS-ROYCE HIGH SKEWED PROPELLERS C AND D

Three different types of cavitation patterns are investigated in details including Back Blade Cavitation (BBC), Back Tip Vortex (BTV), and Face Tip Vortex (FTV). Here, the Back side is the suction side of the blade and Front side is the pressure side of the blade. Due to computational resource limitations, the simulations of the cavitation inception analysis are carried out by employing a steady solver, i.e. simpleFoam, and MRF approach to handle the rotation.

The OW cavitation inception charts of propeller C and D are presented in Figure 6.1. The charts include the experimental measurements and numerical predictions of different cavitation inception criteria. In order to provide a wider range of experimental prediction in lower and higher J values, experimental measurements are interpolated/extrapolated by adopting power trend lines. Minimum pressure, energy balance, minimum vapor volume (Eulerian cavitation simulation), and simplified uncoupled bubble dynamics criteria are employed to predict the cavitation inception points.

For the propellers C and D at OW conditions, and in the range of $0.8 < J < 1.0$, cavitation appears only on the suction side of the blade as BBC, and BTV. Due to the measurement difficulty related to propeller C, the inception measurements

are conducted only in the range of $0.9 < J < 1.0$, while the experimental measurements of propeller D cover the range of $0.8 < J < 1.0$. At higher J values, $1.1 < J$, cavitation appears as pressure side cavitating tip vortex, so called FTV.

Comparing the inception charts of the propellers reveal that both of the them have similar BBC inception characteristics. The tip vortex inception behaviour, however, show significant differences. As the tip vortices are stronger in propeller C, the BTV and FTV cavitation inception happen earlier on this propeller.

6.2.1 Minimum pressure criterion

Considering the measurement uncertainties, the agreement between the experimental data and the minimum pressure criterion is acceptable for BBC and FTV. For BTV, the discrepancy becomes higher. One reason can be the fact that BBC and FTV evolve on the blade or at the edge of the blade where there is enough nuclei to incept cavitation. As in the presence of enough nuclei, cavitation incepts very close to the saturation pressure, the minimum pressure criterion provides good accuracy in BTV and FTV.

6.2.2 Energy balance

In Figure 6.2, variations of predicted and simulated tip vortex vapour volumes versus the cavitation number are presented for J=0.82. Considering the minimum volume detectable during the tip vortex inception measurements, assumed to be $0.2365mm^3$, the predicted BTV cavitation inception points at $J = 0.82$ by the energy criterion are $\sigma_i = 7.53$ for the propeller C, and $\sigma_i = 4.05$ for the propeller D.

The BTV and FTV inception behaviours at other operating conditions are evaluated by this criterion, and are presented in Figure 6.1.

6.2.3 Minimum vapor volume

Eulerian cavitation simulations at different cavitation numbers are needed to be conducted to find the simulated vapour volume corresponding to the cavitation inception condition. As this demands considerable computational resources, the evaluation has been conducted only of one J value, J=0.82, for both of the propellers, and is presented in Figure 6.2. Considering the minimum vapour volume criterion, $0.2365mm^3$, the predicted BTV cavitation inception points at J=0.82 are $\sigma_i = 7.5$ for the propeller C, and $\sigma_i = 4.12$ for the propeller D.

6.2.4 Simplified uncoupled bubble dynamics

The exerted pressure on a particle travelling through the vortex core at different J values is presented in Figure 6.3. The figure clearly shows the considerable

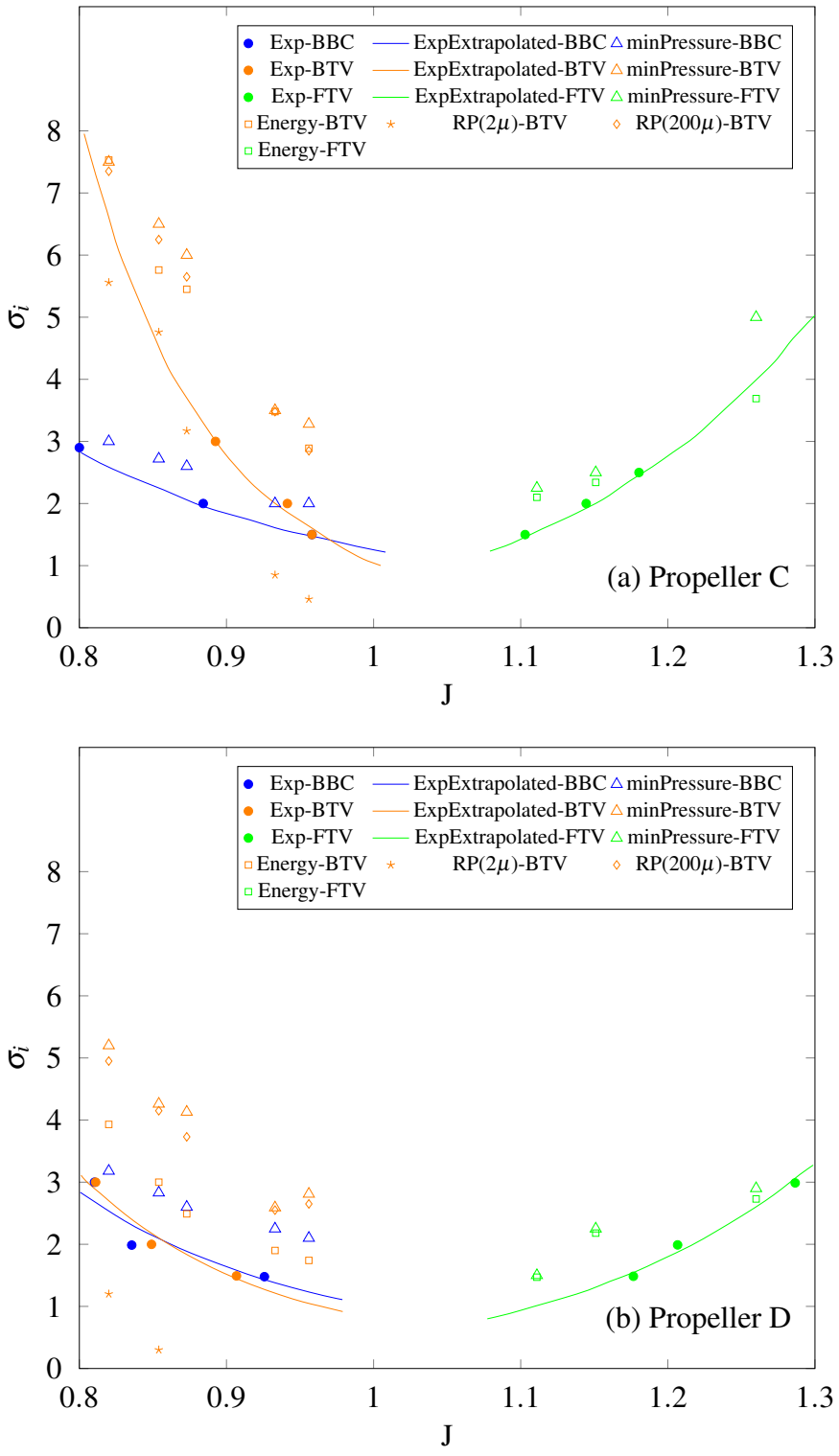

Figure 6.1: Open water cavitation inception diagram of RR propellers

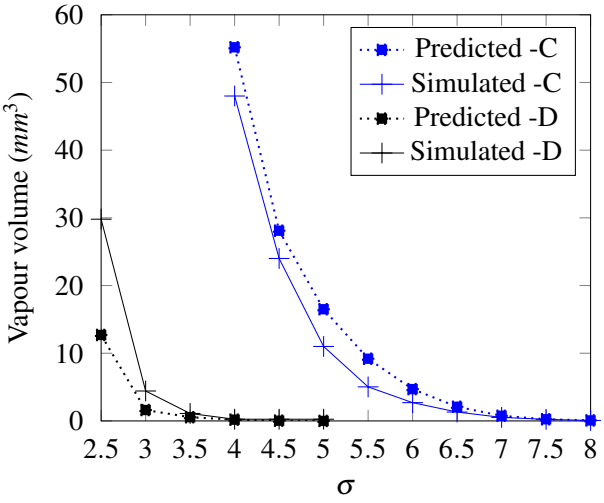

Figure 6.2: Variation of the tip vortex cavitation vapour volume versus the cavitation number, J=0.82, OW condition, propellers C and D

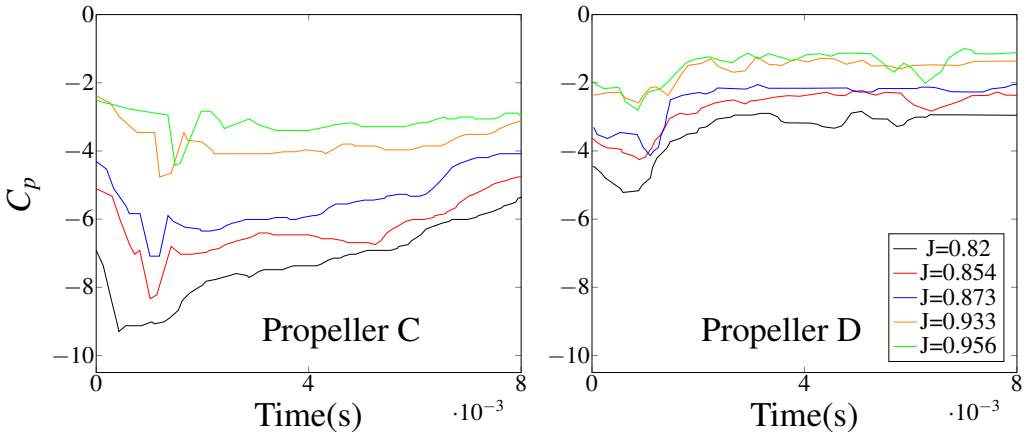

Figure 6.3: Exerted pressure coefficient on a single bubble travelling along the vortex core at different operating conditions, BTV, wetted flow simulations

difference between the tip vortex strengths of the propellers C and D, where the propeller C shows stronger tip vortices.

In Figure 6.4, the predicted cavitation inception numbers for different initial bubble radii along with the values achieved using the minimum pressure criterion are presented. The figure clearly shows the dependency of the predicted cavitation inception number on the initial bubble radius where cavitation incepts almost immediately when the pressure falls below the saturation pressure at higher radii similar to weak water conditions. As a result, the inception prediction of $R = 200\mu m$ is close to the minimum pressure criterion results. The inception analysis of $R = 2\mu m$, which represents strong water conditions, predicts much lower values for the cavitation inception number.

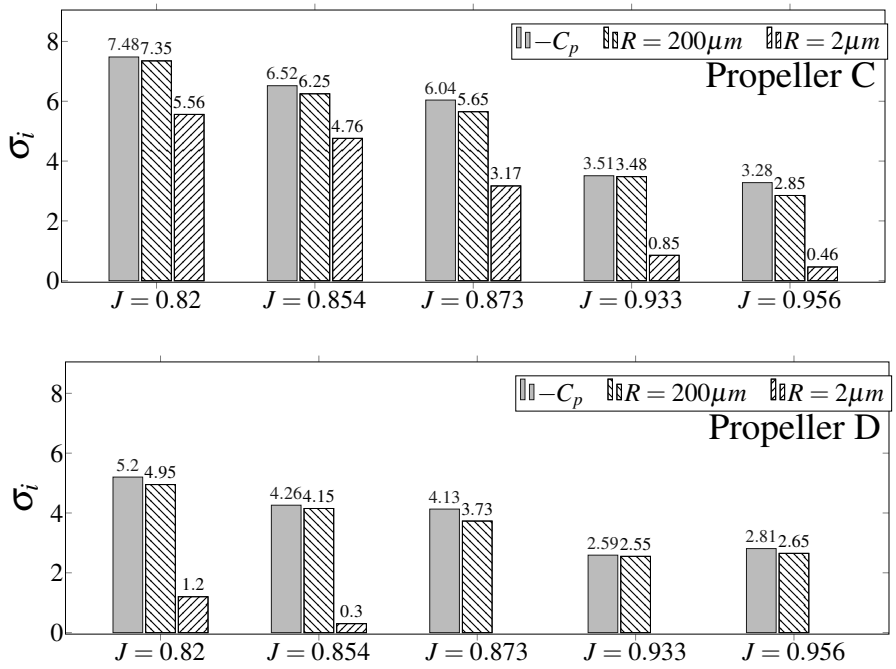

Figure 6.4: Predicted BTV cavitation inception numbers for different initial nuclei radii, compared with minimum pressure criterion ($-C_p$) at different operating conditions

6.2.5 Spatial mesh resolution impacts

When the spatial mesh resolution in the tip region is insufficient, the tip vortex strength cannot be predicted accurately, and consequently higher pressure at the vortex core will be predicted. Since prediction of the tip vortex depends on the spatial mesh resolution, the inception analysis will also depend on the spatial mesh resolution. In Figure 6.5, the inception chart of propeller D is presented where numerical results are provided for two different spatial resolutions, H2 and H3. H3 resolution contains three layers of refinement, and has the spatial resolutions as fine as 0.05 mm in the tip region, and is the resolution employed in Figure 6.1. H2 resolution is coarser and contains two layers of refinements, and has the spatial resolutions as fine as 0.1 mm in the tip region.

As it is presented in Figure 6.5, both of the resolutions predict very similar BBC as the mesh resolution on the blade is the same on both resolutions, and apparently, the flow field at lower radii is not affected by the tip vortex resolutions. However, the tip vortex inception prediction is considerably dependent on the spatial resolution, especially for BTV. As H3 resolution is finer, it predicts stronger tip vortex and therefore higher cavitation inception points than the predicted values by H2 resolution.

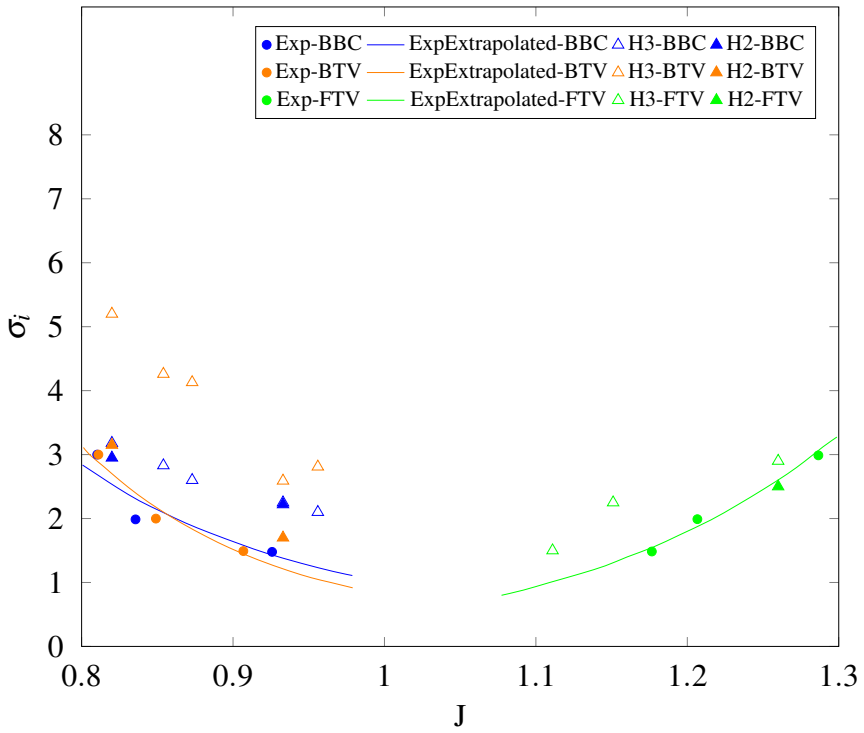

Figure 6.5: Open water cavitation inception diagram of propeller D for different mesh resolutions, minimum pressure inception criterion

6.3 Summary of cavitation inception analysis

The evaluated inception methods include minimum pressure criterion, semi-empirical relation, energy of low pressure region, Eulerian cavitation simulation, and bubble dynamics method.

It is noted that the accuracy of the tip vortex simulation, and consequently the pressure field prediction, affects the cavitation inception predictions. For the elliptical foil, the finer resolution leads to prediction of a stronger tip vortex and therefore earlier cavitation inception.

The analysis of the tip vortex and trailing vortices at the blade tip region indicates the presence of very small flow dynamics, where the interaction of these flow structures determines the pressure field and therefore the cavitation pattern. Comparison of the Q field with experimental high speed recording proves the capability of the current numerical tool in predicting these small scale flow dynamics.

Comparison between the inception charts of the propellers reveal that both of the them have similar BBC inception characteristics. The tip vortex inception behaviour, however, show significant differences. As the tip vortices are stronger on propeller C, the BTV and FTV inception happen earlier on this propeller.

The capability of the current methodology and numerical setup in distinguishing very fine vortical structures between the propellers with slight alternation in

the tip geometry, and TVCI, are indicated. It is shown that the numerical results can predict the trend of the measured cavitation inception patterns very well, and can highlight the contributing vortical structures.

7

Propeller Hydrodynamics

The focus of this chapter is on the formation and development of the tip vortex flow structures around propellers C and D in open water conditions. The vortical structures are evaluated at three different J values, and compared with high speed videos. The objective is to evaluate the capability of the current numerical methods in distinguishing very fine vortical structures and cavitating tip vortex flows between propellers with slight alternation in the tip geometry, and therefore explore the possibility of using CFD to support advanced propeller design work.

7.1 J=0.82, PROPELLER C

The experimental observations clarifies that at this J value, two main vortices are formed in the blade tip region of the propeller C. One is the tip vortex and the other is an inward vortex formed on the blade and then separated at the trailing edge, r/R$\sim$0.9. The interactions of these two vortices with each other, and also the nuclei and turbulent disturbances determine the tip vortex cavitation feature.

In Figure 7.1, three different instances are presented for interactions of these two vortices in the cavitating condition of σ=2. It can be observed that the inward vortex and tip vortex have different inclinations, and trajectories, where the propeller skewness and the blade rake angle contributes on. In Figure 7.1a, the inward vortex cavitates on the blade, and extends to the trailing edge as a cavitating trailing vortex, while the tip vortex cavitates downstream of the blade tip. As the cavitating inward vortex become thicker, the tip vortex cavitation extends further upstream, Figure 7.1b. Finally, when the inward vortex cavity disappears, the tip vortex cavitation starts from the tip of the blade, Figure 7.1c. The high fidelity numerical simulations can precisely detect these two vortices, and their interactions, Figure 7.2. It clearly declares that the interactions of the vortices change their strengths and noticeably their trajectories.

The tip vortex roll-up (and therefore the tip vortex strength) is strongly de-

(a) (b) (c)

Figure 7.1: Interactions of vortices at the tip of the blade, and formation of tip vortex cavitation, propeller C, OW, J=0.82, σ=2.

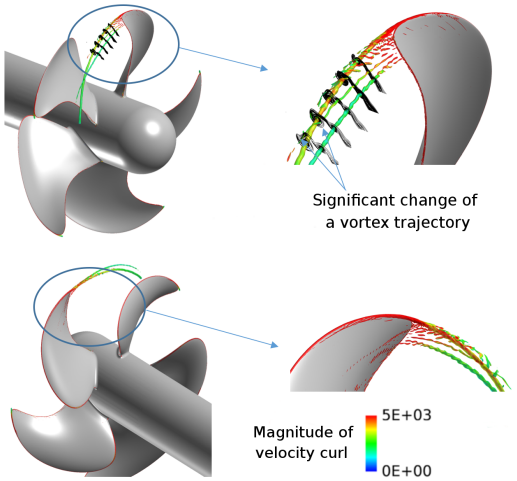

Figure 7.2: Numerical prediction of vortex interactions at the tip of the propeller C, Iso surface of Q (Q=1000) coloured with magnitude of velocity curl along with the velocity streamlines, different views, OW, J=0.82, wetted flow.

pendent on the trailing vortices, Figure 7.2. The results indicate the presence of very small scale flow dynamics in the tip region of the blade, also noted in the experimental observations. However, these vortical structures are formed mostly on the tip or at the trailing edge of the blade. There are only a few vortical structure formations on the blade close to the trailing edge.

Comparison between the experimental observations and the wetted flow numerical results is presented in Figure 7.3. The numerical results include an iso-surface of pressure equal to the saturation pressure, and an iso-surface of Q criterion equal to 200. It should be noted that all of the iso-surfaces of the Q criterion presented in this study is coloured by the magnitudes of the velocity curl similar to Figure 7.3. Comparison indicates that the location of the blade bubble cavitation and tip vortex have been accurately predicted by the numerical simulations. The numerical simulations are carried out in wetted flow conditions, and thus, the predicted cavitating region does not include the probability of nuclei effects. The

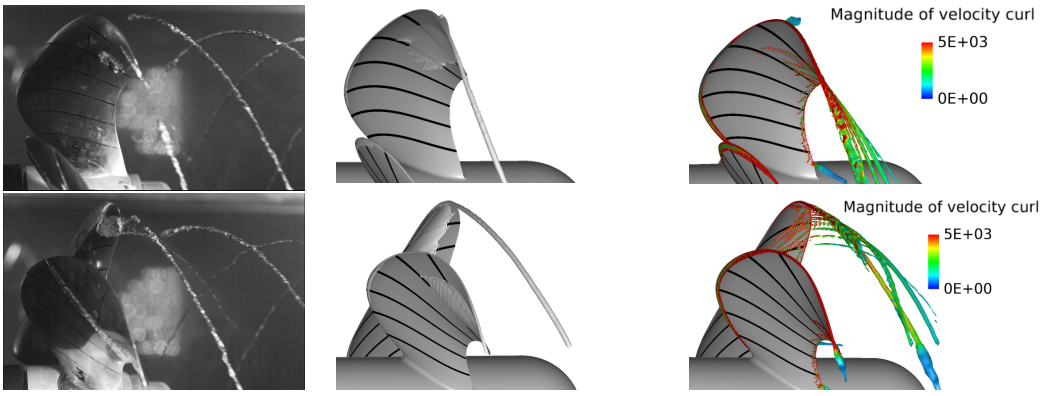

(a) Experiments (b) $p = p_{sat}$ (c) Q=200

Figure 7.3: Comparisons between experimental instances and numerical predictions in the wetted flow conditions, propeller C, OW, J=0.82, σ=2.

distribution of Q clearly shows that the separated vortices at the trailing edge of the blade contribute to the strength of the main tip vortex. The predicted blade bubble cavitation covers a lager area than the experimental snapshot. As it is observed in the experimental snapshots, the pressure in the region $0.8 \leq r/R \leq 0.9$ is either lower than the saturation pressure or very close to the saturation pressure which has been accurately predicted by the numerical simulations.

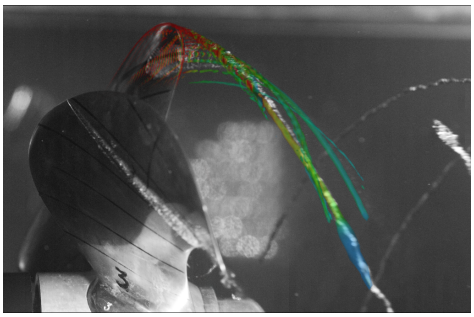

Figure 7.4: Plotting the numerical Q prediction on the related experimental snapshot, propeller C, OW, J=0.82, σ=2.

In Figure 7.4, the numerical prediction of vortical structures, Q criterion, and the experimental observation at one instance of Figure 7.3 are plotted together. The figure proves that the trajectory of the tip vortex is predicted very accurately for the propeller C at J=0.82 and $\sigma = 2$. Results also provides more insights regarding the interaction of trailing vortices and its effects on the cavitation formation.

In Figure 7.5, the cavitation simulations at different cavitation numbers are presented, and compared with experimental snapshots. It can be noted that although the flow vortical structures are predicted very well in the wetted flow simulations, the discrepancy between experimental observations and cavitation sim-

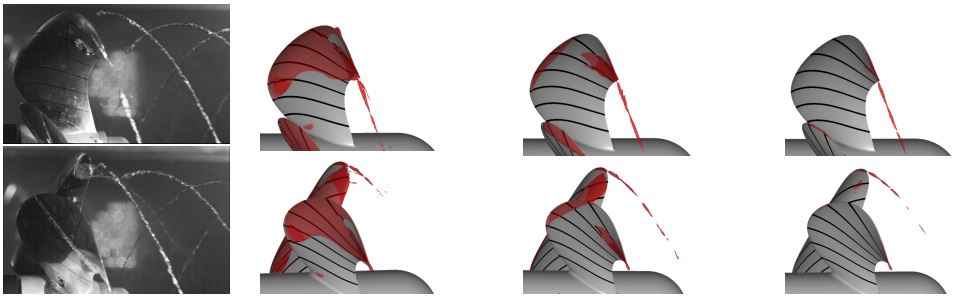

(a) Exp. $\sigma = 2$ (b) $\sigma = 2$ (c) $\sigma = 2.5$ (d) $\sigma = 3$

Figure 7.5: Comparisons between experimental instances and numerical results at different σ, J=0.82, $\alpha_v = 0.5$, propeller C

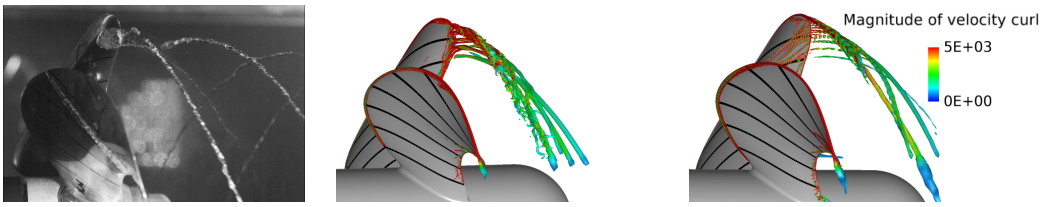

(a) Exp. σ=2 (b) σ=2 (c) Wetted flow

Figure 7.6: Effects of the presence of blade cavitation on the vortical structures, Q=200, J=0.82, propeller C

ulations are considerable, Fig. 7.5a and Fig. 7.5b. Similar discrepancy between numerical predictions and experimental observations are noted in other cases, e.g. PPTC propeller in the Symposium of Marine Propulsors (SMP) 2015, where it is highlighted that limitations of the Eulerian cavitation simulation, and current mass transfer modelling in considering laminar boundary layer or nuclei distributions are the main reasons for this discrepancy.
At higher cavitation numbers, e.g. $\sigma = 3$, where the sheet cavity is weaker or does not exist in the numerical predictions, the structure of cavitating tip vortex matches better with the experimental observations, Fig.7.5d.

Comparison of vortical structures between cavitating flow simulations, Fig.7.6b, and wetted flow simulations, Fig.7.6c, shows that the presence of the cavitation alters the structures of the trailing vortices although does not change the main tip vortex structures.

7.2 J=0.82, PROPELLER D

The experimental observations of the propeller D at σ=2 and $J = 0.82$ are presented in Figure 7.7. At these conditions, the sheet cavitation are formed on the suction side of the blade covering the upper part of the blade from the leading edge till the trailing edge in $r/R > 0.7$, Figure 7.7a. However, as it can be seen in Figure 7.7b, in the lower radii at r/R$\sim$0.5, intermittent appearance of cavitation

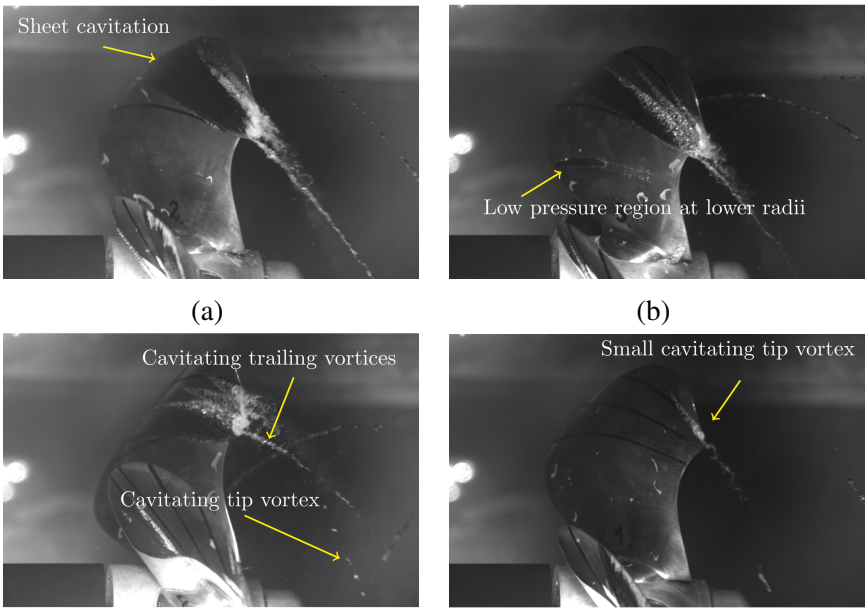

Figure 7.7: Experimental observations of sheet and tip vortex cavitation interactions, propeller D, OW, J=0.82, σ=2.

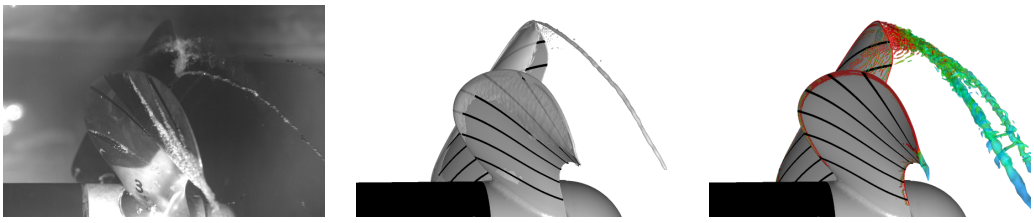

(a) Experimental instances (b) $p = p_{sat}$ (c) Q=200

Figure 7.8: Comparisons between experimental instances and numerical predictions in the wetted flow conditions, propeller D, OW, J=0.82, σ=2.

is noted at the leading edge which extends till the mid-chord of the blade. It indicates that the pressure at the leading edge at these radii is either lower than the saturation pressure or very close to that, and consequently small disturbances lead to cavitation at these radii.

Formation of sheet cavitation on the blade, and its extension to the trailing edge leads to formation of cavitating trailing vortices. It also alters the tip vortex structure, and prevents formation of a cavitating tip vortex. From Figure 7.7c, it can be observed that at r/R$\sim$0.7 the sheet cavitation leads to formation of a strong cavitating trailing vortex. The cavitating tip vortex is prevented on the blade tip, and postponed to the downstream to form a few uncontentious elongated bubble cavitation.

In Figure 7.8, experimental observations are compared with the wetted flow numerical results at $J = 0.82$. The iso-surface of pressure equal to the saturation

pressure shows that in $r/R > 0.5$ the leading edge pressure is lower than the saturation pressure. In $r/R > 0.7$, the iso-surface of pressure extends till the blade trailing edge, and covers most of the blade area, Figure 7.8b. The pressure at the tip vortex is lower than the saturation pressure. It can be noted that the pressure at the trailing vortices in $r/R > 0.9$ is also lower than the saturation pressure. The discrepancy between experimental observations of cavitating tip vortex and numerical prediction of the pressure iso-surface in propeller D is considerable. The presence of the blade sheet cavitation in the propeller D considerably alters the pressure field at the tip region, and therefore increases the discrepancy between wetted flow results and cavitation measurements. In the conditions that the sheet cavity on the blade does not affect the cavitating tip vortex structure, e.g. J=0.785 at $\sigma = 3$ in Figure 7.9, the cavitating tip vortex forms right at the tip of the blade which therefore can be predicted with a high accuracy by the wetted flow simulations, Figure 7.10.

Around the propeller C, vortical structures are formed mostly on the tip of the blade while in propeller D, the vortical structures are formed on the blade, and then shed at the trailing edge of the blade. Consequently the shedding vortical structures are more significant for propeller D, especially in $r/R > 0.8$.

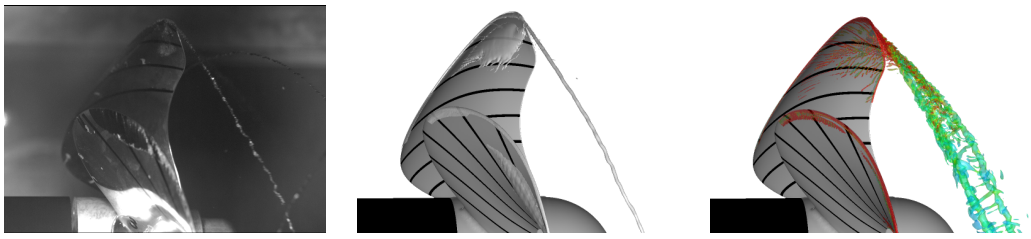

(a) Experimental instances (b) $p = p_{sat}$ (c) Q=200

Figure 7.9: Comparisons between experimental instances and numerical predictions in the wetted flow conditions, propeller D, OW, J=0.785, σ=3.

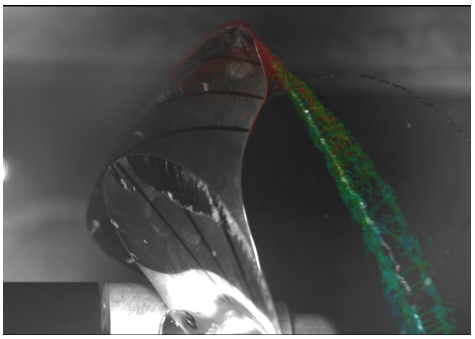

Figure 7.10: Plotting the numerical Q prediction on the related experimental snapshot, propeller D, OW, J=0.785, σ=3.

At J=0.82 and $\sigma = 2$, the propeller D experiences sheet cavitation on the upper part of the blade, in the r/R>0.7 region. It is also noted that at lower radii,

(a) Exp. $\sigma = 2$ (b) $\sigma = 2$ (c) $\sigma = 2.5$ (d) $\sigma = 3$

Figure 7.11: Comparisons between experimental instances and numerical results at different σ, J=0.82, $\alpha_v = 0.5$, propeller D

r/R>0.5, the leading edge pressure is lower than the saturation pressure which appears as an intermittent cavitation during the experimental tests. Eulerian cavitation simulation predicts these low pressure regions as cavitating regions, Figure 7.11. In this figure, the comparison between an experimental snapshot and related cavitation simulations is presented. In order to provide further insights about the sensitivity of the propeller to operating conditions, numerical results of different cavitation numbers are included.

As the grid resolution is not fine enough at the aft part of the blade in the r/R>0.8 region, very small structures of cavitating trailing vortices are predicted as a sheet cavity. At r/R$\sim$0.8, a strong cavitating trailing vortex is observed in the experimental snapshot which has not been predicted in the numerical results due to the insufficient grid resolution.

Although at J=0.82 the cavitation incepts later in propeller D compared to propeller C, cavitation simulations at different cavitation numbers show that the propeller D is more sensitive to the operating conditions. While at $\sigma = 3$ cavitation appears only as a small sheet cavity on the leading edge of the propeller D, Figure 7.11d, at $\sigma = 2$ sheet cavity covers almost the whole blade, Figure 7.11b.

Presence of the cavitating structures at the aft part of the blade leads to formation of smaller vortical structures. For propeller D, these vortical structures are formed in the r/R>0.8 region, Figure 7.12b. Comparison between the vortical structures in the wetted flow simulations, Figure 7.12c, and the vortical structures in the cavitating conditions, Figure 7.12b, suggests that in both of the cases the main tip vortex forms at the tip of the blade, and develops till downstream. However, it should be noted that presence of cavitation alters the structure of the tip vortex as in the wetted flow condition, the pressure inside the main tip vortex is lower than the saturation pressure, and in the cavitating case, the pressure at the core of the tip vortex is predicted to be higher than the saturation pressure.

7.3 J=1.26

In Figure 7.13 and 7.14, experimental observations are compared with wetted flow numerical results at J=1.26. The agreement between pressure iso-surface $p = p_{sat}$ and the observed cavitating tip vortex is acceptable as the extent and location of the cavitating tip vortex have been predicted very well.

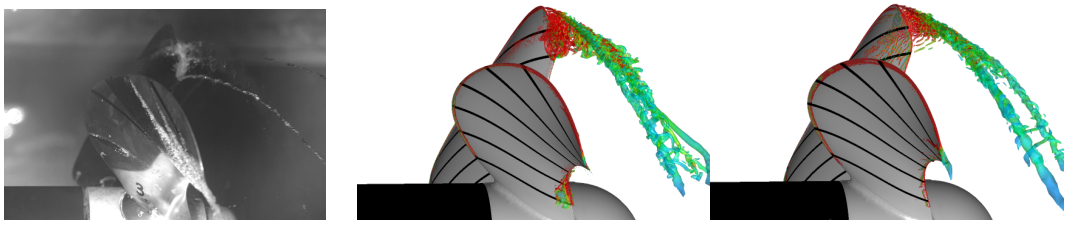

(a) Exp. σ=2 (b) σ=2 (c) Wetted flow

Figure 7.12: Effects of the presence of blade cavitation on the vortical structures, Q=200, J=0.82, propeller D

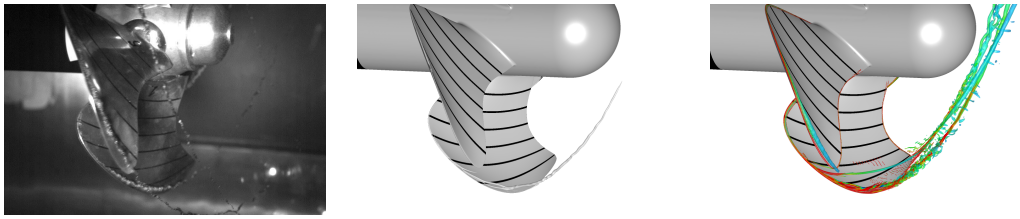

(a) Experimental instances (b) $p = p_{sat}$ (c) Q=200

Figure 7.13: Comparisons between experimental instances and numerical predictions in the wetted flow conditions, propeller C, OW, J=1.26, $\sigma = 2$

In Figure7.15, white coloured pressure iso-surface is plotted along with the distribution of Q= 200 coloured with the magnitude of the velocity curl on the pressure side of the blade. As it can be seen, the pressure iso-surface is located inside the attached tip vortex which is rolled up and shaped on the leading edge, and then developed as the main tip vortex. The figure also reveals the presence of very small vortical structures on the blade of propeller D in r/R>0.8. The roll-up of these shedding vortices leads to formation of a strong trailing vortex located downstream of the blade at r/R$\sim$0.9. On propeller C, formation of a vortical structure originating on the leading edge at r/R$\sim$0.85 is also noted.

7.4 J=0.933

At this J value and for σ=2, the propeller only experiences suction side cavitation. Both of the propellers experience on blade bubble cavitation in $0.8 < r/R < 0.9$ close to the tailing edge, while only for propeller C, a cavitating tip vortex is predicted, Figure 7.16. The results of the propeller D, Figure 7.16b, shows that there is no strong tip vortex attached to the blade. Vortical structures are generated on the blade, and then are shed from the trailing edge of the bade in $0.8 < r/R$. The roll-up of these trailing vortices lead to formation of a tip vortex and a strong trailing vortex downstream of the blade trailing edge.

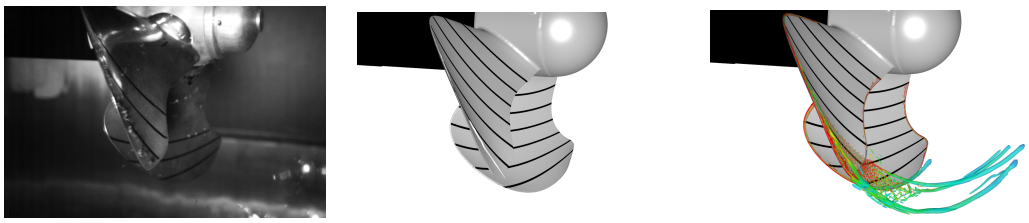

(a) Experimental instances (b) $p = p_{sat}$ (c) Q=200

Figure 7.14: Comparisons between experimental instances and numerical predictions in the wetted flow conditions, propeller D, OW, J=1.26, $\sigma = 2$

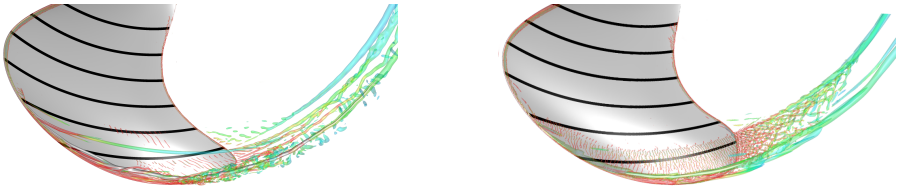

(a) Propeller C (b) Propeller D

Figure 7.15: Presentation of Q=200 and white coloured pressure iso surface, $p = p_{sat}$, in the wetted flow conditions, pressure side view, J=1.26

7.5 Summary of numerical simulations of propellers C and D

Three different cavitation patterns are observed on the propellers. At low J values, $0.8 < J < 1.0$, cavitation appears on the suction side of the blade as sheet/bubble (BBC), and cavitating tip vortex (BTV), while at higher J values, only pressure side cavitating tip vortex appears on the propeller (FTV).

For propeller A at J=0.82 in OW conditions, vortical structures are formed mostly on the tip of the blade while for propeller B, vortical structures also formed on the blade, and then shed at the trailing edge of the blade. Consequently, the shedding vortical structures are more significant for propeller B, especially in r/R$>$0.8.

For both propellers at J=1.26 in OW conditions, the saturation pressure iso-surface is located inside the main tip vortex which is rolled-up and shaped on the leading edge. For propeller B, shedding of very small vortical structures in r/R$>$0.8 leads to formation of a strong trailing vortex located downstream of the blade at r/R$\sim$0.9.

At J=0.933, propeller B does not show an attached strong tip vortex, and there is only shedding of trailing vortices in 0.8$<$r/R which in the downstream of the blade roll-up to form a stronger trailing vortex.

It is shown that the current methodology is capable of predicting very fine cavitating vortical structures between propellers with only slight differences in the tip geometry, and can be employed to support advanced propeller design work.

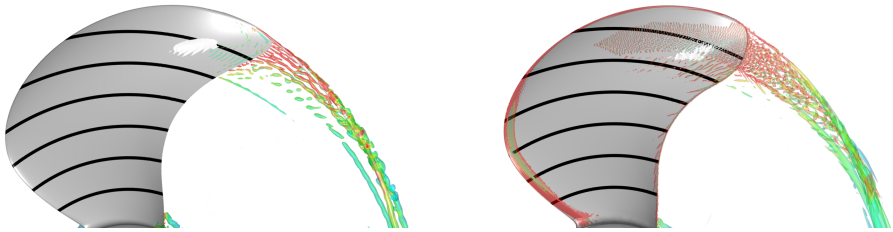

(a) Propeller C (b) Propeller D

Figure 7.16: Presentation of Q=200 and white coloured pressure iso-surface, $p = p_{sat}$, in the wetted flow conditions, suction side view, J=0.933

8

Concluding Remarks

This thesis concerns cavitation formation and numerical simulation of this phenomenon, in the early stage, i.e. cavitation inception, and in the developed form, i.e. sheet or cloud cavitation, primarily for marine propellers. As cavitating tip vortices are usually the first form of cavitation that appears on propeller blades, development of a numerical methodology for the tip vortex cavitation inception is in focus. For developed cavitation simulation, the spatial mesh resolution requirements and mass transfer modelling in the Eulerian cavitation simulation framework is evaluated.

Different cavitation patterns and regimes are studied, and it is shown that the simultaneous adoption of incompressible Implicit LES and Transport Equation Model can provide accurate predictions of sheet/cloud cavitation. The capability of the current methodology and numerical setup in distinguishing very fine vortical structures between the propellers with slight alternation in the tip geometry, and tip vortex cavitation inception are highlighted. It is shown that the numerical results can predict the trend of the measured cavitation inception patterns very well, and can highlight the contributing vortical structures. The results clarify the possible improvement of the SST $k-\omega$ model in predicting the tip vortex flows by employing curvature correction models. It is shown that some of these models are capable to predict accurate tip vortex flow fields, partly due to that they alter the boundary layer behaviour on the foil, and formation of a leading edge vortex. This is consistent with the flow behaviour predicted by Implicit LES, and is believed to be crucial for the correct behaviour with an accelerated axial flow in the vortex core. As tip vortex flows involve very small scales of flow structures in time and space, numerical simulations of them require very fine grid resolutions, and high-order schemes making the simulations very costly. In addition, we note the following detailed remarks.

Sheet and cloud cavity

The dependency of the sheet cavity closure region and the cloud cavity collapse on the spatial mesh resolution is investigated in the numerical results of the Twisted foil. As a consequence of the collapse dependency on the mesh resolution, the collapse induced pressure pulses also become dependent on the resolution. The collapse occurs in a very small fraction of time, and therefore the pressure oscillation induced by the collapse has limited effects on the force prediction but the erosion and noise prediction will be affected. One suggestion is using very fine resolution in the closure regions which results in an increased computational cost. Another suggestion is using automatic mesh refinement approach to refine the computational cells in the regions where collapse occurs.

To calibrate the mass transfer rate, the velocity strain time scale is suggested and tested. It was shown that using this time scale will improve the accuracy of the pressure distribution as well as cavitation pattern predictions. Moreover, it is highlighted in the E779A propeller simulation that different calibrated mass transfer models lead to similar cavitation prediction.

The shear stress effects on the rupturing of the liquid pocket is modelled by considering the velocity strain rate as an appropriate for the magnitude of the shear stress tensor. It is shown that this modification will increase vapor generation, but also affect condensation behaviour.

Tip vortex flows

Numerical simulation around the tested Rolls-Royce propellers show that the flow around the blade is mostly dominated by the vortex structure near the tip region as well as the tip vortex cavitation.

The mesh dependency study clarifies that at least 32 grid points across the vortex core diameter are required to accurately predict the tip vortex with the current numerics. The streamwise grid point demand is found to be lower, with cell sizes equal to 16 grid points across the vortex core diameter, as the streamwise gradients of the flow are lower compared to the inplane flow gradients. Since the OpenFOAM package can be reasonably considered as a second order numerical tool, these findings match with the previous reports on LES analysis of tip vortex flows. As the tip vortex formation and its roll-up are mostly governed by the boundary layer in the vicinity of the foil tip, which is covered by the mesh refinement regions, further refinements of the spatial mesh on the wake of the foil is found not to have significant contributions on the tip vortex prediction.

Mesh resolution requirements for cavitating tip vortex are clarified to be lower than wetted tip vortex simulations. It is found that presence of cavitation would increase the tip vortex diameter consequently leading to lower grid requirements.

Comparisons of the velocity distributions between numerical results and experimental PIV images show a very good agreement. It highlights the capability of the current approach in predicting the accelerated axial velocity at the vortex core, and therefore good prediction of the pressure distribution which is very important in cavitation inception studies.

Impact of turbulence modelling on tip vortex flow predictions

The comparison between Euler, ILES, and SST $k-\omega$ results shows the importance of turbulence modelling in accurate prediction of tip vortex velocity and pressure fields. While the SST $k-\omega$ model is totally incapable of predicting the tip vortex, ILES and Euler can predict the pressure field of the tip vortex. However, as the accelerated axial velocity at the vortex core depends on the development of boundary layers on the foil and the vortex roll-up, Euler simulation fails to predict the vortex core accelerated axial velocity.

The comparison of ILES and LDKM results clarifies that both of these LES models can provide very accurate tip vortex flow predictions.

As curvature correction (CC) models are dependent on the values and distribution of flow parameters, their performance, and particularly the distribution of correction function, is flow field dependent. As finer structures are resolved in finer resolutions, the distribution of the correction function is also mesh resolution dependent.

Tip vortex cavitation inception

The simplest numerical approach to determine the cavitation inception number, σ_i, is the minimum pressure criteria. In this method, the operating condition when the lowest pressure value of a wetted flow falls below the saturation pressure is called the inception point. The advantage of the method is its simplicity, as it only requires the pressure field of the wetted flow simulation to determine the inception point. However, the method does not include the nuclei contribution on the inception prediction, and therefore usually leads to over prediction of σ_i.

The cavitation inception study by the bubble dynamic approach shows a strong dependency of the inception on the nuclei size. It is found that as the nuclei radius is increased, the inception point tends towards the minimum pressure criterion which corresponds to the weak water measurements. The prediction of the inception for small nuclei sizes (i.e. $2\mu m$) shows good agreement with the strong water measurements of inception. For accurate tip vortex cavitation inception prediction, it is necessary to determine the size of nuclei which can be captured into the vortex core region.

Energy balance and minimum vapour volume criteria generally predict similar cavitation inception while minimum vapour volume criterion is computationally more costly as it demands Eulerian cavitation simulation at different operating conditions.

The accuracy of the tip vortex simulation, and consequently the pressure field prediction, affect the cavitation inception predictions. For the elliptical foil, the finer resolution leads to prediction of a stronger tip vortex and therefore an earlier cavitation inception.

The analysis of the tip vortex and trailing vortices at the blade tip region indicates the presence of very small flow dynamics, where the interaction of these flow structures determines the pressure field and therefore the cavitation pattern. Comparison of the Q field with experimental high speed recording proves the ca-

pability of the current numerical tool in correctly predicting these small scale flow dynamics.

Cavitating propeller simulation

The numerical simulations on the PPTC propeller and RR propellers show sheet cavitation on the leading edge of the propeller while bubble cavitation is observed in the experiment to incept from the leading edge.

This might be a modelling discrepancy between the numerical and experimental procedures. Appearance of bubble cavitation in the experiment on the leading edge suggests that pressure at the leading edge is close to, or possibly even below, the saturation pressure while the numerically predicted pressure at the leading edge is far lower than the saturation pressure in a considerable region. Without further experimental data clarifying the actual blade pressure, its difficult to assess whether the difference in prediction is related to an error in the flow modelling, or there are, e.g., geometrical differences between the tested and modelled propeller causing this deviation. However, it is also known that a laminar boundary layer can suppress cavitation inception, even though pressure is far below the saturation pressure. Therefore, it is suggested to measure the pressure over the blade, e.g. by using Pressure-Sensitive Paint.

REFERENCES

[1] J.P. Franc and J.M. Michel. *Fundamentals of cavitation*, volume 76. Springer, 2006.

[2] N.X. Lu. *Modeling cavitation mechanisms using large eddy simulation*. PhD thesis, Departmnet of Shipping and Marine Technology, Chalmers University of Technology, 2013.

[3] J.S. Carlton. Cavitation. In J.S. Carlton, editor, *Marine Propellers and Propulsion (Second Edition)*, pages 205 – 246. Butterworth-Heinemann, Oxford, second edition edition, 2007.

[4] Y.A. Bouziad. *Physical modelling of leading edge cavitation: Computational methodologies and application to hydraulic machinery*. PhD thesis, Citeseer, 2006.

[5] Propeller erosion. http://www.brighthubengineering.com. Accessed: 2015-4-14.

[6] J.P. Franc and J.M. Michel. Attached cavitation and the boundary layer:experimental investiguation and numerical treatment. *Journal of Fluid Mechanics*, 154:6390, 1985.

[7] L. Tassin and S. L Ceccio. Examination of the flow ear the leading edge of attached cavitation. part 1; detachment of two-dimensional and axisymmetric cavities. *Journal of Fluid Mechanics*, 376:61–90, 1998.

[8] A. Vallier. *Eulerian and Lagrangian cavitation related simulations using OpenFOAM*. Licentiate thesis, Lund University, Lund, Sweden, 2010.

[9] A. Vallier. *Simulations of cavitation from the large vapour structures to the small bubble dynamics*. PhD thesis, Lund University, Lund, Sweden, 2013.

[10] P. Queutey and M. Visonneau. An interface capturing method for free-surface hydrodynamic flows. *Computers and Fluids*, 36(9):1481 – 1510, 2007.

[11] J. Sauer. *Instationär kavitierende Strömungen : ein neues Modell, basierend auf Front Capturing (VoF) und Blasendynamik*. PhD thesis, PhD thesis, Karlsruhe University, 2000.

[12] J. Sauer and G.H. Schnerr. Unsteady cavitating flow - a new cavitation model based on a modified front capturing method and bubble dynamics. In *In Fluids Engineering Summer Conference, Proceedings of FEDSM*, 2000.

[13] A.K. Singhal, M.M. Athavale, H. Li, and Y. Jiang. Mathematical basis and validation of the full cavitation model. *Journal of Fluids Engineering*, 124(3):617–624, 2002.

[14] P.J. Zwart, A.G. Gerber, and T. Belamri. A two-phase model for predicting cavitation dynamics. In *ICMF 2004 International Conference on Multiphase Flow, Yokohama, Japan*, 2004.

[15] R.F. Kunz, D.A. Boger, D.R. Stinebring, T.S. Chyczewski, J.W. Lindau, H.J. Gibeling, S. Venkateswaran, and T.R. Govindan. A preconditioned Navier–Stokes method for two-phase flows with application to cavitation prediction. *Computers & Fluids*, 29(8):849–875, 2000.

[16] C.L. Merkle, J. Feng, and P.E.O. Buelow. Computational modeling of the dynamics of sheet cavitation. In *3rd International Symposium on Cavitation, Grenoble, France*, 1998.

[17] I. Senocak. *Computational Methodology for the Simulation of Turbulent Cavitating Flows*. PhD thesis, University of Florida, Florida, 2002.

[18] I. Senocak and W. Shyy. Interfacial dynamics-based modelling of turbulent cavitating flows, part-1: Model development and steady-state computations. *International Journal for Numerical Methods in Fluids*, 44:975–995, 2004.

[19] I. Senocak and W. Shyy. Interfacial dynamics-based modelling of turbulent cavitating flows, part-1: Time-dependent computations. *International Journal for Numerical Methods in Fluids*, 44:997–1016, 2004.

[20] S. Gopalan and J. Katz. Flow structure and modeling issues in the closure region of attached cavitation. *Physics of Fluids*, 12(4):895–911, 2000.

[21] R.E.A. Arndt, V.H. Arakeri, and H. Higuchi. Some observations of tip-vortex cavitation. *Journal of Fluids Mechanics*, 229, 1991.

[22] B.H. Maines and R.E.A. Arndt. Tip vortex formation and cavitation. *Journal of Fluids Engineering, Transactions of the ASME*, 119(2):413–419, 1997.

[23] W. G. Souders and G. P. Platzer. *Tip vortex cavitation characteristics and delay of inception on a three-dimensional hydrofoil*. Naval Ship Research and Development Center,, 1981.

[24] O. Boulon, M. Callenaere, J.P. Franc, and J.M. Michel. An experimental insight into the effect of confinement on tip vortex cavitation of an elliptical hydrofoil. *Journal of Fluid Mechanics*, 390:1–23, 1999.

[25] C. E. Brennen. *Cavitation and Bubble Dynamics*. Oxford University Press , New York, 1995.

[26] P. Ligneul and R. Latorre. Study of nuclei distribution and vortex diffusion influence on nuclei capture by a tip vortex and nuclei capture noise. *Journal of Fluids Engineering, Transactions of the ASME*, 115(3):504–507, 1993.

[27] C.T. Hsiao and G.L. Chahine. Scaling of tip vortex cavitation inception noise with a bubble dynamics model accounting for nuclei size distribution. *Journal of Fluids Engineering, Transactions of the ASME*, 127(1):55–65, 2005.

[28] K. Park, H. Seol, W. Choi, and S. Lee. Numerical prediction of tip vortex cavitation behavior and noise considering nuclei size and distribution. *Applied Acoustics*, 70(5):674–680, 2009.

[29] Y.T. Shen and P.E. Dimotakis. Viscous and nuclei effects on hydrodynamic loadings and cavitation of a NACA 66 (mod) foil section. *Journal of Fluids Engineering, Transactions of the ASME*, 111(3):306–316, 1989.

[30] J.J.A. Schot, P.C. Pennings, M.J.B.M. Pourquie, and T.J.C. van Terwisga. Modelling of tip vortex cavitation for engineering applications in OpenFOAM. In *11th World Congress on Computational Mechanics*, July 20-25, 2014, Barcelona, Spain.

[31] A. Asnaghi, , R.E. Bensow, and U. Svennberg. Implicit large eddy simulation of tip vortex on an elliptical foil. In *Proceedings of Fifth International Symposium on Marine Propulsion, Espoo, Finland*, 2017.

[32] A. Asnaghi, , R.E. Bensow, and U. Svennberg. Comparative analysis of tip vortex flow using RANS and LES. In *Proceedings of VII International Conference on Computational Methods in Marine Engineering, Nantes, French*, 2017.

[33] K.H. Kim, G. Chahine, J.P. Franc, and A. Karimi. *Advanced Experimental and Numerical Techniques for Cavitation Erosion Prediction*. Springer Netherlands, 2014.

[34] T. Huuva. *Large eddy simulation of cavitating and non-cavitating flow*. Chalmers University of Technology, 2008.

[35] G. Kuiper. *Cavitation inception on ship ship propeller models*. PhD-thesis, Delft Technical University, 1981.

[36] R.E. Bensow and G. Bark. Implicit LES predictions of the cavitating flow on a propeller. *Journal of Fluids Engineering*, 132(4):041302, 2010.

[37] F. Vesting, R. Gustafsson, and R.E. Bensow. Development and application of optimisation algorithms for propeller design. *Ship Technology Research*, 63(1):50–69, 2016.

[38] B. Zhang, J. Lou, C.W. Kang, A. Wilson, J. Lundberg, U. Svennberg, and R.E. Bensow. CFD modeling of propeller tip vortex over large distances. *International Journal of Offshore and Polar Engineering*, 24(3):181–183, 2014.

[39] C. Fureby. ILES and LES of complex engineering turbulent flows. In *European Conference on Computational Fluid Dynamics, ECCOMAS CFD*, 2006.

[40] W. J. Rider. Effective subgrid modeling from the ILES simulation of compressible turbulence. In *European Congress on Computational Methods in Applied Sciences and Engineering ECCOMAS, Computational Fluid Dynamics Conference*, 2006.

[41] A. Asnaghi. *Developing Computational Methods for Detailed Assessment of Cavitation on Marine Propellers*. Licentiate thesis, Department of Shipping and Marine Technologies, Chalmers University of Technology, 2015.

[42] R.E. Bensow and M. Liefvendahl. Implicit and explicit subgrid modeling in LES applied to a marine propeller. In *38th Fluid Dynamics Conference and Exhibit, American Institute of Aeronautics and Astronautics*, 2008.

[43] F.S. Pereira, L. Eça, and G. Vaz. On the order of grid convergence of the hybrid convection scheme for rans codes. In *Congreso de Métodos Numéricos en Ingeniería, Bilbao, Spain*, 2013.

[44] S. Menon and W.W. Kim. High Reynolds number flow simulations using the localized dynamic subgrid-scale model. *34th AIAA Aerospace Sciences Meeting and Exhibit, Reno, Nevada*, 1996.

[45] F. Menter. Zonal two equation $k-\omega$ turbulence models for aerodynamic flows. *AIAA Paper*, 93, 1993.

[46] F. R. Menter, M. Kuntz, and R. Langtry. Ten years of industrial experience with the SST turbulence model. *Turbulence, Heat and Mass Transfer*, 4:625 – 632, 2003.

[47] A. Hellsten. Some improvements in menter $k-\omega$ SST turbulence model. In *29th AIAA Fluid Dynamics Conference, Albuquerque, NM*, June 15 18, 1997.

[48] A. Revell, G. Iaccarino, and X. Wu. Advanced rans modelling of wingtip vortex flows. In *Center for Turbulence Research, Proceedings of the Summer Program*, 2006.

[49] S.K. Arolla and P.A. Durbin. Modelling rotation and curvature effects within scalar eddy viscosity model framework. *International Journal of Heat and Fluid Flow.*, 39:7889, 2013.

[50] S.K. Arolla and P.A. Durbin. Assessing the effects of streamline curvature on the aerodynamics of circulation control airfoil. *AIAA Paper*, 2013.

[51] M. Visonneau, E. Guilmineau, P. Queutey, J. Wackers, and GB. Deng. Assessment of statistic and hybrid les turbulence closures for complex free-surface flow simulation with combined grid refinement criteria. In *30th symposium on naval hydrodynamics, Hobarth, Tasmania, Australia*, 2014.

[52] S.K. Arolla. *Modeling and eddy simulation of rotating and curved turbulent flows*. PhD thesis, Doctoral Thesis, Iowa State University, Ames, Iowa, 2013.

[53] B.A. Pettersson, P.A. Durbin, and A. Ooi. Modeling rotational effects in eddy-viscosity closures. *International Journal of Heat and Fluid Flow*, 20(6):563 – 573, 1999.

[54] Starccm-user guide, version 10.06. https://www.cd-adapco.com/. Accessed: 2017-3-10.

[55] S.K. Arolla and P.A. Durbin. A rotation/curvature correction for turbulence models for applied cfd. *Progress in Computational Fluid Dynamics An International Journal*, 14:341 – 351, 2014.

[56] P. Smirnov and F. Menter. Sensitization of the SST turbulence model to rotation and curvature by applying the Spalart-Shur correction term. *Journal of Turbomachinery*, 131(4), 2009.

[57] A.S. Stabnikov and A.V. Garbaruk. Testing of modified curvature-rotation correction for $k-\omega$ SST model. *Journal of Physics: Conference Series*, 769(1), 2016.

[58] M. Kato and B. E. Launder. The modelling of turbulent flow around stationary and vibrating square cylinders. In *Proceedings of 9th Symposium on Turbulent Shear Flows, Kyoto, Japan*, 1993.

[59] R.E.A. Arndt. *Fluid Vortices*. Springer Netherlands, 1995.

[60] F. M. White. *Fluid Mechanics*. Tata McGraw - Hill Education, 2011.

[61] A. Asnaghi, A. Feymark, and R.E. Bensow. Improvement of cavitation mass transfer modeling based on local flow properties. *International Journal of Multiphase Flow*, 93:142 – 157, 2017.

[62] N. Wikstrom, G. Bark, and C. Fureby. Large eddy simulation of cavitation submerged objects. In *Eighth international conference on numerical ship hydrodynamics, Busan, Korea*, 2003.

[63] H. Jasak H.G. Weller, G. Tabor and C. Fureby. A tensorial approach to CFD using object oriented techniques. *Computational Physics*, 12, 1997.

[64] H. Jasak. *Error Analysis and Estimation for the Finite Volume Method with Applications to Fluid Flows*. PhD thesis, Department of Mechanical Engineering, Imperial College of Science, Technology and Medicine, 1996.

[65] H. Rusche. *Computational Fluid Dynamics of Dispersed Two-Phase Flows at High Phase Fractions*. PhD thesis, Department of Mechanical Engineering, University of London, Technology and Medicine, 2002.

[66] A. Asnaghi. *InterPhaseChangeFoam Tutorial [Online]*. Chalmers University of Technology, 2013. Available http://www.tfd.chalmers.se/ hani/kurser/OS_CFD_2013/.

[67] A.H. Koop. *Numerical simulation of unsteady three-dimensional sheet cavitation*. University of Twente, 2008.

[68] E.J. Foeth. *The structure of three-dimensional sheet cavitation*. PhD thesis, Delft Technical University, 2008.

[69] E.J. Foeth and T. Terwisga. The structure of unsteady cavitation, part i: Observation of an attached cavity on a three-dimensional hydrofoil. In *Proceedings of 6th International Symposium on Cavitation, Wageningen, The Netherlands*, 2006.

[70] R.E.A. Arndt and A.P. Keller. Water quality effects on cavitation inception in a trailing vortex. *Journal of Fluids Engineering*, 114, 1992.

[71] P.C. Pennings, J. Westerweel, and T.J.C. Van Terwisga. Flow field measurement around vortex cavitation. *Experiments in Fluids*, 56, 2015.

[72] H. Streckwall and F. Salvatore. Results of the wageningen 2007 workshop on propeller open water calculations including cavitation. In *RINA Marine CFD, Southhampton, England*, 2008.

[73] G. Dubbioso, R. Muscari, and A.D. Mascio. CFD analysis of propeller performance in oblique flow. In *Third International Symposium on Marine Propulsors, smp13, Launceston, Tasmania, Australia*, 2013.

[74] A. Stella, G. Guj, and Felice F.D. Propeller wake flowfield analysis by means of LDV phase sampling techniques. *Experiments in Fluids*, 28, 2000.

[75] D.D. Florio, F.D. Felice, G.P. Romano, and M. Elefante. Propeller wake structure at different advance coefficients by means of piv. In *Proceedings of PSFVIP-3, Maui, HI*, 2001.

[76] F.D. Felice, M. Felli, G. Giordano, and M. Soave. Pressure and velocity correlation in the wake of a propeller. In *Proceedings of Propeller Shafting, Virginia Beach, Norfolk, VA*, 2001.

[77] 2nd international workshop on cavitating propeller perfomance. http://www.caee.utexas.edu/smp15/smp_workshop_2015.html. Accessed: 2015-04-11.

[78] Potsdam Propeller Test Case SVAtech GmbH Potsdam. http://www.sva-potsdam.de/pptc_data.html. Accessed: 2015-4-14.

[79] N.X. Lu, R. E. Bensow, and G. Bark. Large eddy simulation of cavitation development on highly skewed propellers. *Journal of Marine Science and Technology*, 19, 2013.

[80] P.C. Pennings, J. Bosschers, J. Westerweel, and T.J.C. Van Terwisga. Dynamics of isolated vortex cavitation. *Journal of Fluid Mechanics*, 778:288–313, 2015.

[81] P. C. Pennings. *Dynamics of Vortex Cavitation*. PhD -thesis, Delft Technical University, 2016.

[82] D.B. Stinebring, K.J. Farrell, and M.L. Billet. The structure of a three- dimensional tip vortex at high Reynolds numbers. *Journal of Fluids Engineering, Transactions of the ASME*, 113(3):496–503, 1991.

[83] J. Wells. *Effects of Turbulence Modeling on RANS Simulations of Tip Vortices*. Master thesis, Virginia Polytechnic Institute and State University.

[84] X.X. Peng, B. Ji, Y. Cao, L. Xu, G. Zhang, X. Luo, and X. Long. Combined experimental observation and numerical simulation of the cloud cavitation with u-type flow structures on hydrofoils. *International Journal of Multiphase Flow*, 79:10–22, 2016.

[85] N.X. Lu, R.E. Bensow, and G. Bark. LES of unsteady cavitation on the Delft twisted foil. *Journal of Hydrodynamics, Ser. B*, 22(5):784–791, 2010.

[86] B. Ji, X. Luo, Y. Wu, X. Peng, and Y. Duan. Numerical analysis of unsteady cavitating turbulent flow and shedding horse-shoe vortex structure around a twisted hydrofoil. *International Journal of Multiphase Flow*, 51:33–43, 2013.

[87] R.E. Bensow. Simulation of the unsteady cavitation on the Delft Twist11 foil using RANS, DES and LES. In *Proceedings of the 2nd International Symposium on Marine Propulsors. Hamburg, Germany*, 2011.

[88] G.H. Schnerr, I.H. Sezal, and S.J. Schmidt. Numerical investigation of three-dimensional cloud cavitation with special emphasis on collapse induced shock dynamics. *Physics of Fluids*, 20(4):040703, 2008.

[89] S. Park and S. H. Rhee. Numerical analysis of the three-dimensional cloud cavitating flow around a twisted hydrofoil. *Fluid Dynamics Research*, 45(1), 2013.

[90] G. Vaz, T. Lloyd, and A. Gnanasundaram. Improved modelling of sheet cavitation dynamics on delft twist11 hydrofoil. In *Proceedings of VII International Conference on Computational Methods in Marine Engineering, Nantes, French*, 2017.

[91] L. Eça and M. Hoekstra. Evaluation of numerical error estimation based on grid refinement studies with the method of the manufactured solutions. *Computers and Fluids*, 38:1580 – 1591, 2009.

[92] L. Eca, G. Vaz, and M. Hoekstra. A verification and validation exercise for the flow over a backward facing step. In *Proceedings of V European Conference on Computational Fluid Dynamics, ECCOMAS CFD 2010,Lisbon, Portugal, 14-17 June 2010*, 2010.

[93] G.F Rosetti, G. Vaz, and A.C. Fujarra. URANS calculations for smooth circular cylinder flow in a wide range of reynolds numbers: Solution verification and validation. *Journal of Fluids Engineering, Transactions of the ASME*, 134, 2012.

[94] M. Morgut. *Prediction of non-cavitating and cavitating flow on hydrofoils and marine propellers by CFD and advanced model calibration*. PhD thesis, Universit Degli Studi Di Udine, 2012.

[95] E. Guilmineau, GB. Deng, A. Leroyer, P. Queutey, M. Visonneau, and J. Wackers. Numerical simulations for the wake prediction of a marine propeller in straight-ahead flow and oblique flow. *Journal of Fluids Engineering, Transactions of the ASME*, 140, 2017.